Innovative Approaches to Superdeformed Nuclear Shapes Studies in Heavy Actinides

Nazarena Tortorelli

SIGIL·UNIVERSITAT·LUDOVIC·MAXIM

Muenchen 2024

Innovative Approaches to Superdeformed Nuclear Shapes Studies in Heavy Actinides

Nazarena Tortorelli

Dissertation
an der Fakultät für Physik
der Ludwig–Maximilians–Universität
München

vorgelegt von
Nazarena Tortorelli
aus Neapel, Italien

München, den 17.12.2024

Erstgutachter: Peter G. Thirolf
Zweitgutachter: Andreas Wilhelm Oberstedt
Tag der mündlichen Prüfung: 19.03.2025

Contents

List of Figures

List of Tables

Zusammenfassung

Der Aktiniden-Bereich bietet eine außergewöhnliche Möglichkeit zur Erforschung superdeformierter Kernformen, die durch ihre extreme Deformation sowie einzigartige Schaleneffekte und deformierungsfördernde Kräfte charakterisiert sind. Diese Kernzustände bieten Einblicke in grundlegende Aspekte der Kernstruktur. Obwohl dieses Forschungsfeld seit über einem Jahrhundert untersucht wird, ermöglichen neueste technologische Fortschritte Untersuchungen mit bisher unerreichter Präzision und Reichweite.

Diese Dissertation konzentriert sich auf zwei vorbereitende Experimente, die darauf abzielen, Methoden zur Produktion und Detektion exotischer Isotope und Spaltisomere im Aktiniden-Bereich weiterzuentwickeln. Das erste Experiment wurde am Fragment Separator (FRS) und an der FRS Ion Catcher (FRS-IC) am GSI durchgeführt. Durch Projektilfragmentation eines ^{238}U-Primärstrahls mit 1000 MeV/u wurden Aktinidenkerne erzeugt, mit hoher Präzision separiert und identifiziert. Die Isotope wurden anschließend in einer kryogenen Stoppzelle gestoppt, extrahiert und mithilfe fortschrittlicher Massenspektrometrietechniken analysiert. Um die Detektion kurzlebiger Spaltisomere zu ermöglichen, wurden technologische Verbesserungen an der Stoppzelle vorgenommen, wodurch die Ionenaustrittszeit auf unter 30 ms reduziert und die Akzeptanz für höhere Strahlraten erhöht wurde. Die Inbetriebnahme dieser Verbesserungen sowie die experimentellen Ergebnisse zeigten die Machbarkeit der Untersuchung von Kernen in diesem anspruchsvollen Bereich der Nuklidkarte. Zusätzlich wurde eine neuartige Time-Over-Threshold (ToT)-Methode implementiert, die sich als effektiv erwies, um Spaltfragmente von Alphazerfällen zu unterscheiden, trotz der geringen Querschnitte der Spaltprozesse im Vergleich zu konkurrierenden Zerfallskanälen.

Das zweite Experiment wurde am IGISOL-System im JYFL-Labor der Universität Jyväskylä in Finland durchgeführt und konzentrierte sich auf die Untersuchung von ^{240f}Am und ^{242f}Am. Das Spaltisomer ^{242f}Am, mit einer Halbwertszeit von etwa 14 ms, ist das langlebigste Spaltisomer und ein entscheidendes Element bei der Untersuchung der Eigenschaften von doppel-höckrigen Spaltbarrieren wie sie für Spaltisomere charakteristisch sind. Frühere Untersuchungen mit der Reaktion $^{242}\mathrm{Pu}\,(\mathrm{d}, 2\mathrm{n})^{242}\mathrm{Am}$ identifizierten optimale Produktionsenergien im Bereich von 7–12 MeV, während theoretische Vorhersagen einen Wert von 13.8 MeV nahelegten. Dieses Experiment validierte die Methodik zur Produktion von ^{242f}Am und ^{240f}Am, bestimmte deren Halbwertszeiten und das Verhältnis zwischen Isomer und Grundzustand und untersuchte die Anregungsenergie von ^{242}Am. Darüber hinaus wurde das Potenzial von ^{242}Am als Kandidat für die Nuclear Excitation by Electron Cap-

ture (NEEC)-Methode untersucht, was neue Einblicke in diesen Mechanismus bietet.

Die Ergebnisse beider Experimente legen die Grundlage für zukünftige Studien im Aktiniden-Bereich und unterstreichen den Wert der Integration komplementärer Methoden wie der am FRS-IC und IGISOL eingesetzten. Die Ergebnisse betonen die Bedeutung präziser Massenmessungen und fortschrittlicher Detektionstechniken bei der Verfeinerung von Spaltbarrierenparametern.

Zusammenfassend hebt diese Dissertation die Bedeutung fortschrittlicher experimenteller Aufbauten zur Untersuchung superdeformierter Kerne und Spaltisomere hervor. Durch die Nutzung der komplementären Stärken des FRS, Ion Catchers und IGISOL trägt diese Arbeit nicht nur zum Verständnis der Kernstruktur bei, sondern ebnet auch den Weg für zukünftige Untersuchungen exotischer Isotope. Diese Ergebnisse leisten einen bedeutenden Beitrag zur Kernstrukturphysik im Bereich schwerer, stark deformierte Kerne und eröffnen neue Wege, die komplexe Landschaft von Deformationsphänomenen im Bereich niedriger Drehimpulse zu erforschen.

Abstract

The actinides region presents an exceptional opportunity for exploring superdeformed nuclear shapes, characterized by their extreme deformation and associated with unique shell effects and deformation-driving forces. These nuclear states provide a window into fundamental aspects of nuclear structure. While this field has been studied by now for over a century, recent technological advancements now allow for investigations with unprecedented precision and scope.

This thesis focuses on two exploratory experiments aimed at advancing methodologies for the production and detection of exotic isotopes and fission isomers in the actinides region. The first experiment was conducted at the Fragment Separator (FRS) and FRS Ion Catcher (FRS-IC) at GSI. Using projectile fragmentation of a ^{238}U primary beam at 1000 MeV/u, actinide nuclei were produced, separated, and identified with high precision. The isotopes were subsequently stopped in a cryogenic stopping cell, extracted, and analyzed using advanced mass spectrometry techniques. To enable the detection of short-lived fission isomers, technological upgrades to the stopping cell were developed, reducing ion extraction times to below 30 ms and increasing rate capabilities for higher beam current acceptance. The commissioning of these improvements, as well as the experimental results, demonstrated the feasibility of studying nuclei in this challenging region of the nuclear chart. Additionally, a novel Time-Over-Threshold (ToT) method was implemented, proving effective in differentiating fission fragment events from alpha decays, despite the low cross-section of fission processes relative to competing decay channels.

The second experiment was conducted at IGISOL, located at the JYFL Laboratory of the University of Jyväskylä in Finland, focusing on the study of ^{240f}Am and ^{242f}Am.

The fission isomer ^{242f}Am, with a half-life of approximately 14 ms, represents the longest-lived known fission isomer and represents a critical subject for studying the properties of double-humped fission barriers, which are characteristic for fission isomers. Previous investigations using the $^{242}\mathrm{Pu(d, 2n)}^{242}$Am reaction identified peak production energies in the range of 7–12 MeV, with theoretical predictions suggesting a value of 13.8 MeV. This experiment validated the methodology for producing ^{242f}Am and ^{240f}Am, measured their half-lives and isomer-to-ground state ratios, and explored the excitation energy of ^{242}Am. Furthermore, the study investigated the potential of ^{242}Am as a candidate for Nuclear Excitation by Electron Capture (NEEC), offering new insights into this mechanism.

The findings from both experiments lay the groundwork for future studies in the actinides region, highlighting the value of integrating complementary methodologies such as those employed at FRS-IC and IGISOL. The results emphasize the importance of precise mass measurements and advanced detection techniques in refining fission barrier parameters.

In conclusion, this thesis underscores the importance of integrating advanced experimental setups for the study of superdeformed nuclei and fission isomers. By leveraging the complementary strengths of the FRS, Ion Catcher, and IGISOL, this work not only enhances our understanding of nuclear structure but also sets the stage for future investigations of exotic isotopes. These results contribute significantly to the broader field of nuclear physics in the region of heavy, strongly deformed nuclei, offering new pathways to explore the intricate landscape of deformation-dependent phenomena in the regime of low angular momenta.

Chapter 1

Introduction and motivation

1.1 The history of isomer studies

When this doctoral project started few years ago, the physics community celebrated the centenary of the discovery of nuclear isomers with the aims to continuing to explore this field thanks to new technologies available. Before doing so, as with any compelling story, it is necessary to recount its most significant milestones. Therefore, in this chapter, some sections will be devoted to a historical introduction to nuclear isomers, eventually leading to a more detailed description of fission isomers, which are the main focus of this thesis. In honor of the 100th anniversary of the discovery of nuclear isomers, several scientific articles were written on the subject, in particular, a book entirely dedicated to the topic titled "Nuclear Isomers" [1], the new Handbook of Nuclear Physics [2], with an entire section dedicated to nuclear fission and a chapter on nuclear isomers, and the recently published special edition of the European Physics Journal on "Nuclear Isomers" [3]. They are mentioned here because much of what will be found in the following chapters refers to these works, but also for a second reason—to express the gratitude to the authors of these articles and books, who have provided well-organized and readily accessible scientific information and references, thereby facilitating the writing process.

It is appropriate to begin by retracing the century since the discovery of nuclear isomers. With Ernest Rutherford's identification of the compact atomic nucleus in 1911 [4], the nuclear age commenced. Almost concurrently, in 1913, the British chemist Frederick Soddy identified chemical "isotopes" [5], defined as variants of chemical elements with the same number of protons but differing in the number of neutrons, although the neutron itself had not yet been discovered. Building on this finding, Soddy later proposed in 1917 the possibility of the existence of "isotopes with identical atomic weight and chemical properties, but differing in their stability and mode of disintegration" [5].

This statement intertwines the discovery of chemistry with the emerging field of nuclear physics when, in 1921, at the Kaiser Wilhelm Institute for Chemistry in Berlin, German chemist Otto Hahn, together with his colleague Lise Meitner, discovered nuclear isomers. [A good and interesting biography of Lise Meitner can be found here: [6]]. They were methodically mapping out the complex process by which ^{238}U nuclei decay radioactively to form stable ^{206}Pb nuclei. The decay chain involves a number of different nuclei, including a completely new chemical element with atomic number 91. Having discovered a particular isotope of this element, Hahn and Meitner named it proto-actinium. Specifically, what they discovered was (what is now known as) ^{234}Pa had two $\beta-$decaying states, one with a half-life of 1 minute and the other of 7 hours.

Figure 1.1: Historical picture of the chemist Otto Hahn and physicist Lise Meitner at the Kaiser-Wilhelm Institute in Berlin in 1913. (Courtesy: Archives of the Max Planck Society, Berlin).

The work of Hahn and Meitner marked the discovery of nuclear isomerism and the birth of the new field of nuclear structure. However, progress in our understanding of isomers was slow, and it was only with the discovery of the neutron by James Chadwick in 1932 [7] that the concept began to gain attraction. Finally, in 1936, the German physicist Carl Friedrich von Weizsäcker proposed the accepted explanation for isomers [8]. Von Weizsäcker realized that all nuclei have angular momentum, or spin, and that different arrangements of proton and neutron orbits can create different spin states, just as "chemical isomers" have different spatial arrangements of atoms. If the excited state has a spin very different from the ground state, it will take a long time to emit a gamma ray and decay to the ground state. In the case of protactinium$-$234, for example, the difference between the two states is four units of spin or $4\hbar$. This makes (E4) gamma decay so slow that the excited state is actually more likely to decay by emitting an electron (β decay). These isomers are known as spin isomers. Spin isomers have been of fundamental importance in nuclear physics, especially for the development of the "nuclear shell model", which was developed in 1949 by Maria Göppert Mayer [9] and independently by Otto Haxel, Hans Daniel Jensen, and Hans Suess [10]. Just as electrons form atomic shells that can hold no more than a certain number of electrons, neutrons and protons form nuclear shells, with similar limits on how many protons and neutrons each nuclear shell can contain. The first shell can hold up to two nucleons, the second up to eight, with subsequent shells accommodating a maximum of 20, 28, 50, and 82 nucleons. Known as "magic numbers", these values are the same for both proton and neutron shells. Due to the neutron excess in heavy elements, higher magic number for neutrons are 126 and 184, while the magic number for protons beyond 82 is still in the focus of research in the field of super-heavy elements.

As the years passed, more and more data on isomers were collected, which helped in the understanding and development of various nuclear models. A well-known historical example of isomers is the 8^- state in ^{180}Hf with a half-life of 5.5 hours. In 1953, Bohr and Mottelson identified a group of levels in ^{180}Hf as the first rotational band ever observed in a nucleus [11]. This fundamental rotational band, populated by the long-lived 8^- isomeric state in ^{180}Hf, opened a new field of rotational phenomena in nuclei, leading to the development of collective nuclear models and the discovery of a new type of isomers, the K isomers, found in deformed nuclei.

We have now reached the 1960s, when another piece in the description of isomers is added. During this period, isomers were discovered in excited nuclei significantly changing shape when decaying to the ground state [12]. These isomers are known as shape isomers, and during decay, they can undergo a transition, for example, from spherical to prolate. In very heavy nuclei, there is even a subset of shape isomers, known as "fission isomers" (which we will focus on in this thesis), where the excited nucleus spontaneously splits into two lighter nuclei during decay.

To schematically represent an isomer, we can describe it as a second minimum in the potential energy landscape, where the nucleus remains trapped before decaying to the ground or to another excited state. The energy scale of isomeric excitation energies ranges from keV to MeV, while the decay time ranges from nanoseconds to several years. The known isomers are compiled in the "Atlas of Nuclear Isomers" [13], which presentely contains about $2,581$ isomers along with their various spectroscopic properties such as energies, spin and parity, decay branches, multipolarity, gamma energies, etc. This data reveals many new systematic features across the nuclear landscape, with characteristics varying from region to region.

Fig. 1.2 displays a selection of long-lived ($> 1ms$), highly excited ($> 1MeV$) isomers, (discoveries since 2010 are represented by open circles, the data are from [14]) which are mainly found in exotic neutron-rich and proton-rich nuclei, as well as in the transuranic region of superheavy nuclei. It is noticeable that the overall distribution of isomers in the N-Z plane is not random. This indicates that the distribution of isotopes on the chart of nuclides (as well as the type of nuclides and decay modes) is closely connected to nuclear structure. This is extremely interesting and suggests that a more detailed study of nuclear isomers could help answer questions about nuclear structure and models.

1.1.1 Modes of Isomer Decay

Isomers can decay through the emission of α or β particles, or via fission, depending on their energetics, but they can also de-excite via electromagnetic processes (emission of γ

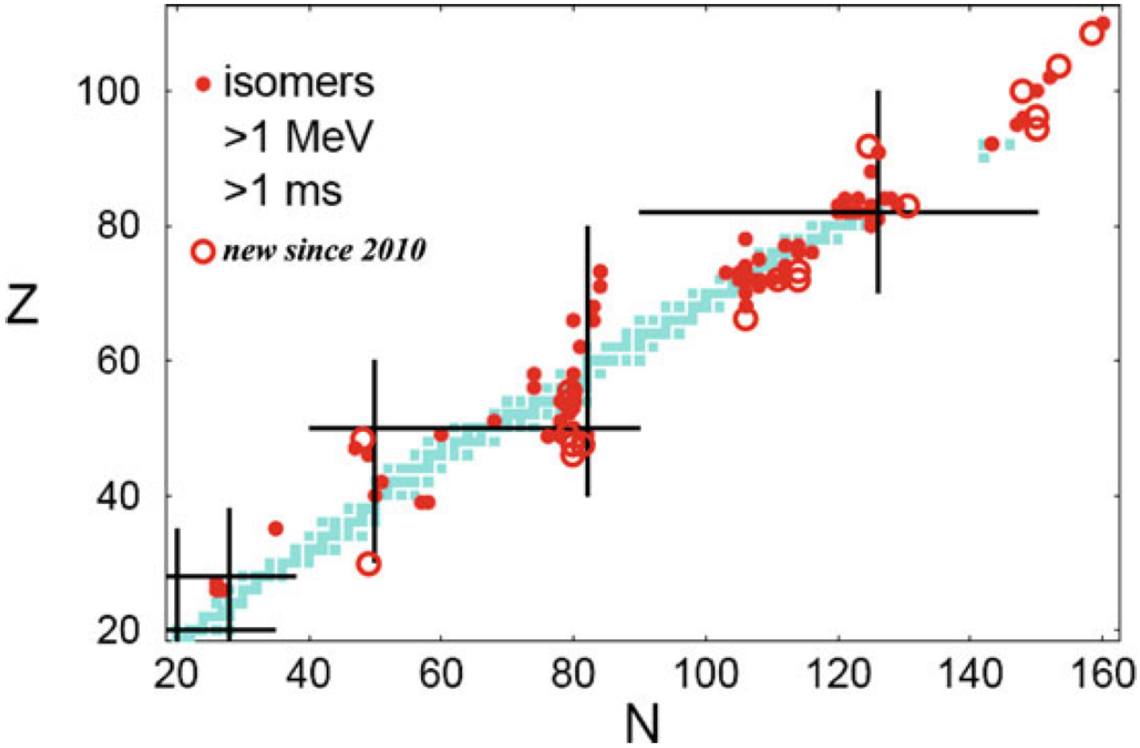

Figure 1.2: Nuclear chart illustrating known isomers with energies greater than 1 MeV and halflives larger than 1 ms. Discoveries made since 2010 are shown as red open circles, and earlier discoveries as red filled circles. The pale blue squares represent stable (and naturally occurring) nuclear ground states, and the black lines represent the closed-shell magic numbers [15].

rays or conversion electrons).

In the case of gamma decays, transitions are expressed in an extreme single-particle approximation using Weisskopf estimates [16, 17].

When an isomer undergoes beta decay, it is not easily distinguishable from a promptly decaying excited state that also decays via beta emission. The distinction can be made by investigating the energy, spin, and parity, or the half-lives of the isomers, as these can be either shorter or longer than those of the ground states.

Another possible decay branch is proton decay. A proton can be emitted from a nucleus when the emission is energetically possible. However, the probability of emission is low due to the Coulomb barrier and angular momentum. For this reason, the half-lives can be long, and other decay modes might compete. The first detection of proton radioactivity was from an isomeric state with $T_{\frac{1}{2}} = 250$ ms, $I_{\pi} = \frac{19^-}{2}$ in ^{53}Co, with a proton decay branch of 1.5% ([18] and subsequent detailed studies by [19]).

In the case of fission isomers, which are the focus of our work, the most favorable decay modes are alpha decay and spontaneous fission. In heavy nuclei (A > 140), there are many examples of isomers that decay via α emission [20, 14]. The heaviest case is the superheavy isotope ^{240}Ds [21]. This example is particularly interesting because the isomer is located at a relatively high excitation energy (1.1 MeV) and yet has a much longer half-life ($T_{\frac{1}{2}} = 4$ ms) compared to its ground state ($T_{\frac{1}{2}} = 0.2$ ms), so the isomer appears to be more stable than the ground state [22]. This suggests that new superheavy elements might be discovered in their highly excited isomeric states rather than in their ground states.

For the region of heavy elements (Z$\geq$ 90), decay predominantly occurs via spontaneous fission. This can happen in two different situations. The first situation involves normally deformed isomers, with deformations similar to their respective ground states. An example is ^{250}No [23], whose ground state undergoes fission with a half-life of 4μs, while its isomer has a half-life of 35μs, with less than 50% probability for the fission branch. Again, as seen similarly in cases of isomers that decay via α emission, it appears that fission of the isomeric state is disfavored compared to fission of the ground state [22]. The second situation involves superdeformed shape isomers that also decay via spontaneous, but delayed, fission. These "shape isomers" will be discussed in the next chapter.

1.1.2 Potential application of nuclear isomers

The study of nuclear isomers carries enormous potential for technological development. Long lived isomers, for example, are used in medical imaging [24], while others could potentially be used to store energy as "nuclear batteries" [25] or to create super-accurate clocks [26].

One application of nuclear isomers worth mentioning is the nuclear clock. It is appropriate to highlight this here not only because of its interest and potential technological implications, but also because many advances in this field have been made at the Medical Physics Chair of LMU [27].

Presently, and since 1967, the SI-unit "second" is defined as: 9192631770 times the period of the radiation emitted in the transition of the two hyperfine levels of the ground state in the isotope ^{133}Cs. This corresponds to a microwave wavelength, while modern and most precise optical atomic clocks exploit the about five orders of magnitude higher optical frequencies and reach relative uncertainties already entering the 10^{-19} regime. This corresponds to an inaccuracy of such clocks of 1 second over a period of about 30 billion years. The accuracy of such clocks is limited by the perturbative interaction of the atom with its environment. A clock based on the measurement of a nuclear transition would be more robust since nuclear levels are less affected by external fields due to usual smaller nuclear moments compared to the atomic ones. Because the measurement of transition energy relies on highly stable lasers, the energy must be orders of magnitude lower than that of typical nuclear excitations.

The isomer with the lowest known energy is ^{229}Th, which has an energy of only about 8.4 eV, corresponding to light with a wavelength of about 148 nm. Recently, enormous progress has been made in understanding its properties, but even measuring its excitation energy has been a challenge, requiring the development of new types of radiation detectors. The half-life of neutral ^{229}Th atoms is 7(1) μs [28], while when being in an ionized charge state, it has a predicted lifetime of $T_{\frac{1}{2}} \simeq 10^3$ s [29]. Recently, several measurements following radioactive decay of ^{229m}Th embedded in VUV (vacuum ultraviolet) transparent crystals resulted in lifetime values (re-scaled for vacuum conditions) of about 2000 s. For these reasons, using the nuclear transition of ^{229}Th could lead to the construction of a clock more accurate than any other [30]. Furthermore, the development of a nuclear clock with a predicted precision of 10^{-19} [31] would have important implications for both fundamental physics—such as investigating the temporal variation of fundamental constants or the search for ultralight dark matter candidates—and applications like gravity sensors [32, 33]. We can only wait for the subsequent developments of this fascinating project.

1.2 Production and separation methods for exotic nuclei

The reason to revisit in this thesis work a discovery made 100 years ago for a PhD project is that, thanks to recent developments in nuclear detectors, rare beam facilities, reaction analyzers, and digital electronics, as well as in computational power, nuclear isomers have returned into the focus of nuclear physics research. To study isomers in unstable or very heavy nuclei species via novel reaction schemes, we need to produce so-called exotic nuclei. Exotic nuclei are atomic nuclei that exhibit unusual properties compared to stable nuclei commonly found on Earth. These properties can include an unusual combination of protons and neutrons, often extending towards very high numbers of neutrons or protons, or presenting a deformed or metastable nuclear structure. Exotic nuclei can also show binding energies, nuclear sizes, and decay modes that significantly differ from more common nuclei. In order to study them, they need to be produced. Below, we will consider the factors involved in their production, the nuclear reactions used, and the separation methods applied for the resulting reaction products.

1.2.1 Reaction mechanisms

The reaction schemes used to generate "exotic" nuclei have emerged at different times, starting from the late 1900s, depending on the type of decay favored in a particular area of the nuclide chart, as shown in Fig.1.3.

Today, there are two widely used processes for producing exotic nuclei, with a third process currently being explored. These processes are:

- the fusion of a light nucleus with another nucleus, occurring at energies close to the reaction threshold,
- the fragmentation of a heavy nucleus by a very light nucleus at relatively high kinetic energies ("in-flight fragmentation"),
- multinucleon transfer between two heavy nuclei, which can occur at the Coulomb barrier.

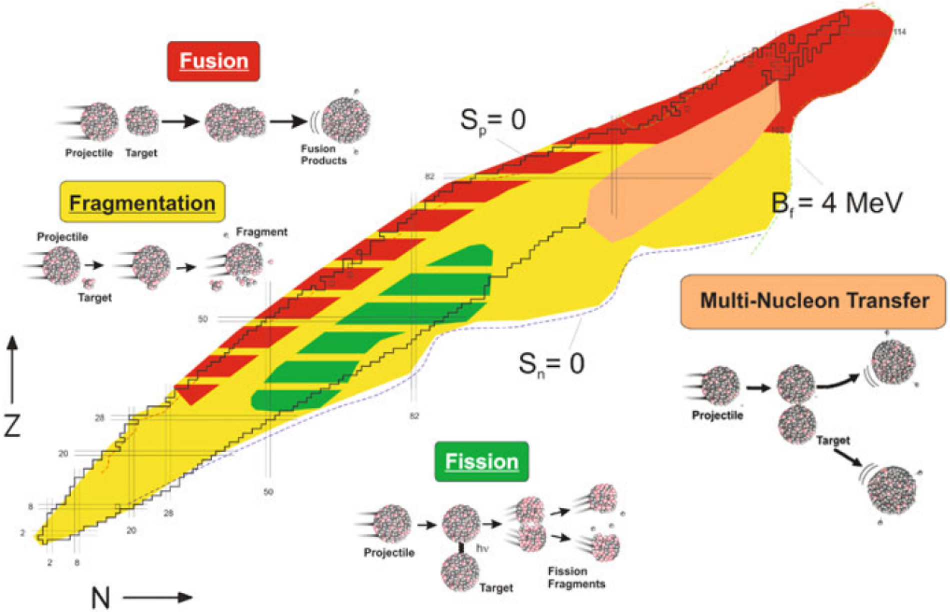

Figure 1.3: Chart of Nuclides with schematic representation of the present extent of known nuclei within the black bold line and the theoretically existing nuclei confined by the dotted between the driplines where the neutron and proton separation energy vanish $S_{n,p} = 0$. Additionally shown are the regions in which various nuclear reaction schemes are predominantly used or predicted to produce exotic nuclei [34].

Additionally, very heavy nuclei produced in any reaction can undergo fission, producing neutron-rich, medium-mass products.

1.2.2 Production techniques

The techniques to separate exotic nuclei are designed to their production rate, which depends mainly on the production reaction used and on the cross section involved in the process. For example, when considering cross sections, fusion reactions used to produce superheavy nuclei have extremely low cross sections, typically in the range of picobarns (10^{-12} barns) to femtobarns (10^{-15} barns), whereas fragmentation reactions can have much higher cross sections in this mass region (range of millibarns (10^{-3} barns) or even larger. When we consider a production reaction and an associated separation technique, we refer to them as production techniques. Two techniques are commonly used nowadays: isotope separation online (ISOL) and in-flight separation. In both techniques, a mixture of exotic nuclei is produced in nuclear reactions between the accelerated beam of projectiles and a target. The reaction products are transported away from the high-background reaction site, and are purified and prepared to meet the requirements of the experimental setups downstream. The techniques are complementary, and each has its advantages and drawbacks. In the ISOL method, exotic isotopes are produced through target fragmentation reactions, such as spallation or fission. A high-energy proton beam (up to 4 GeV) with high intensity (up to 100μA) strikes a thick target (with an areal density on the order of several $10\frac{g}{cm^2}$), where the reaction products are stopped and thermalized. These nuclei are then extracted from the target in the form of ions, mass-separated, and finally re-accelerated to the desired energies by a secondary accelerator (post-accelerator). The resulting radioactive ion beams (RIBs) are directed onto a secondary target to induce nuclear reactions and perform spectroscopic measurements. The advantages of this method include a high production rate of exotic beams, and the ability to freely choose the post-reacceleration energy, providing thermalized ions ready for low-energy experiments. However, there are also disadvantages: the efficiency of the produced isotopes heavily depends on the chemical properties of the released elements, and isobaric contamination of the secondary beam cannot be completely suppressed. This latter issue can be addressed by using multiple-reflection time-of-flight mass spectrometers (MR-TOF-MS) as high-resolution isobar separators, such as at TRIUMF's Ion Trap for Atomic and Nuclear sciences (TITAN) [35, 36] and at the Isotope Separator On-Line Device (ISOLDE) [37] facilities, or by employing selective laser ionization techniques (see [38]).

In the In-Flight method, heavy ion beams with energies ranging from 100 MeV up to 1 GeV per nucleon strike a thin primary target (with an areal density of up to $10\frac{g}{cm^2}$). The kinetic energy of the projectile beam is close to the Coulomb barrier for fusion reactions and above the Coulomb barrier energy (in the GeV/u region) for projectile fragmentation and fission reactions. The fragments produced emerge ionized from the target and with a velocity similar to the projectile beam; these products are then rapidly separated in flight ($\leq 1\mu$s) according to their masses and charges, and finally directed to high-energy experiments for spectroscopic and reaction studies or to induce secondary reactions without additional acceleration. In the case of fusion, Wien filters or fragment separators are used for separation (see [39, 40]), while for fission and projectile fragmentation reactions, fragment separators are used, such as the FRagment Separator (FRS) [41] at GSI. The In-Flight method also has the significant advantage of providing a clean isotope beam free from isobaric contamination due to the high energy of the fragments, which also makes event-by-event identification possible, allowing for the use of cocktail beams.

These two techniques (summarized in Fig. 1.4) prove to be highly complementary. The first one is limited to radioactive ion beams (RIBs) with long half-lives, greater than 1 ms, due to the time required to extract the radioactive nuclei from the thick primary target and transport them to the ion source. However, the ISOL method produces high-quality RIBs over a wide range of energies, from a few tens of keV to about 100 MeV per nucleon (after post-acceleration).

The In-Flight method allows for the production of RIBs with short half-lives, down to a few hundred nanoseconds. These beams, however, tend to be of lower quality (i.e., with a large angular and momentum spread of the ions, requiring cooling for low-energy experiments) and are limited to energies close to those of the primary stable beam, in a range from 100 MeV to 1 GeV per nucleon. The beam quality could be improved through cooling techniques, e.g., in a storage ring, but the cooling time is in the order of few seconds [43] and in this case the advantage of fast in-flight production is lost.

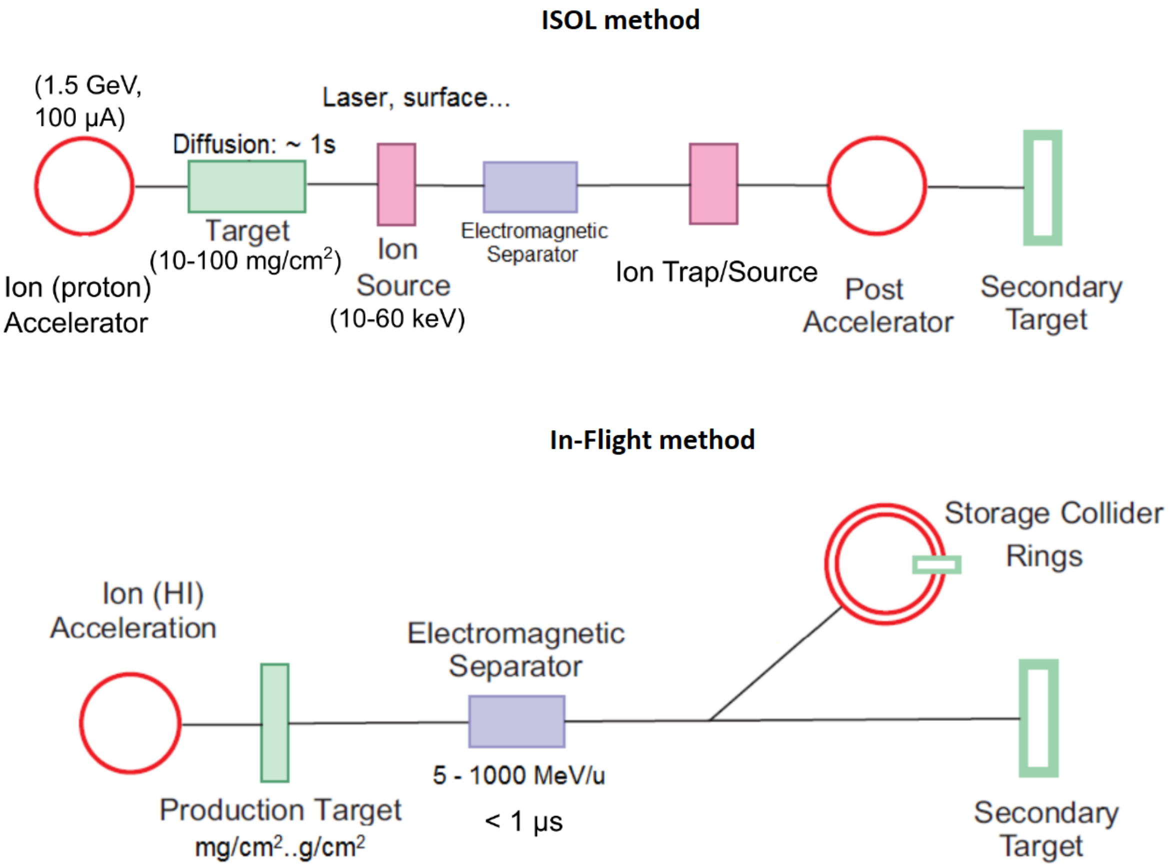

Figure 1.4: Schematic outline of the ISOL (upper part) and In-Flight (bottom part) production technique for radioactive ion beams. Adopted and modified from [42].

By coupling these two complementary techniques, a hybrid method is obtained, where exotic nuclei are produced at relativistic energies but used for low-energy experiments, as is done at the FRagment Separator (FRS) at GSI [41]. Exotic nuclei are produced using the in-flight method at relativistic speeds and then pass through a cryogenic gas cell (CSC) that thermalizes and slows the produced nuclei down to keV energy range. They are subsequently extracted within a time frame of 10 to 100 ms and sent to a low-energy experimental setup. This allows for low-energy experiments (as in the ISOL technique) using a clean and short-lived beam (as with the in-flight method). A hybrid technique of this kind is employed at the FRS Ion Catcher at GSI (a schematic outline of the hybrid technique is shown in Fig. 1.5), where a cryogenic gas cell (CSC) is used to slow down the beam and direct it to a mass spectrometer, here the multiple reflection time of flight mass spectrometer (MR-ToF-MS), which will be discussed extensively in the next chapter. However, this method brings with it technical complexity due to the integration of various technologies. Therefore, hybrid techniques can also be combined differently depending on the prerequisites of the facility.

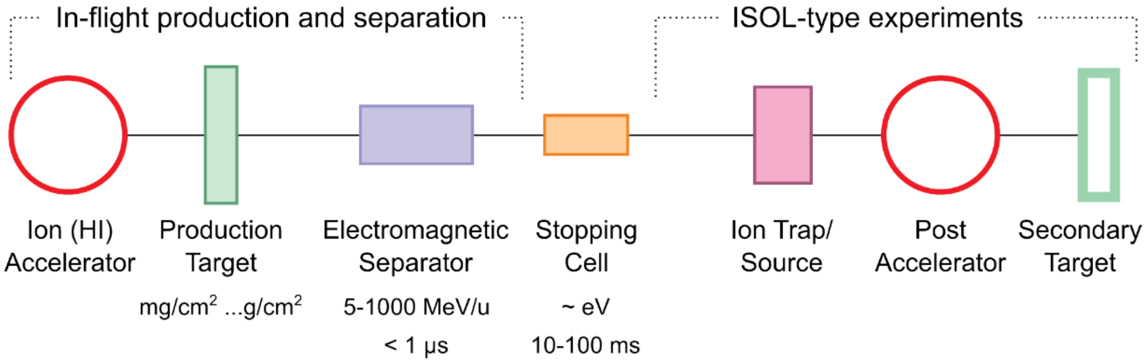

Figure 1.5: Schematic outline of the hybrid technique for production of exotic ion beams. Adopted and modified from [42].

As another hybrid method we can also consider the upgrade of the ISOL method that improved over the years since its invention at the Niels-Bohr Institute in Kopenhagen in 1951 for the production of $^{89-91}Kr$. The main adaptations to the ISOL method have been developed to compensate for the slow extraction process. One of these is the IGISOL method (Ion Guide Isotope Separator On-Line) developed and set up at the accelerator laboratory of the University of Jyväskylä in Finland, which in its latest version, IGISOL-4 [44], utilizes a laser ion source [45]. This technique collects the recoil nuclei produced in a nuclear reaction using the ISOL method and neutralizes them in a high-pressure gas cell, typically filled by helium, sometimes by argon. The selected ions are transported by a gas flow out of the gas cell and injected through a differential pumping electrode system into the high-vacuum section of the isotope separator for further acceleration and mass-based separation, as shown in Fig. 1.6. Selection is achieved using a laser system that selectively re-ionizes only the element of interest among those in the cell. When the ions are slowed down in the gas, their charge state is constantly reset in charge-exchange collisions determined by their velocity, the type of gas, and its purity. The conditions in which the ions are slowed down vary significantly for different reactions, as well as due to plasma effects from the composition of different processes leading to neutralization or other ion losses during their transport in the gas. In the most recent versions of IGISOL [45], to overcome the shortcomings of plasma effects and to provide selectivity based on atomic number (Z), a laser ionization technique is used (proposed in the early 1990s and developed further by the Leuven group [46]) that re-ionizes only the element of interest among those collected in the cell. A schematic picture of this method is shown in Fig.1.6.

This technique overcomes some limitations of the traditional IGISOL method, particularly providing Z-selectivity (by atomic number) and improving efficiency, especially for fission reactions. It is particularly useful for studying refractory elements and reactions that produce a wide range of products, such as fission reactions. However, this technique can also have disadvantages. It requires specific laser ionization schemes for each element, which can limit its application.

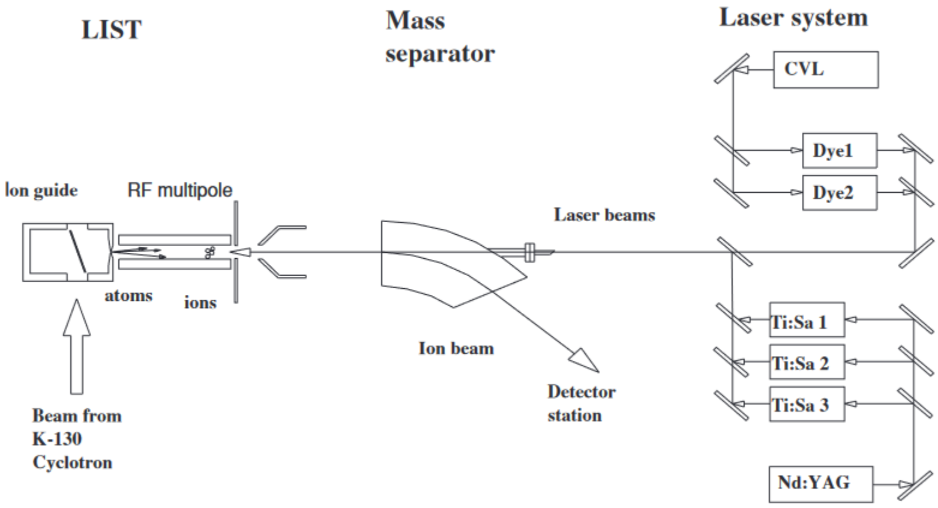

Figure 1.6: Schematic view of the laser ion source trap at IGISOL [45].

In summary, each technique has its benefits and drawbacks, but by combining multiple techniques and instrumentation (such as mass spectrometers and cooling devices), techniques can be tailored to the studies to be undertaken. In particular, the use of multiple reflection time-of-flight mass spectrometers (MR-TOF-MS) and selective laser ionization aims to further improve the selectivity and efficiency of these techniques, addressing the issue of isobaric contamination in ISOL techniques. Meanwhile, integrating these techniques with cooling and storage devices opens new possibilities for precision experiments and applications with exotic nuclei.

1.3 Introduction to GSI and JYFL

Here we provide a general description of two research institutes that produce exotic nuclei: GSI in Darmstadt, where the FRS Ion Catcher with the hybrid technique is located, and the accelerator laboratory of the University of Jyväskylä (JYFL) in Finland, where the IGISOL facility can be found. We choose these two because they are the facilities where the experiments described in the following chapters were conducted.

1.3.1 GSI

The GSI Helmholtz Centre for Heavy Ion Research placed at Darmstadt, founded in 1969 as Gesellschaft für Schwerionenforschung mbH, is a world-leading research facility dedicated to the study of heavy ions. GSI's primary mission is the construction and operation of accelerator facilities conducting research on exotic nuclei in fields from fundamental physics to medical and space science applications. Additionally, GSI operates several large spectrometer and detector systems, and participates in the ALICE detector project at

CERN.

In the facility, a primary beam of stable ions is produced and accelerated up to ~ 11.4 MeV/u at the UNIversal Linear ACcelerator (UNILAC) [47]. From here the beam can be directly sent to some downstream experiments or can be injected to the heavy-ion synchrotron (SIS$-$18) [48] for further acceleration of the ions to relativistic energies (from $3-20$ MeV/u up to $1-2$ GeV/u) and then directed to the Fragment Separator FRS [41] where secondary ion beams of exotic nuclei are produced via the in-flight technique (as introduced in Sect. 1.2). The isotopes of interest are filtered and delivered to the experimental stations downstream, in the case of our interest to the FRS Ion Catcher [49, 50]. Figure 1.7 shows a layout of the GSI facility, including the additions presently under construction in the context of the FAIR project [51].

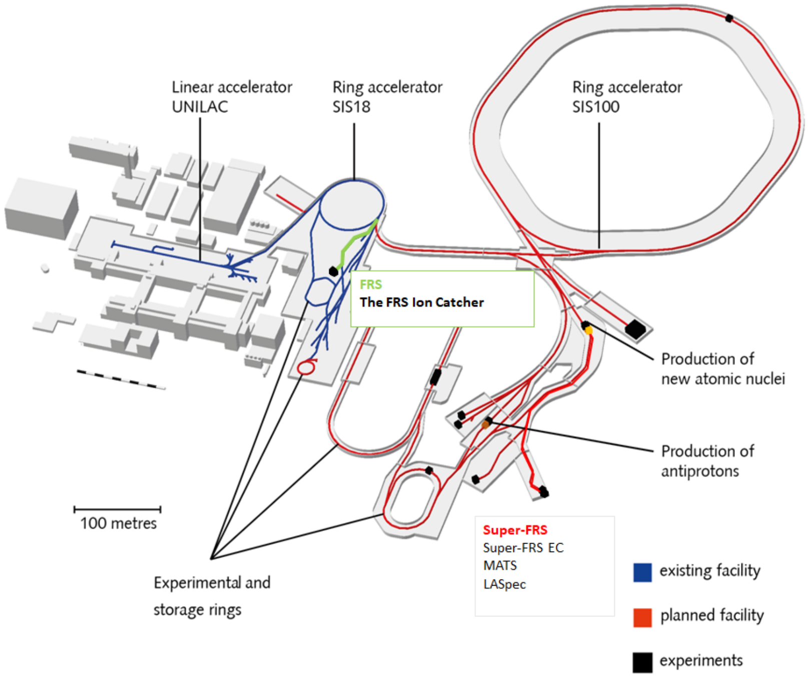

Figure 1.7: Schematic layout of the GSI facility. It mainly consists of the heavy-ion linear-accelerator UNILAC, the heavy-ion synchrotron, presently existing is SIS$-$18 and under construction SIS$-$100 , the fragment separator FRS and the (under construction) Super Fragment Separator (S-FRS). The FRS Ion Catcher is positioned at the final focal plane of the FRS [Picture for presentation shared within the FRS Ion Catcher group].

1.3.2 FRagment Separator (FRS)

In the FRS, the relativistic ion beam bombards a production target producing exotic nuclei via projectile fragmentation and fission reactions. The secondary beam is then separated in-flight and delivered to different experiments downstream such as to the FRS-IC. A schematic view of the FRS and the FRS Ion Catcher is shown in Fig. 1.8.

The FRS consists of two similar magnetic separation stages. Each stage has two dipole magnets for magnetic rigidity analysis and a set of quadrupole and hexapole magnets for focusing of the beam and ion optical corrections. At the end of each stage there are slits to control the variety of selected ions. A profiled aluminum degrader is located at the mid-focal plane between the two separation stages and a variable degrader is installed at the end of the FRS in the final focal plane.

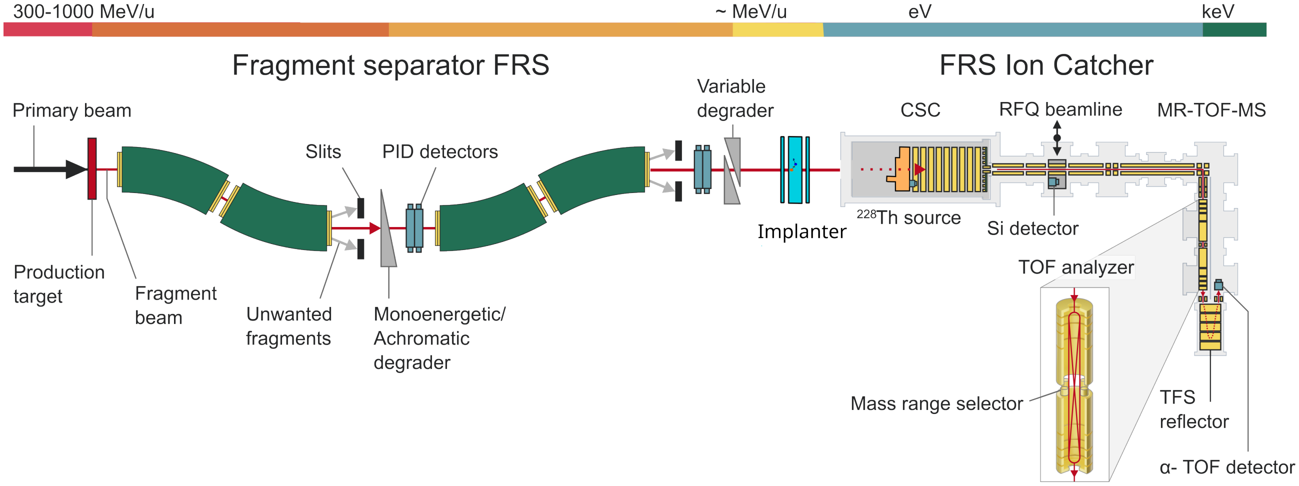

Figure 1.8: Schematic drawing of the experimental setup showing the Fragment Separator (FRS) combined with the FRS Ion Catcher (FRS-IC) at GSI as it was during the experiment S530 discussed in this work. [Adapted for S530 settings from a picture made by D. Amanbayev]

The relativistic beam of exotic radioactive isotopes emerges via projectile fragmentation and/or fission reactions typically fully-stripped as fragments from the target. The fragments are separated and filtered by crossing the FRS's stages using a $B\rho - \Delta E - B\rho$ method. At the first magnetic stage, fragments are separated by their magnetic rigidity $B\rho$, this means the ions are selected accordingly to the mass-over-charge ratio (m/q). Then they meet the wedge shaped aluminum degrader to reduce part of their energy (energy loss is $\Delta E \sim Z^2$). At this point at the last stage, the magnetic rigidity becomes isotope-specific, so isotope separation is achieved. Tuning by the angle of the wedge-shaped degrader at the mid-focal plane, the FRS can provide an achromatic (standard) mode or monoenergetic modes [Geissel et al., 1989]. The achromatic mode is optimal for the isotopic separation, but has a large range straggling. That is why it is preferable to use the monoenergetic mode when the FRS is combined with the FRS-IC, since in this way a larger number of ions can be stopped in the cryogenic stopping cell (the CSC being the first part of the FRS-IC system). The installation of the variable degrader at the end of the FRS and just before the CSC allows to use the achromatic mode by correcting the range position dependence, such that the CSC is capable to handle a cocktail beam (see Fig. 1.9 [52]).

A large number of detectors is installed all along the FRS for the in-flight particle identification (PID) and intensity monitoring. The intensity of a primary beam is mea-

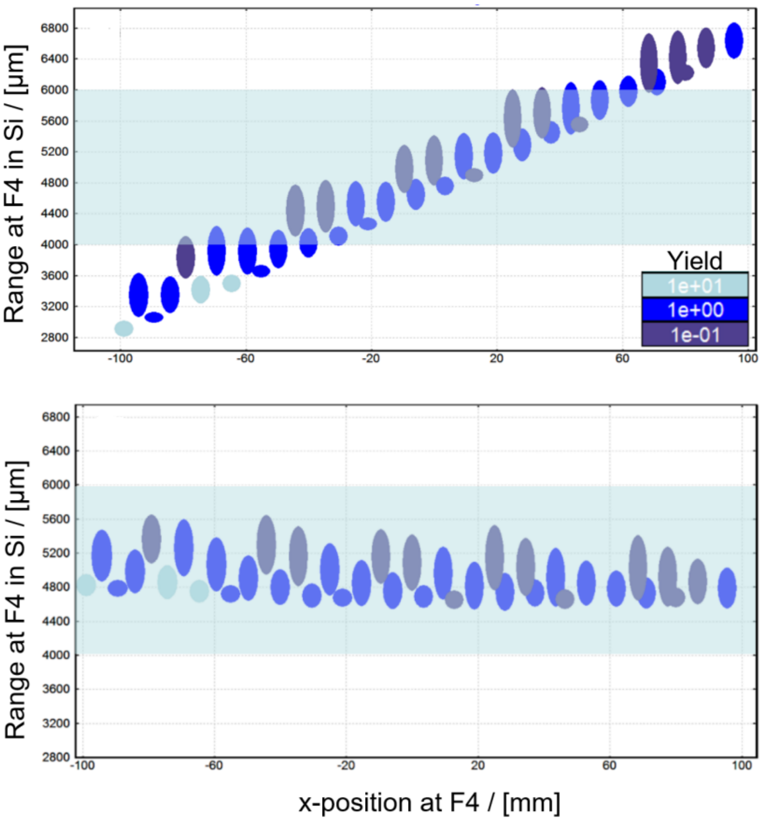

Figure 1.9: The ellipses in this figure panels show the ion straggling range versus the CSC length. The upper plot refers to normal operation of the FRS and uses achromatic optics. With this mode, only few nuclides can be stopped in gas simultaneously. The bottom plot shows the case when the degrader is used to "correct" the range/position dependence and in this case the CSC can handle the cocktail beam (the beam is completely stopped in the CSC) [52].

.

sured with a secondary electron transmission monitor (SEETRAM). The PID achieved by a combination of plastic scintillators (SCI) measuring time-of-flight and intensity of the fragments [53] and of a time-projection chamber (TPC) measuring position and angle of the fragments [54]. Together they provide information on the mass-over-charge ratio m/q. The installation of a further detector, a multiple sampling ionization chamber (MUSIC) detector provides information about the atomic number Z by measuring the energy deposition of ions in gas [55, 56]. The FRS-IC setup will be in detail explained in Chapter 4.3 together with technical improvements achieved as preparatory developments which enable the experiments presented afterwards.

1.3.3 JYFL

The JYFL Laboratory of the University of Jyväskylä is a Finnish national research facility with an extensive international program in education and research on atomic nuclei under extreme conditions as well as related applications [57]. For these purposes the JYFL cyclotron (AVF, K130) with its ion sources delivers, together with GSI, GANIL and ISOLDE facility, the largest variety of light and heavy ion beams in Europe. The facility has proven to be very reliable, providing up to 7000 hours of beam hours per year. Multiple instrumentations are available, but this job is focused on the IGISOL facility since one of the two experiments presented in the framework of this thesis was performed at IGISOL. IGISOL delivers various species of cooled and bunched radioactive ion beams to beam lines equipped with ion traps for accurate nuclear-mass measurements, detector systems for exotic decay modes and laser-spectroscopy systems for hyperfine-structure studies. Radioactive beams from IGISOL are also used for applications, such as studies of atomistic transport processes in nanoscale solids.

1.3.4 IGISOL

The Ion Guide Isotope Separator On-Line (IGISOL) facility, particularly in its upgraded IGISOL−4 version [44], uses a sophisticated method to produce and handle exotic nuclei. The facility's process begins with a light-ion (mostly proton) projectile beam, generated from either the K130 or MCC30 cyclotron, which strikes a thin target, causing reaction product nuclei to recoil into a fast-flowing buffer gas, usually high-purity helium. These recoil ions are slowed down and thermalized through collision processes in the buffer gas, achieving a singly-charged state with an efficiency ranging from 1 to 10%.

The helium gas flow then guides the ions through a nozzle exit into a subsequent radiofrequency sextupole ion beam guide (SPIG), which operates at a frequency of $3-4$ MHz and an RF amplitude up to 600 V. The SPIG not only enhances the quality of the ion beam by phase space cooling, but also improves the transmission efficiency from the ion guide to the mass separator, with a maximum transmission of up to 100% for currents around 100 nA, although efficiency drops to 50% at higher currents of approximately 600 nA. The extracted ions are then electrostatically accelerated using a 30 keV potential. The ion guide operates at a pressure range between 100 and 300 mbar, with the optimal pressure selected to maximize production for each reaction. In addition to online production, an offline ion source station is available to provide stable ion beams during measurements. This station includes a surface ion source and a glow discharge ion source. The surface ion source produces ions by heating a mixture of potassium, rubidium, and cesium, while the glow discharge ion source ionizes the helium buffer gas through high-voltage discharge sparks, causing fragmentation of the cathode material. Both online and offline ion beams are mass-separated using a 55-degree dipole magnet with a resolving power of $\frac{M}{\Delta M} \simeq 500$. Once mass-separated, the ion beam is directed to various stations, such as the decay spectroscopy line, the cesium atom trap station, or the radiofrequency quadrupole (RFQ) cooler-buncher. In the cooler-buncher, ions are decelerated to about 50 eV and focused into a quadrupole using electrostatic lenses. The ions undergo repeated collisions with helium atoms (at a pressure of ~ 0.1 mbar) to improve their emittance and reduce their energy spread to below 1 eV. The ions are trapped at the end of the cooler by a potential barrier and accumulated for a few hundred milliseconds. They are then released in 100μs bunches, with the individual bunch having a temporal width of $10 - 20$ μs at an energy of 800 eV into either the laser line or the Penning trap facility JYFLTRAP. The transmission efficiency through the cooler-buncher is $60 - 70\%$. The bunched beam offers significantly lower background levels compared to a continuous ion beam, improving the accuracy of time-of-flight (TOF) measurements.

1.4 Motivation

The actinide region offers a fertile ground for investigating superdeformed nuclear shapes due to the interplay between strong shell effects and deformation-driving forces while still being in a regime of low angular momenta. This field has been investigated since the discovery of first isomers about 100 years ago, but today new technology offers new ways to investigate this region.

In this work two exploratory experiments are presented. The first was performed at the Fragment Separator (FRS) and the FRS Ion Catcher based at GSI, and at the IGISOL facility at the JYFL Laboratory of the University of Jyväskylä in Finland.

In the first case measurements have been conducted to explore the feasibility of producing strongly deformed nuclei in the actinide region via the projectile fragmentation technique. The selected approach leverages projectile fragmentation of a ^{238}U primary beam at 1000 MeV/u, combined with advanced separation and identification techniques of reaction products provided by the Fragment Separator (FRS) and then stopped inside a cryogenic stopping cell before being extracted into a diagnostics section for decay spectroscopy or Time-of-Flight mass spectrometry.

Technological development for the stopping cell has to be performed (based on existing concepts and preparatory work) to reduce the ion extraction time from the cell down to 10 ms to allow for measuring the short–lived fission isomers and to increase the rate capability to allow for a larger beam rate acceptance. The commissioning and the experimental status of the technical improvement are presented together with the related experimental results.

On the other side, also the data acquisition has been developed suiting new detector technology and decay signal identification is achieved introducing new methodology.

In the second experimental campaign at IGISOL in Finland, the isomers ^{240f}Am and ^{242f}Am have been studied.

The ^{242}Am fission isomer, with a half-life of approximately 14 ms, is the longest-lived known fission isomer, making it a crucial subject for studying double-humped fission barrier properties. Previous studies using the $^{242}\mathrm{Pu(d, 2n)}^{242}$Am reaction have identified peak production energies in a range of 7 to 12 MeV, while the theoretically predicted value is 13.8 MeV. In this case further measurements are required to refine the peak production

rate.
This experiment served as an investigation to validate the methodology for producing ^{242f}Am and ^{240f}Am, while also exploring the feasibility of measuring the excitation energy of ^{242f}Am. Additionally, it aimed to determine the half-life and the isomer-to-ground state ratio for both ^{240f}Am and ^{242f}Am. These measurements are critical for improving our understanding of fission barrier parameters, such as the barrier height and decay branching ratios.

Furthermore, the investigation of ^{242}Am provides insights for the Nuclear Excitation by Electron Capture (NEEC) process. NEEC is a process in which an atomic nucleus is excited by the capture of a free electron by a highly charged ion. During this capture, the energy released by the electron in binding to an atomic orbital is not emitted as a photon, as in the case of radiative capture, but is transferred directly to the nucleus [58, 59, 60]. The nucleus ^{242}Am has two isomeric states within its energy levels. The first has an excitation energy of 48.63 (5) keV and an average lifetime of 141 (2) years and decays mostly (99.5 %) via isomeric transition (IT). A second isomeric state with excitation energy 2200 (80) keV, average lifetime 13.9 (2) ms and a probability of decay of about 100 % via spontaneous fission (this last isomer will be considered in the following chapters).

Looking at the isomeric state as energy storage state, it is interesting to control their decay for many application as for example a nuclear battery application. The NEEC, as controlled process could be a favourable mechanism to use in this regards. The first of the two isomeric state for the ^{242}Am, it is a strong candidate for the NEEC process due to its low excited states compared to other isomeric state, since it is easier to reach.

The outcomes of this study are expected to contribute significantly to advancing methodologies in nuclear structure physics of heavy, strongly deformed nuclides and enriching our comprehension of exotic nuclear states.

Chapter 2

Superdeformed nuclear shapes in the actinide region

2.1 Introduction to Fission Isomers

Nowadays it is well known that a nucleus can adopt various shapes, from simple spherical configurations to more complex and deformed ones, depending on factors as the N and Z configuration, excitation energy and angular momentum. These distinct shapes emerge due to the presence of additional minima in the nucleus's potential energy surface, beyond the ground state minimum, when the energy is mapped across different degrees of freedom. When a heavy, fissile nucleus assumes a secondary minimum with a shape distinct from its ground state, it can back-decay into the deformed first minimum or by delayed fission. These isomeric states are known as *shape isomers*.

A specific category of shape isomers, called *fission isomers*, occurs in the heavier actinides region, which can decay through alpha decay or spontaneous fission. Fission isomers are characterized by super-deformed shapes and represent the first instances of super-deformation at low-spin states. In this context superdeformation is defined as a nuclear deformation parameterized by a quadrupole deformation parameter $\beta_2 \simeq 0.7$, equivalent to a ratio of semi-minor to semi-major half axis in a rotational ellipsoid of $1:2$.

The first isomer to undergo spontaneous fission was unexpectedly identified in ^{242}Am by Polikanov et al. [61], during an investigation of the properties of short-lived heavy nuclei. In this experiment, a beam of heavy ions (either ^{16}O or ^{22}Ne) produced by the Dubna cyclotron was directed on a thin ^{238}U target. The reaction products were expelled from the target at high speeds and subsequently captured by a rotating collector, which passed through two ionization chambers designed to efficiently detect fission fragments. Special care was taken to ensure that only the signals corresponding to fragments originating from the ^{238}U were recorded. Analysis of the pulse spectrum and fragment range confirmed the occurrence of delayed fission, with a measured half-life, now determined to be 14 ms [61], 100% decay via spontaneous fission (SF) was observed.

The isotope ^{242}Am was already known to exist in two states: a ground state and an isomeric state with an excitation energy of 48 keV. The ground state decays either via β^- decay or K-electron capture, with a half-life of 16 hours, whereas the isomeric state has a much longer half-life of 141 years and a partial half-life for spontaneous fission (SF) of 9.5×10^{11} years. The detection of an isomeric state with a SF half-life of 14 ms at 100% suggested an extreme reduction in the half-life by a factor of 10^{20}, challenging the conventional understanding of the fission barrier [61].

Moreover, the fact that the isomer ratio remained constant, irrespective of the angular momentum introduced by various reactions such as (p, n), (α, 2n), (n, 2n), or (^{11}B, $\alpha 3n$), ruled out the hypothesis that the stability was due to a high-spin isomer resisting gamma decay [62]. Additionally, the proposed theoretical explanation that stability originated from nuclear matter in a superfluid state near the ground state was contradicted by the excitation threshold energy of the isomer, which indicated an excitation energy in the MeV range.

While some nuclei possess two known fission isomers, some of them also exhibit a rotational band built on the isomeric state. These isomers show an intermediate group structure, an interesting phenomenon observed in the cross section of fission with cold neutrons. The first observation of this phenomenon dates back to 1968 [63], when Fubini et al. bombarded slow neutrons on ^{237}Np and measured both the total cross section and the fission cross section. The total cross section displayed a behavior similar to that of other odd-mass nuclei with $A = 237$, but the fission cross section presented numerous peaks, each composed of several resonances at defined energies. This phenomenon can be explained if the potential energy function has two minima. In the absence of a second minimum, resonances are due to the energy levels of the compound nucleus formed in neutron capture. However, the existence of a second minimum introduces the possibility that the ground state of the second well is 2-3 MeV higher than that of the first one, with the captured neutron providing at least 5 MeV of excitation energy. This leads to the formation of a shape isomer, such as a second ground state at least 2-3 MeV above the first ground state. Whenever the excitation levels in the first well coincide with those of the first, greater barrier penetration occurs. Since the second well is shallower, its levels are more spaced apart than those of the first, creating a fine structure superimposed to the cross section.

By the time of the observations mentioned above, the description of a potential energy function with multiple minima was not predicted by the liquid drop model. Only thanks to Strutinsky's [64] insight, which introduced shell effects into nuclear energy calculations, was an additional local minimum was observed in the potential function, termed superdeformed, at a deformation corresponding to an aspect ratio of approximately 2:1, approximating the nuclear shape to a rotational symmetric ellipsoid. This observation clarified the existence of a shape isomer that decays via fission from a locally deformed minimum as previously proposed by Polikanov et al. [61] and by Flerov and Druin [65]. From the excitation function of delayed fission yield compared to prompt fission yield, valuable information was derived regarding the ground state's energy. Furthermore, fission barrier calculations incorporating Strutinsky's corrections revealed additional candidates for fission isomers, which occupy a region from $Z = 92$ to 97 and from $N = 141$ to 151, known as the

”uranium-berkelium island” or the ”island of shape isomers.”

In the following sections, we will explore shape isomers in actinide nuclei. We will begin with general considerations on fission, introducing the liquid drop model (LDM) and the shell corrections (SCM) introduced by Strutinsky. Based on experimental evidence of even a third (hyperdeformed, axis ratio 3 : 1) minimum, we will examine the potential energy surface (PES) function and the Brosa method for multimodal fission, focusing on fission isomers. Finally, we will introduce the experimental campaigns studied in this thesis.

2.2 Considerations on Nuclear Fission

In this section, we want to explore why nuclei undergo fission and the peculiarities of this process, justifying the need to add shell effects to the liquid drop model.

For a nucleus to fission spontaneously, the final state must be energetically favored. Consider a heavy nucleus in the uranium region, for example ^{238}U, which has a binding energy of about 7.6 MeV per nucleon. If ^{238}U were to split into two equal fragments with A= 119, their binding energy per nucleon would be around 8.5 MeV. Therefore, the energy would transition from the bound system of ^{238}U with energy:

$$238 \times 7.6\ MeV = -1809\ MeV$$

to two bound nuclei of ^{119}Pd with energy:

$$2 \times 119 \times 8.5\ MeV = -2033\ MeV.$$

The energy difference between the two systems must be compensated by the law of energy conservation, which occurs through the emission of neutrons, β emissions, γ emissions, but mainly ($\sim$ 80%) as kinetic energy of the fragments, as the Coulomb repulsion separates them.

The probability of decay is proportional to the energy release. Therefore, a large energy release, such as the one predicted for the fission of nuclei rising along the binding energy curve, should favor this reaction. However, this does not happen. Although the fission decay process exists, it does not compete successfully, for instance, with the spontaneous α-decay of ^{238}U (with $t_{1/2} = 4.5 \times 10^9$ years, while the partial half-life for fission is about 10^{16} years), and it does not become an important decay process until reaching nuclei with a mass of 250 or greater.

What inhibits the fission process is the Coulomb barrier. If we split ^{238}U into two identical fragments that barely touch (separation = $R_1 + R_2$, where $R_1 = R_2 = 1.25 fm \cdot (119)^{1/3} = 6.1\,\mathrm{fm}$), the Coulomb barrier is:

$$V = \frac{1}{4\pi\epsilon_0}\frac{Z_1 Z_2 e^2}{R} = \frac{(1.44\,\mathrm{MeV}\cdot\mathrm{fm})\cdot(46)^2}{12.2\,\mathrm{fm}} = 250\,\mathrm{MeV}.$$

Therefore, the 224 MeV of our bound system of two ^{119}Pd nuclei does not have enough energy to overcome the Coulomb barrier, and thus the probability of fission decay is low because the barrier cannot be penetrated.

This situation is shown in Fig. 2.1, where the potential energy of the system is plotted as a function of the separation distance.

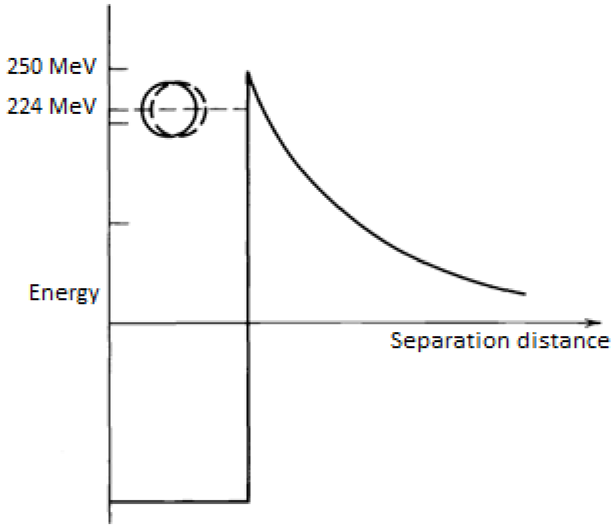

Figure 2.1: Potential energy of the nucleus of ^{238}U as a function of the separation distance [66].

However, for many reasons (for instance, the calculation of the barrier and the nuclear energy are only estimates, the mass split of fragments normally will be asymmetric, etc.), this calculation is approximate.

An instructive approach to understanding fission can be obtained from the semi-empirical Bethe-Weizsäcker mass formula, derived within the liquid drop approach

$$E_{\mathrm{B}} = a_{\mathrm{V}}A - a_{\mathrm{S}}A^{2/3} - a_{\mathrm{C}}\frac{Z(Z-1)}{A^{1/3}} - a_{\mathrm{A}}\frac{(N-Z)^2}{A} \pm \delta(N,Z).$$

The formula below consists of 5 terms:

1. **Volume energy $a_{\mathbf{V}}A$**: Proportional to the volume, it reflects the attractive interaction among nucleons packed into the smallest possible space with an interaction exclusively confined to nearest neighbors.

2. **Surface energy $a_{\mathbf{S}}A^{2/3}$**: Correcting for the assumption of uniform nucleon interaction, this repulsive negative term is proportional to the surface area, analogous to liquid surface tension.

3. **Coulomb energy $a_{\mathbf{C}}\frac{Z(Z-1)}{A^{1/3}}$**: Represents the repulsive potential energy from the Coulomb interaction between proton pairs, reducing the overall binding energy.

4. **Asymmetry energy $a_{\mathbf{A}}\frac{(N-Z)^2}{A}$** (also called Pauli energy): Accounts for the Pauli exclusion principle, indicating that unequal numbers of neutrons and protons lead to higher energy levels being filled while leaving lower levels vacant.

5. **Pairing energy** $\delta(N, Z)$: This accounts for the energetically favored tendency of proton pairs and neutron pairs to occur. An even number of particles is more stable than an odd number due to spin coupling.

Let us examine the impact on the binding energy of a nucleus that is initially spherical and is gradually elongated. This elongation can occur while maintaining a constant volume, but the surface and Coulomb energy terms, which were originally calculated for spherical nuclei, will be influenced by this stretching. We represent the elongated nucleus as a prolate ellipsoid, characterized by a volume of $\frac{4}{3}\pi ab^2$, where a is the semi-major axis and b is the semi-minor axis. The deviation of the ellipsoid from a sphere of radius R is expressed in terms of a distortion parameter ϵ as follows:

$$a = R(1+\epsilon)$$
$$b = R(1+\epsilon)^{-\frac{1}{2}}$$

Here, ϵ represents the eccentricity of the ellipse and is associated with the deformation parameter β given by $\beta = \frac{4}{3}\sqrt{\frac{\pi}{5}}\frac{\Delta R}{R_{av}}$, leading to $\epsilon = \frac{\beta}{\sqrt{5\pi}}$. It is important to note that $R^3 = ab^2$, ensuring the volume remains constant while the distortion increases. As a sphere is elongated into an ellipsoid, its surface area expands according to

$$S = 4\pi R^2 \left(1 + \frac{2}{5}\epsilon^2 + \dots\right);$$

as a result, the surface energy term in the semi-empirical mass formula also increases. The Coulomb energy term is modified by the factor

$$\left(1 - \frac{1}{5}\epsilon^2 + \dots\right),$$

leading to the energy difference (specifically, the reduction in binding energy) between a spherical nucleus and an ellipsoid of the same volume, expressed as:

$$\Delta E = B(\epsilon) - B(\epsilon = 0)$$

$$\simeq -a_s A^{\frac{2}{3}}\left(1 + \frac{2}{5}\epsilon^2 + \dots\right) - a_c\frac{Z^2}{A^{\frac{1}{3}}}\left(1 - \frac{1}{5}\epsilon^2 + \dots\right) + a_s A^{2/3} + a_c\frac{Z^2}{A^{1/3}}.$$

$$\simeq \left(-\frac{2}{5}a_s A^{2/3} + \frac{1}{5}a_c\frac{Z^2}{A^{1/3}}\right)\epsilon^2 \tag{2.1}$$

If the second term surpasses the first, the energy difference becomes positive — indicating that energy is gained through the stretching process, with more significant stretching leading to even greater energy gain. This nucleus becomes unstable against stretching and is prone to fission. In Fig. 2.2 an illustration of the nuclear deformation stages during fission is shown.

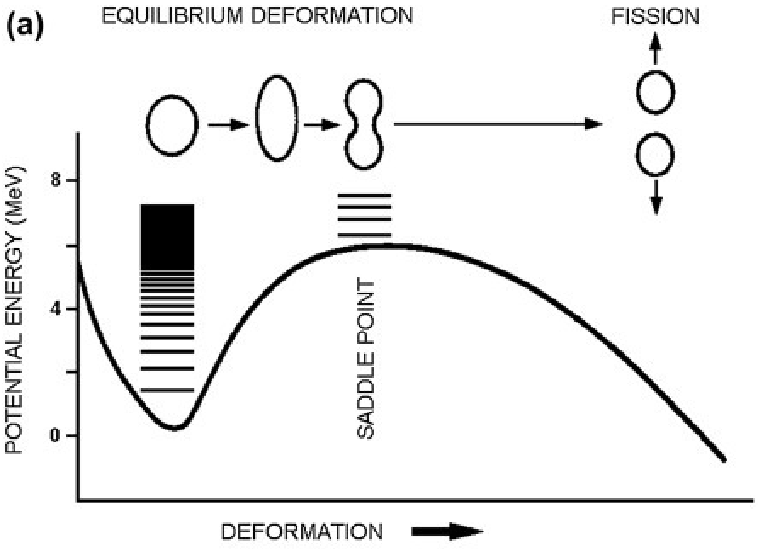

Figure 2.2: Representation of the evolution of the nuclear shape in fission as described by the LDM.

Consequently, for spontaneous fission, the condition is expressed as:

$$-2a_sA^{\frac{2}{3}} + a_c\frac{Z^2}{A^{\frac{1}{3}}} > 0.$$

By substituting the values of a_s and a_c, we arrive at:

$$\frac{Z^2}{A} > 47.$$

This simple estimation needs to be adjusted to consider quantum barrier penetration, which enables spontaneous fission even when the deformation energy is negative. It should also be introduced the observation made on the nuclei in the uranium region. Indeed, they have a permanent equilibrium deformation, resulting in an equilibrium shape that is ellipsoidal rather than spherical. Moreover, the observations listed in the next paragraph will let us understand that this simple model is not efficient to describe the fission reaction particularly in the actinide region.

2.3 Some Observations on Spontaneous Fission from the Liquid Drop Model

In this section are listed some experimental observations about fission that cannot be completely explained by the description of fission as a nuclear deformation in the framework of the liquid drop model.

2.3.1 Lifetime for Spontaneous Fission

The fissility parameter $\frac{Z^2}{A}$, defined earlier, can provide an approximate prediction of the nucleus's ability to undergo spontaneous fission. As shown in Fig. 2.3, the larger the parameter, the shorter the half-life for spontaneous fission (for the ground state). From the data reported in this graph, it is extrapolated that fission for nuclei $\frac{Z^2}{A} = 47$ would have a half-life of about 10^{-20} and hence the fission would "instantly" occur for nuclei having the Fissility parameter $\frac{Z^2}{A} > 47$.

This deduction, however, conflicts with experimental results from the period of 1960-63. During this period, at the Heavy Ion Laboratory in Dubna, through precise studies on various types of activity that could be linked to new heavy elements, spontaneous fission activity with a half-life of 14 ms was observed and attributed to ^{242}Am. This isotope has, in its ground state, a spontaneous fission half-life of the order of 10^{10} years. Therefore, it was impossible to understand how an excited state with a spontaneous fission half-life 10^{19} times shorter than that of the ground state could resist de-excitation for 14 ms [67]. The same uncertainty applies to other isomers, as can be observed in Fig. 2.3, here ^{242m}Am, ^{240m}Am and ^{236m}Am are shown having lifetimes shorter by many orders of magnitude compared to their ground state.

2.3.2 Mass Distribution of Fission Fragments

Another observation concerns the mass distribution products of a typical neutron induced fission reaction for compound nuclei of similar mass. This distribution is not symmetric for every compound nucleus, and while the mass distributions for heavy fragments overlap quite well, the lighter fragments exhibit significant variation (Fig. 2.4).

Comparing ^{236}U with ^{256}Fm, we note that Z, N, and A all increase by about 8.5%. If the liquid drop model of fission were a complete description of the process, we would expect both the heavy and light fragment mass distributions to shift by approximately 8.5% between ^{236}U and ^{256}Fm. That is, the mean fragment masses should shift from about 95 and 140 in ^{236}U to about 103 and 152 in ^{256}Fm. Instead, the observed mean masses in ^{256}Fm are about 114 and 141.

A second observation relates to the mean masses of light and heavy fragments for compound nuclei with masses ranging from $A = 228 - 256$. While the mass of the heavy fragment remains around 140, the light fragment takes up the remaining nucleons and increases linearly with A. This also contradicts the liquid drop model, where we would expect the fragment masses to scale with the mass of the drop.

Figure 2.4 highlights the regions where it is expected to find fission fragments with magic numbers for Z or N according to the shell model. This reveals that within the mass range shown in the figure, there is a region corresponding to the magic number $N = 50$ near the distribution of light nuclei and a second region around $A = 132$, where A corresponds to the sum of two magic numbers $Z = 50$ and $N = 82$ (or perhaps the closed deformed neutron shell at $N = 88$ [69]), making ^{132}Sn an extremely stable nucleus, which determines the lower limit of the heavy fragment mass distribution. No similar effect is observed for

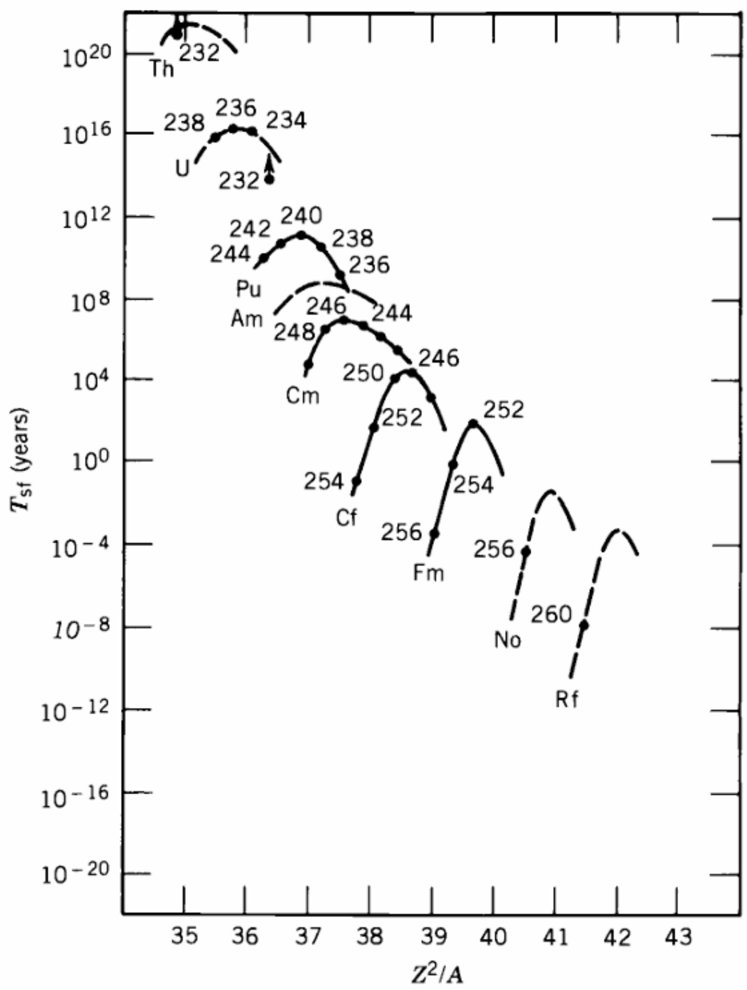

Figure 2.3: Measurements of lifetimes for the spontaneous fission nuclei as a function of the fissility parameter $\frac{Z^2}{A}$ in the mass range of actinides [66].

the light fragment, whose masses are far from the region of $N = 50$.

It appears that a fissioning nucleus tends to divide, forming a fragment around ^{132}Sn (the heavy fragment), while the remaining nucleons are distributed in the light fragment.

2.3.3 Resonance Structure

Another characteristic of spontaneous fission emerges when analyzing the cross section as a function of resonances. Figure 2.5 compares the fission cross section to the total neutron cross section for ^{240}Pu. It is clear that fission selects only certain resonances with a higher probability of fission, while other resonances decay through different processes, possibly via gamma or neutron emission.

Moreover, upon closer inspection, it is evident that fission resonances seem to cluster into well-separated groups rather than being randomly distributed. At the same time, the

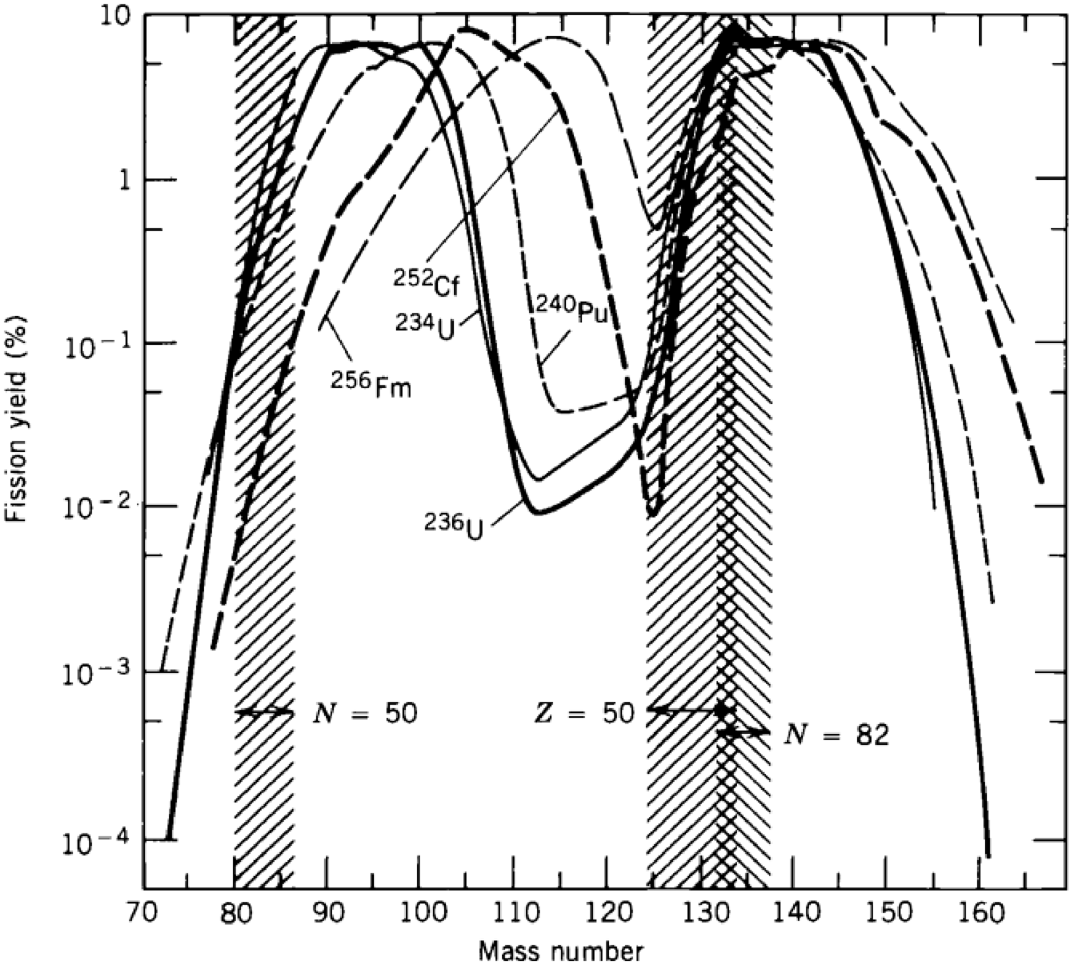

Figure 2.4: Mass distribution of fission fragments from thermal-neutron fission of ^{233}U, ^{235}U and ^{239}Pu, along with spontaneous fission of ^{252}Cf and ^{256}Fm. Shaded areas show approximate locations of closed-shell nuclei [68].

fission widths (between the resonances of the compound nucleus) are enormously large for some groups of resonances (100-1000 eV) and small (1-10 eV) for other groups ([70]). This phenomenon, known as the intermediate structure effect, has also been observed in other nuclei.

Further experimental campaigns revealed similar sub-threshold resonances in other non-fissile actinide isotopes, for instance, in ^{237}Np [63, 71, 72], ^{242}Pu [73, 74] and ^{234}U and ^{238}U [75].

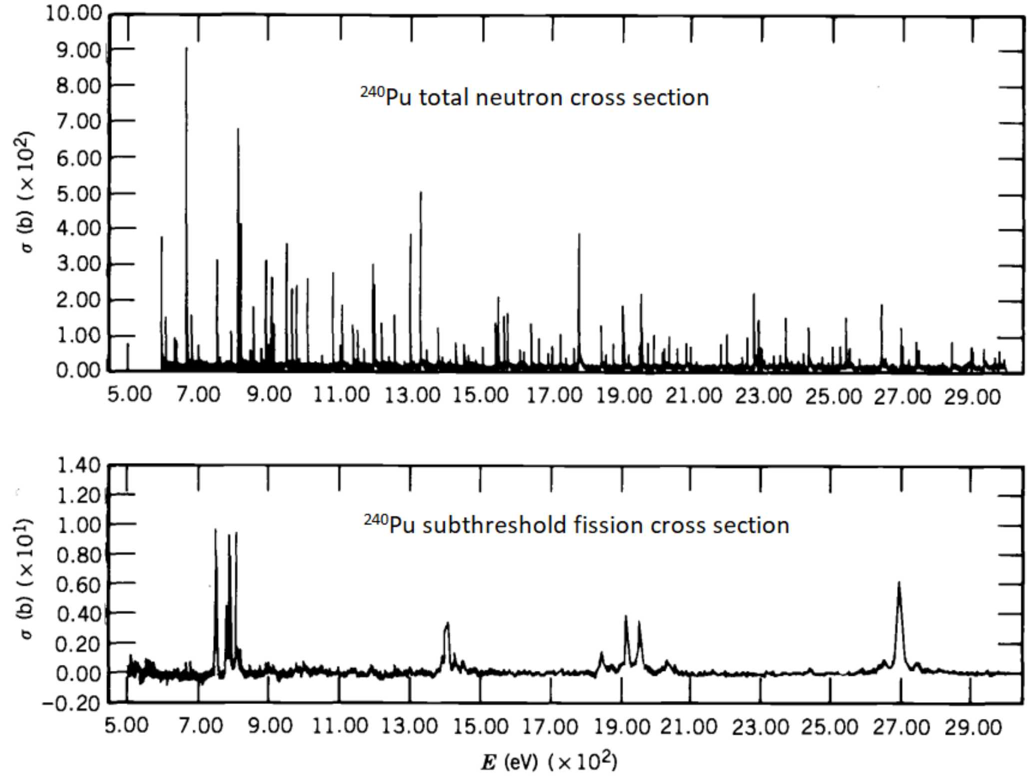

Figure 2.5: Comparison of fission and total cross sections of ^{240}Pu [68]. Upper plot in the picture shows the total neutron cross section as a function of the excitation energy of ^{240}Pu. Lower plot describes the fission cross section as a function of the excitation energy of ^{240}Pu. Fission selects only certain resonances with a higher probability of fission, while other resonances decay through different processes, possibly via gamma or neutron emission.

2.4 Introduction of Shell Effects to the LDM

"It was evident that there was a need for a unified theory that could provide balanced roles to both the LDM and the shell model" - Strutinsky[64, 68].

With these words, in 1966, Strutinsky made a breakthrough concerning the problem of incorporating shell effects into nuclear deformation energies higher than those of the liquid drop model (LDM). For this problem, he devised an averaging method, now known as the Strutinsky smoothing method or Shell Correction Model (SCM). At a 1969 symposium in Lysekil, Sweden, he presented the results of applying his shell-correction method to calculating fission barriers, providing a physical explanation for fission isomers — an experimental fact that had not yet been explained theoretically. Thanks to this method, the contradictory observations listed above finally found an explanation.

The Strutinsky method combines the macroscopic liquid drop model with a simplified microscopic treatment based on the shell model for nuclei in deformed potentials [76]. In the independent particle model, the total energy of a nucleus is given by the sum of single-particle energies. The SCM uses a renormalization of single-particle energies in deformed potentials relative to the liquid drop model energy, where the single-particle energy levels are replaced by a smooth distribution of states resembling the density of single-particle states but without the real shell structure [77].

We start by considering the energy levels for neutrons in a prolate deformation potential derived for the single-particle state in deformed nuclei by Nilsson [78] and observe the changes in the potential barrier description.

The most drastic effect of the shell structure occurs in the fission barrier itself. When we begin stretching the nucleus (characterized by an eccentricity parameter ϵ), the energy increases as ϵ^2, as shown in Eq. 2.1, giving an approximate parabolic dependence. The single-particle states in the now-deformed nucleus vary with deformation, as shown in Fig. 2.6; some increase in energy with deformation, while others decrease.

If the valence nucleons are in a state with a positive slope, the net energy increases with deformation and it will be slightly faster than the parabola since the single-particle energy also increases with ϵ. However, at some point, as ϵ increases in Fig. 2.6, the energy crosses into a state with a negative slope. The valence particle, choosing the lowest energy state, now follows the new state, and the net energy change with ϵ is slightly less than the parabola. This continues until another crossing occurs with a state where the energy increases with ϵ, and the total energy again exceeds the parabola. The energy function evolution of the valence particles as function of deformation ϵ is shown in Fig. 2.7. At the point where fission begins, the shape of the single fission barrier shown in black in Fig. 2.7 is modified, and the energy dependence introduced by the single-particle shell structure results in a double-humped fission barrier.

The figure represents in black (solid line) the potential energy as a function of the nuclear deformation once the shell contribution is added to the liquid drop model as described by Strutinsky. Unlike the liquid drop model alone (dashed black line), there are two local minima, with the first being deeper than the second, having an average difference of 2-3 MeV between the first and second minima. The lowest lying states in the first and second wells are called class I and class II states or ground state (GS) and superdeformed ground state (SD), respectively.

The appearance of a second minimum also explains the existence of shape isomers that undergo spontaneous but delayed fission, discovered several years ago [61]. These so-called shape isomers (metastable states) have their ground state in the second minimum. Shape isomers decay either by fission (if) or by an internal deexcitation, i.e., via gamma decay into the first well (iγ), corresponding to tunneling through the outer or inner barrier, respectively. This also explains the much shorter half-lives for spontaneous fission of isomers, hence called delayed or isomeric fission, compared to the ground state. In the second minimum configuration, the barrier to be crossed is much thinner.

The presence of a second minimum in the potential energy versus deformation can also explain the intermediate structure effect in fission resonances. As the deformation increases (in the second minimum, nuclei are more deformed than in the first), the rotational spectral bands become closer. Indeed, using the formula for the rotational spectrum $E = \frac{\hbar^2}{2I} l(l+1)$, where E is the energy of the considered band member state, I is the moment of inertia, and l is the angular momentum, and recalling that the moment of inertia is directly proportional to the deformation, we find that for more deformed configurations, the term inversely proportional to energy $\frac{\hbar^2}{2I}$ is smaller, and thus the distance between rotational energy states is smaller.

These so-called intermediate structures have been observed for many actinide nuclei, as summarized elsewhere by Bjørnholm and Lynn [62] or Weigmann [80] and references therein.

The Strutinsky method, with the introduction of the second minimum, also explained why shape isomers in actinides have different decay preferences. In this regard, Möller and Nix [81] presented barrier calculations for thorium, plutonium, californium, and nobelium with neutron numbers $N = 142, 146, 150, 154$, and 158, showing that the height of the inner barrier varies with proton number Z. In particular, light actinides predominantly decay via gamma decay, heavy ones favor delayed fission, while both decay modes are observed in the intermediate region for uranium and neptunium isotopes. Figure 2.8 illustrates how the height of the outer barrier changes with increasing Z for various actinides, from thorium to californium, showing that for larger Z, the outer barrier height is lower than the inner barrier, favoring delayed fission, while for smaller Z, the opposite is true, and for intermediate Z, where the barrier heights are similar, there is no preferred decay mode.

The island of shape isomers for the known actinides nuclei is represented in the Fig. 2.9. Here, the squares in yellow are the predicted and observed shape isomers. In the picture are included: the isomeric half-life, the existence of a third minimum (III, in red), the energy for the γ - back decay into the first minimum (in green) and the decay mode. The picture is adopted from [79] and modified accordingly to the new data from [83, 84, 85, 86] and from the National Nuclear Data Center (NNDC), maintained by the Brookhaven National Laboratory.

Despite the successful explanation of the experimental observations mentioned above, the early SCM calculations did not provide the correct fission barrier shape for actinides and failed to explain observed asymmetry in the mass distribution of most fission fragments.

In the meanwhile, again Möller and Nix [81], identified an unexpected phenomenon: the peak of the outer barrier was found to split into two distinct peaks, separated by a at that time assumed shallow third minimum for small neutron numbers $N \leq 146$. Additionally, when comparing these experimental results with calculations based on a two-humped model, it was observed that the calculated second minimum was several MeV lower than the experimentally deduced one. However, these analyses were carried out using a model that assumed a double-humped barrier, which later proved to be inadequate. The first direct evidence of a triple-humped barrier emerged from the analysis of microstructures in the resonances of the reactions $^{232}\mathrm{Th}(n,f)$ and $^{230}\mathrm{Th}(n,f)$ [87, 88]. This considerable mismatch, along with a similar issue concerning the inner barrier height, became known as the "thorium anomaly". Later on, the microstructures were interpreted as rotational bands, where the level spacing and the deduced moment of inertia, $\hbar^2/2I \approx 2$ keV, suggested a quadrupole deformation of $\beta_2 \approx 0.9$.

Subsequent experiments, using the reaction (d, pf) (e.g., [89]), transferring more angular momentum, verified the previous results and strongly supported the existence of a third minimum.

More than 10 years after the work of Möller and Nix, Bengtsson et al. [90] studied the potential energy landscape of thorium isotopes and other nearby nuclei, including deformations of all multipolarities up to six. They studied for the first time the influence of β_6 on the appearance of the third minimum and demonstrated that the position and height of the peaks and the third minimum as a function of β_2 change from $\beta_6 = 0$ to $\beta_6 \neq 0$. As a consequence, for elements up to uranium, it is expected that nuclei near the beta-stability line have a third minimum about 0.4 MeV deep, while for neutron-rich nuclei, the minimum was measured to be up to 1.5 MeV deep [90].

Building on this, here is reported an example of a PES study for ^{232}Th (in Figure 2.10) that includes multipolarities up to 7 [91] and helps to understand the observation of the asymmetric fission fragment distributions. Referring to Fig. 2.10, the potential energy landscape in the (β_2, β_3) plane, shown on the left side of Fig. 2.10, exhibits the super-deformed (SD) minimum at $\beta_2 = 0.6$ and $\beta_3 = 0$, while the hyper-deformed (HD) minimum splits into two distinct minima at $\beta_2 = 0.86$, but with very different values for β_3 ($\lambda = 3 - 7$). The corresponding values for $\beta_3 \approx 0.57$ and 0.34 can be directly determined from the contour plot; all other values for β_4 to β_7 can be found in the original work. The ground state minimum, which is not displayed, corresponds to a reflection symmetric shape with $\beta_2 \simeq 0.2$ and $\beta_4 \simeq 0.1$. The right side shows the deformation energy as a function of β_2 for the shortest of the two static fission paths, indicated by dashed lines on the left. The zero deformation energy refers to the spherical nucleus. The excitation energies of the second and third minima are indicated as $E_{II} = 2.1$ MeV and $E_{III} = 4.2$ MeV, respectively.

A more recent work that also shows the energy as a function of the deformation can be found in the habilitation thesis of P. Thirolf [92]. In Fig. 2.11, it is shown, again for ^{232}Th, the potential energy surface as a function of the deformation, calculated with different sets of relativistic mean-field parameters (PL-40: [93], NL1: [94], NL-SH: [95]). The barrier heights are also plotted as derived in these model calculation: in a non-relativistic Hartree-Fock calculation with the Gogny D1s force [96], in a macroscopic-microscopic calculation ('YE+WS': Yukawa-plus-exponential and Woods-Saxon) [91] and for the experimental dataset: exp^1 is taken from Ref. [62], exp^2 from Ref. [97] and exp^2 (O$^-$) from [98].

To re-connect to the fragment mass distribution, it is proposed here a very interesting observation, proposed by Cwiok et al. [91] and illustrated in Fig. 2.12. According to Cwiok et al., the structure of the third minimum in ^{232}Th arises from a di-nuclear-like configuration of the compound nucleus, in which a spherical and a deformed component coexist, forming two "solutions". The compound nucleus ^{232}Th can be seen as a system with a nearly spherical heavy fragment around ^{132}Sn and a well-deformed light fragment around ^{100}Zr as illustrated in Fig. 2.12.

To better understand what leads to the appearance of two solutions, we return to the observed fragment mass distributions. We observe that the compound nuclei for which fission fragments are reported can at most be composed of one doubly magic fragment plus a second fragment containing the remaining nucleons. It is as if the compound nucleus were preformed by two nuclei, which become the fission fragments once the nucleus undergoes fission. The two nuclei organize themselves so that one, or both if possible, tend toward the maximum stability predicted by the shell model. This shows how crucial Strutinsky's suggestion of adding shell effects to the LDM was. In this light, it becomes clear why we obtain the fragment mass distribution emerging from Fig. 2.12. For compound nuclei between ^{234}U and ^{256}Fm, a nucleus can pre-form ^{132}Sn, with the remaining nucleons arranging themselves in the second fragment. Up to here we have only shown asymmetric mass distributions. The occurrence of symmetric fission also tells us the importance of shell models driving the fragment formation. Indeed, approaching the mass of the compound nucleus ^{264}Rf, the fragment mass distribution is symmetric, since it is associated with the strong ^{132}Sn $+^{132}$Sn channel (see discussion in [99]) which for a compound nucleus with lower mass is not possible.

At the end of this section, only the double minimum in the HD region of the PES remains to be explained. The existence of split HD minima allows for multiple fission pathways — at different deformations, leading to different mass splits and average total kinetic energies. These so-called fission modes form the basis of the multimodal random neck rupture model (Brosa et al. [99, 100]) which is explained in the next section.

2.5 Multimodal Random Neck Rupture Model

The multimodal random neck rupture model [100] was first proposed by Turkevich and Niday in 1951 [101] to explain the mass distribution of fission fragments from the compound nucleus ^{233}Th.

According to the Brosa model, the compound nucleus is still regarded as a thermalized system, that is, a system which, between its formation and scission, passes through an intermediate equilibrium stage. However, its evolution takes place on a multidimensional potential energy surface.

This model combines the macroscopic dynamics of the Liquid Drop Model with microscopic corrections arising from shell effects. In this way, while the Shell Model provides a probabilistic interpretation of the decay channels, the Brosa model describes the compound nucleus as a system that evolves dynamically on a complex potential energy surface, whose minima correspond to energetically favored nuclear deformations along the fission path.

The minima of the potential energy function in the Brosa model correspond to the so-called fission valleys (fission channels), that is, the energetically preferred pathways the nucleus may follow towards scission. Each minimum represents a stable configuration of the compound nucleus, associated with a specific mass asymmetry of the final fragments and a distinct balance between macroscopic and microscopic contributions.

The"Brosa model" is divided into two main parts: the Random Neck Rupture Model and a second part (derived from the same model), which introduces the new concept of fission multichannel behavior.

The random neck rupture model describes the compound nucleus as a system that evolves randomly over time. A compound nucleus elongates (e.g. via a β-vibration along the long axis of the rotational ellipsoid) and deforms increasingly, creating a "neck" connecting the two primary lobes. This neck is very thin and fragile, and fluctuations in its structure lead to rupture. The way in which this neck breaks has a direct influence on the mass distribution of the produced fragments.

The model is called random neck rupture because it predicts that for the same compound nucleus, the evolution of its pre-scission shape can vary and occur stochastically. Thus, the "neck" may appear in different positions on the surface of the deformed nucleus.

The rupture may occur closer to one of the lobes, producing asymmetric fragments, or in a more balanced way, generating fragments of more similar masses. According to this model, several parameters of the fission process are closely related to the nature of the neck and its rupture. These parameters are:

- **Total Kinetic Energy (TKE)**: The energy released during the rupture of the neck is a critical factor. A shorter or thinner neck generally results in higher TKE, as the fragments are closer to each other when separating, thus experiencing a greater Coulomb repulsion force.

- **Fragment Mass Distribution (Y(A))**: The model explains why the mass distribution of fragments produced by fission is often asymmetric. When the rupture occurs near one of the lobes, the fragment produced in that region will be larger, while the other will be smaller. This generates a "two-humped" distribution, characteristic of low-energy fission, such as that of ^{235}U.

- **Neutron Multiplicity ($\nu(A)$)**: The number of neutrons emitted during fission is also influenced by the way the neck ruptures. A longer or more unstable neck is associated with higher neutron multiplicity, as hotter and less stable fragments tend to emit more neutrons.

Since the pre-scission shape follows a random evolution, it is possible to have different pre-scission configurations for the same nucleus. This suggests the existence of different fission channels, each associated with a pre-scission configuration. These fission channels are also referred to as "fission modes."

If we consider the Potential Energy Surface (PES), the fission channels can be represented as different trajectories of the fission process in the PES leading to distinct results in terms of fragment characteristics such as mass, kinetic energy, and neutron multiplicity. The scission point on the PES is also called the bifurcation point, suggesting the various paths the process can take.

These bifurcation points are critical for understanding why, depending on the initial conditions (such as the energy or angle of incidence of the neutron inducing fission), the same nucleus can produce fragments with very different characteristics. For example, in the case of ^{236}U fission, even minimal variations in the incident neutron energy can divert the fission process into a different channel, resulting in different mass and kinetic energy distributions for the fragments.

The minima of the PES correspond to different configurations of the compound nucleus and represent what, in a 2D plot of potential energy versus deformation, correspond to the GS, SD, and HD minima. Fig. 2.13 shows a 3D representation of the PES, both in the case where it contains only the macroscopic energy term (LDM) and in the case where the microscopic shell effects (SCM) are added. One can visually understand that, in the case of the liquid drop model, there is only a single minimum, leading to only one possible mass distribution. However, when shell effects are included, multiple possible mass distributions (defined here starting from the fission channels) can emerge.

So far, three main fission modes have been identified: standard asymmetric mode I (S1), standard asymmetric mode II (S2), and the symmetric superlong mode (SL). The names of the fission modes reflect the pre-scission shape of a compound nucleus before fissioning. A pre-fission shape is directly connected to the mass and TKE distribution (as can be seen in Fig. 2.14) this mean that these two observables are very important for studies about nuclear structure (and nuclear shape) of fissioning nuclei.

The model also includes shell effects. In fact, the model suggests that the preference for forming nuclei with magic numbers is not random but derives from the energetic structure of the nucleus, which guides fission toward configurations that minimize the system's energy. Thus, a privileged pre-scission configuration is one where the neck divides the nucleus into two lobes, with one or both containing a magic number of nucleons. This explains the presence in the Fig. 2.4 of one of the two fragments with a mass close to ^{132}Sn.

An important application of the multimodal model is the ability to calculate the probabilities of different fission channels. Each channel has a different likelihood of being followed, and this probability can be calculated based on the potential energy along each path. In other words, the model allows for estimating which pre-scission configuration will be more probable based on the initial conditions of the system.

In this chapter an introduction to the knowledge of fission isomers has been reported. As learned here, the theory of this field had no great news in the last 30 years. On the other hand, newly available technologies have appeared which can be applied to proceed with the exploration of this topic trying to fill the empty box of knowledge and expand it toward new horizons and applications. The next chapter will introduce the new technologies used for the investigations made within this work.

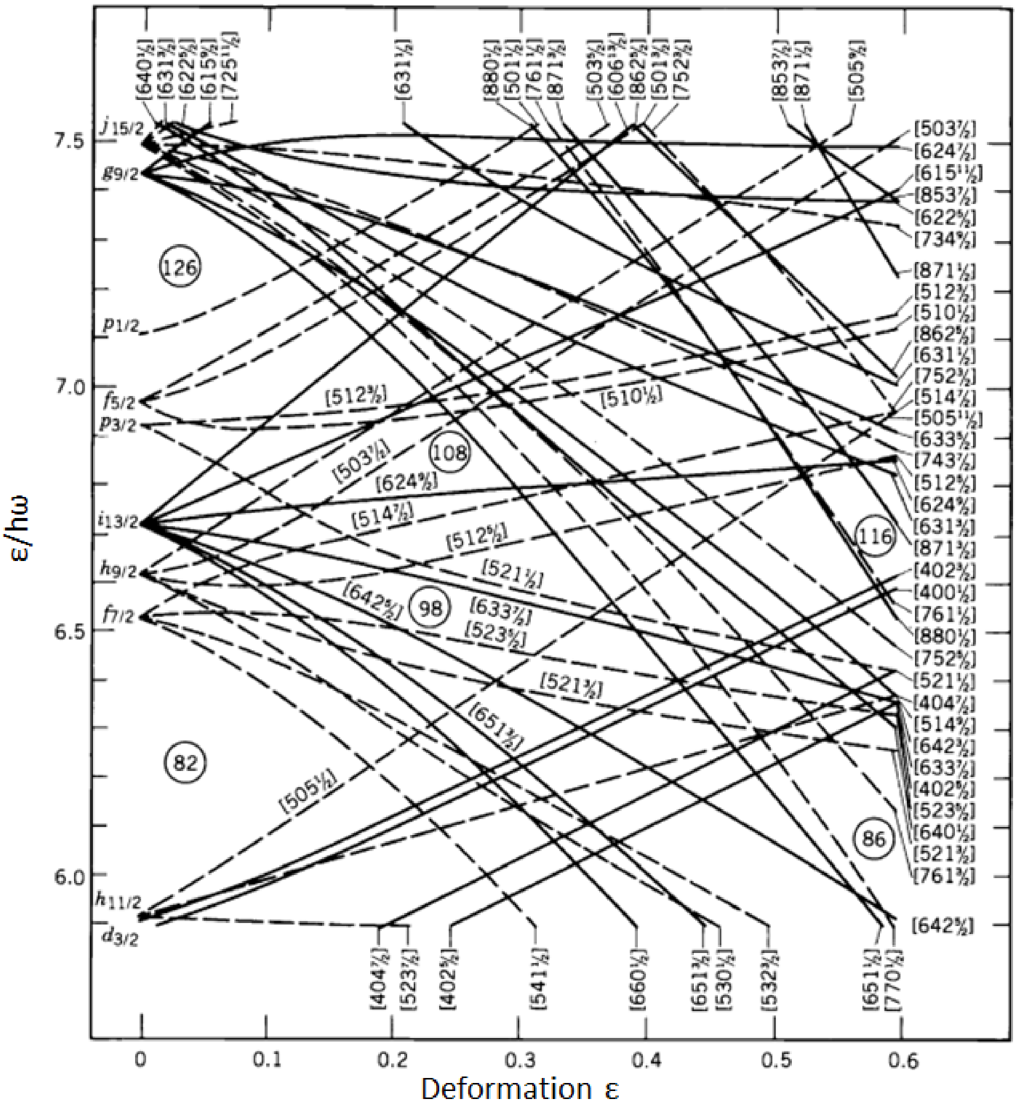

Figure 2.6: Energy levels for neutrons in a prolate deformed potential [78].

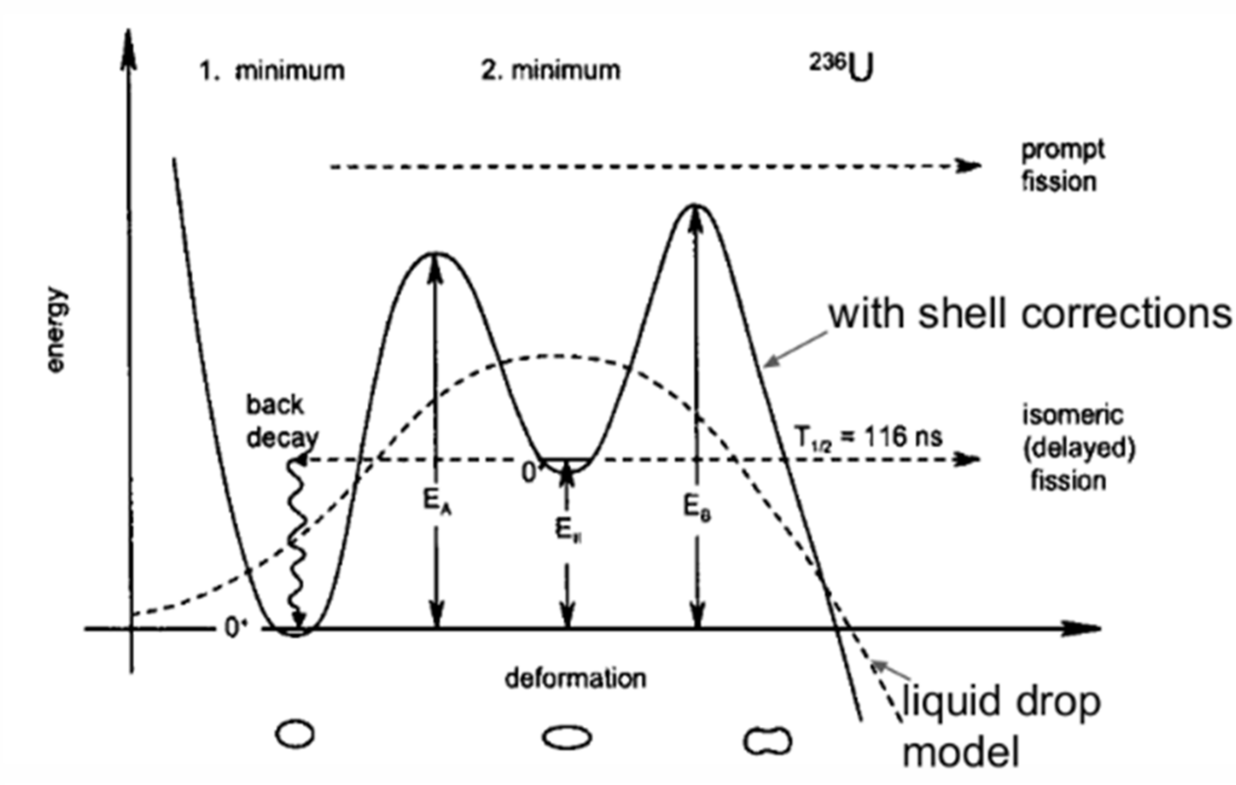

Figure 2.7: A schematic representation of fission isomers decay branches from the second nuclear potential well in the case of ^{236}U. A fission isomer can decay from the second potential well via two decay options: via isomeric (delayed fission) or via γ back decay into the first minimum [79].

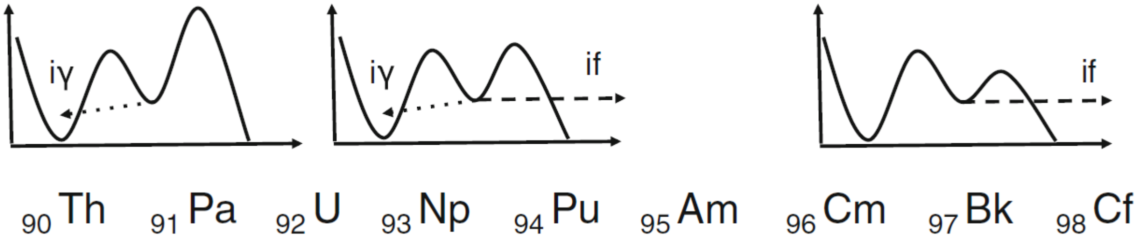

Figure 2.8: Trend of relative barrier heights for different actinides. The dashed and dotted arrows indicate a shape isomer's probability to undergo fission (if) and isomeric back-decay (iγ), respectively [82].

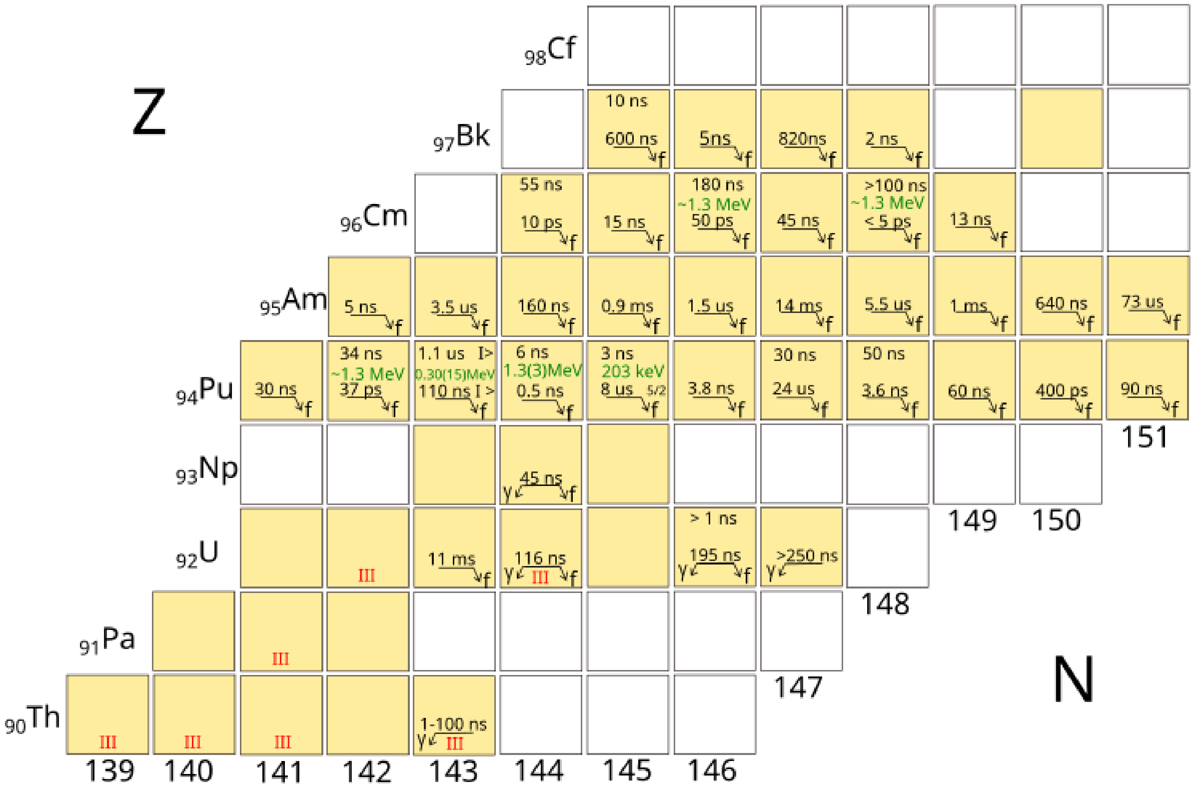

Figure 2.9: Part of the nuclear chart giving the half-lives of all fission isomers presently known. Two values for the same isotope indicate spin isomeric states in the second minimum. Isotopes where the existence of a third minimum in the potential energy surface has been experimentally established have been indicated by the index “III”.

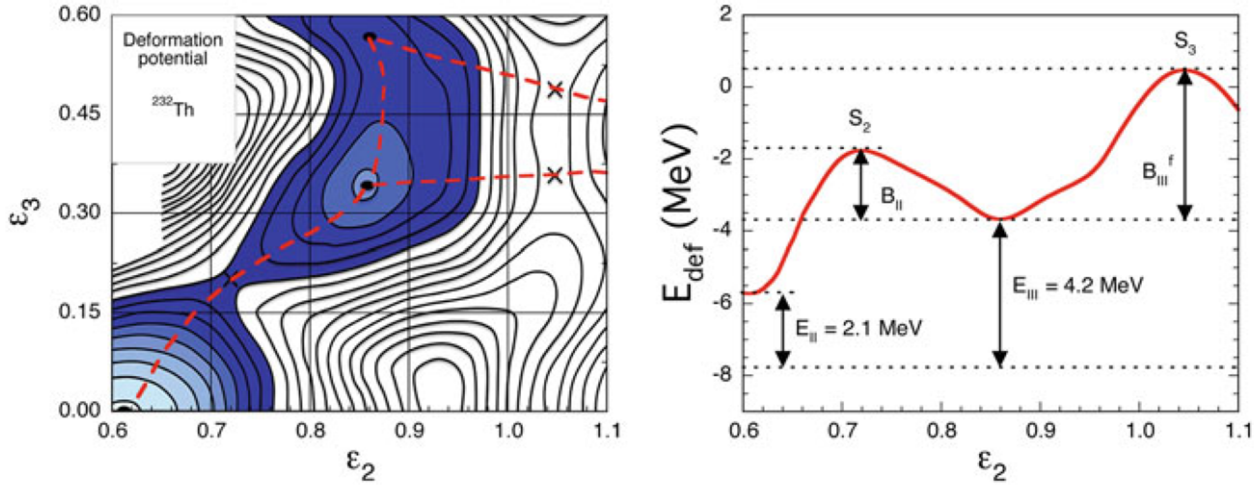

Figure 2.10: The left picture represents the potential-energy surface for ^{232}Th as a function of β_2 (quadrupole) and β_3 (octupole) deformations (here denoted as ϵ_2 and ϵ_3), according to [91]. The contour line separation is 0.5 MeV. The minima and saddle points are marked by dots and crosses, respectively. The dashed line indicates the static fission path from the second minimum to fission (via the reflection asymmetric third minimum at $\epsilon_2 \sim 0.9$, $\epsilon_3 \sim 0.3$). On the right side a plot of the potential energy as a function of the quadrupole deformation ϵ_2 is shown: the solid red line corresponds to the shorter trajectory in the contour plot from the left panel. The excitation energies of the minima are given relative to the ground state, and the heights of the second and third saddle point representing the barrier heights of the inner and outer barrier of the hyperdeformed third minimum are indicated, respectively, as S2 and S3 [91].

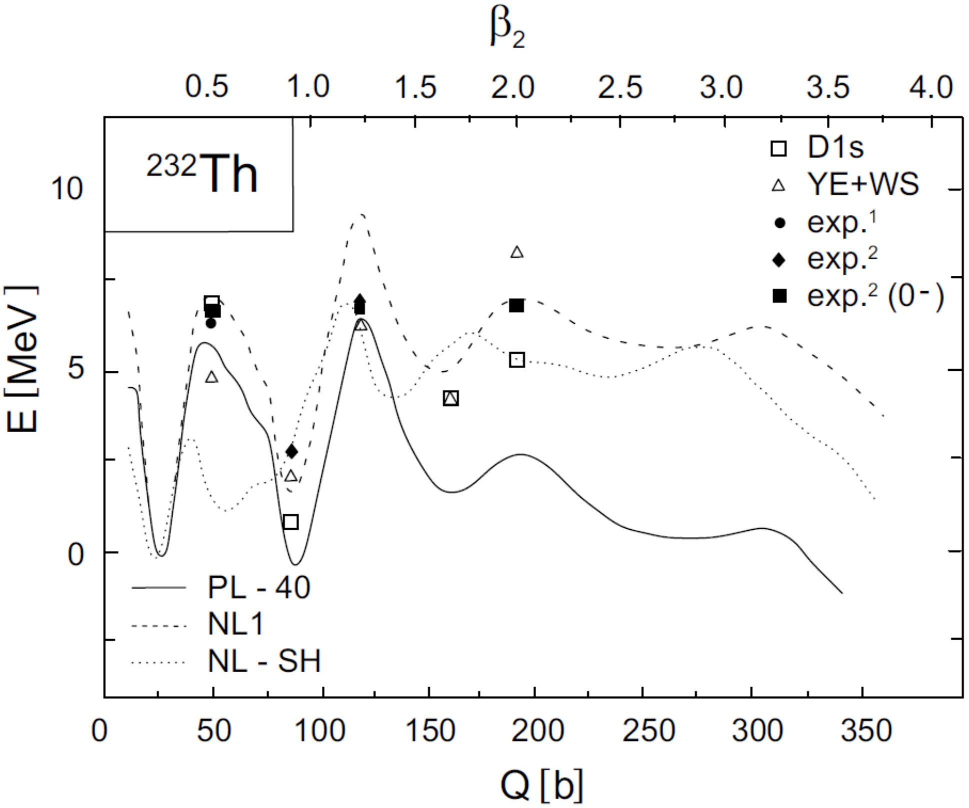

Figure 2.11: Potential energy surface of ^{232}Th calculated with different sets of relativistic mean-field parameters (PL-40: [93], NL1: [94], NL-SH: [95]). The barrier heights are also plotted: in a non-relativistic Hartree-Fock calculation with the Gogny D1s force [96], in a macroscopic-microscopic calculation ('YE+WS': Yukawa-plus-exponential and Woods-Saxon) [91] and experimental values are shown for comparison. exp^1 is taken from Ref. [62], exp^2 from Ref. [97] and exp^2 (O$^-$) from [98, 92].

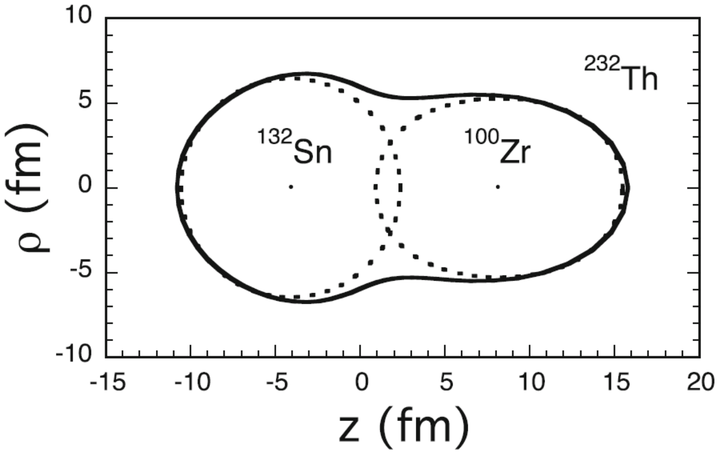

Figure 2.12: The shape of ^{232}Th in the (reflection-asymmetric, hyperdeformed) third minimum is shown as a di-nuclear system consisting of spherical ^{132}Sn and well-deformed ^{100}Zr [82].

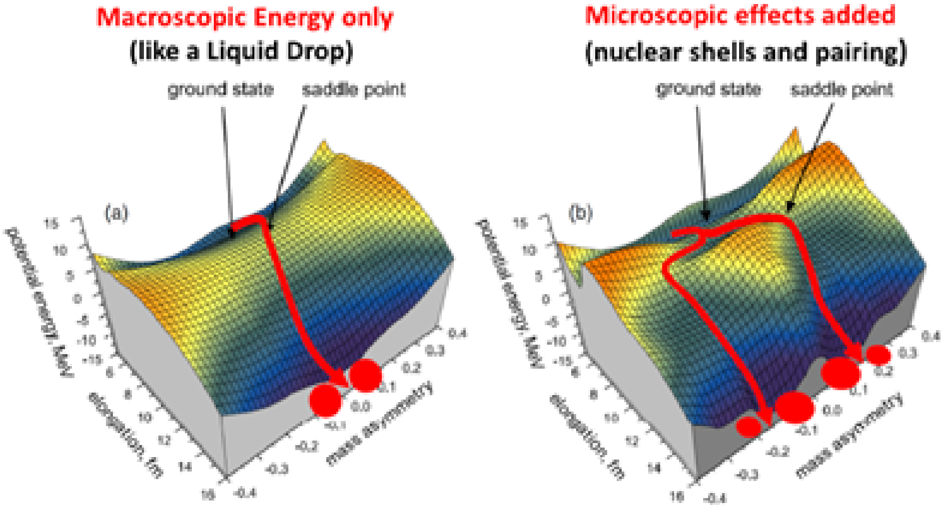

Figure 2.13: A 3D representation of the PES with only the macroscopic energy term (LDM, left panel) and with added microscopic shell effects (SM, right panel). In the LDM, a single minimum results in one possible mass distribution, whereas with shell effects, multiple mass distributions can arise from different fission channels [102].

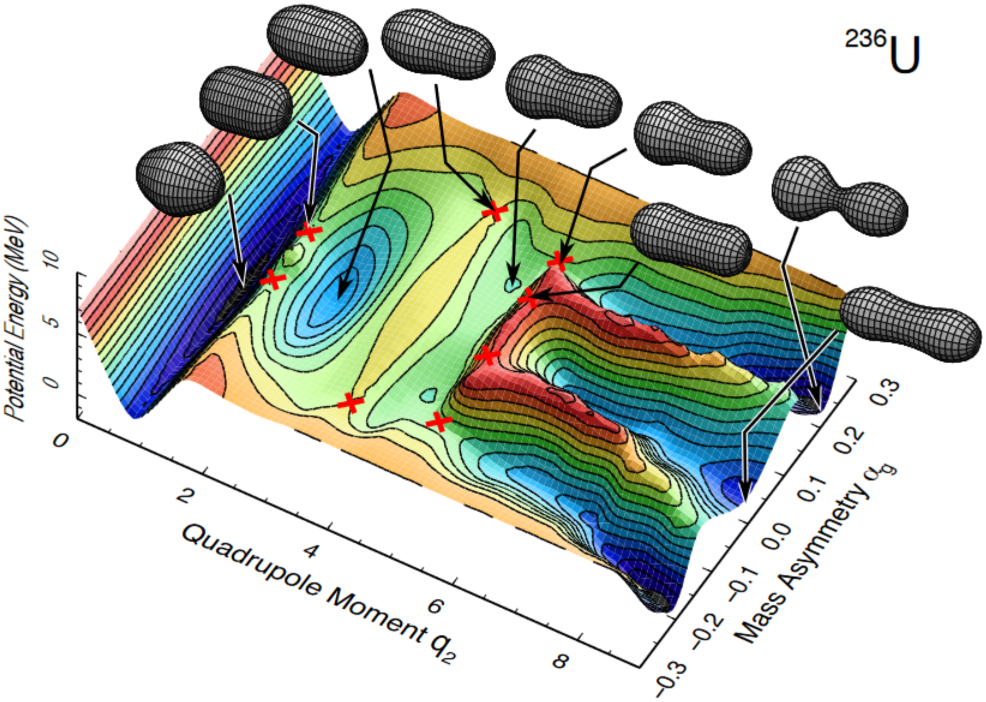

Figure 2.14: Potential energy surface of the compound nucleus ^{236}U as a function of the quadrupole moment and of the mass asymmetry. For each saddle point is indicated the nuclear shape of, accordingly to theoretical calculation, the nucleus ^{236}U. From the saddle point the fissioning nucleus can divide in fragments of a certain mass asymmetry [103].

Chapter 3

Introduction to the Fission Isomer Measurements at GSI and at IGISOL

In the context of studying the fission isomers discussed in the previous chapter, in this one are discussed two recent experiments conducted within the framework of this thesis at GSI and IGISOL. The two experiments employed significantly different techniques aimed at exploring specific regions of the actinide area, where, as discussed before, fission isomers are clustered.

Recent advancements in reaction mechanisms and experimental setups have opened new avenues for studying this topic, and we will summarize the techniques utilized in the two experimental campaigns.

3.1 Fission Isomer Experiment at the FRS

Historically, fission isomers in the actinide mass region were populated solely through direct reactions induced by light ions and neutrons. A recently intriguing method for producing actinide nuclei in isomeric states involves fragmentation reactions. This method, described in the previous Sect.1.2, consists of high-energy heavy ions striking a light-element target, allowing for larger excitation energies and spin transfers compared to the reactions induced by neutrons and light ions, which have predominantly been employed so far. Nuclear fragmentation also offers additional advantages, such as rapid production and separation (280 ns flight time for particles with 1 GeV/u from the production site to the end of the FRS), enabling access to isomers with short half-lives, and, most importantly, high beam purity and event-by-event identification. This method was utilized in the 2021 experimental campaign at GSI using the FRagment Separator (FRS). In this setup, a beam of ^{238}U at 1 GeV/u was directed onto a ^{9}Be target to produce fragments with $Z > 82$ and $140 < N < 146$. Two detection methods were employed, covering a half-life range from approximately 50 ns to 50 ms.

The first method, designed to address shorter half-lives (ranging from nanoseconds to microseconds), involves implanting reaction products into a fast plastic scintillator equipped with four photomultiplier tubes (PMTs), positioned at each of its four edges.

The system consists of three layers of plastic scintillator material, with thicknesses of 1 mm, 5 mm, and 1 mm, respectively. The first and third layers (named VETO 1 and VETO 2) are each coupled to 2 PMTs, while the middle layer (called the "implanter") is coupled to 4 PMTs.

Ions coming from the FRS reach the implantation system at a rate of approximately 1000 events per second. These ions are selected by the FRS with the same mass, ensuring that the time taken to travel between layers of the implantation system is consistent (on the order of tens of nanoseconds). When an ion passes through a layer of scintillator material, it emits a light signal, and the time of this signal is recorded.

Due to the relatively low rate of incoming ions, a single-event detection approach is feasible, with three possible scenarios:

- **An event signal is recorded in each detector.** The time interval between VETO 1 and the implanter, as well as between the implanter and VETO 2, is a few tens of nanoseconds. This indicates an ion passing through all three layers.
- **An event signal is recorded in VETO 1 and the implanter, but not in VETO 2.** This suggests the ion has been implanted in the second layer.
- **An event signal is recorded only in the second layer, with a possible time correlation to a previous implantation event.** In this case, the detected signal represents the decay of an ion that was implanted earlier.

For the study of fission isomers, only isomeric delayed fission decay signals are of interest. The system's resolution is insufficient to detect gamma back-decay signals.

A schematic picture of the implantation together with a VETO detector system photographs are shown in Fig. 3.1.

The decay events include beta and alpha decay and spontaneous fission, but fission events can be distinguished since they produce an energy deposit signals up to two orders of magnitude higher. Based on the discrimination the ratio of implantation to fission decay events can be calculated and it will provide the fission isomer-to-ground-state ratio.

The second method, which targets longer half-lives (approximately ms), utilizes mass spectrometry conducted with a multi-reflection time-of-flight mass spectrometer (MR-TOF-MS) [104] installed in the FRS-IC setup, which will be discussed in detail below. At the FRS-IC, positioned at the final focal plane of the FRS, ions are thermalized in high-density cryogenic helium gas, allowing for mass measurements using the MR-TOF. From the mass difference between ions in their ground and isomeric states, the excitation energy of the isomer, denoted as E_{II}, can be directly obtained when the data quality allows.

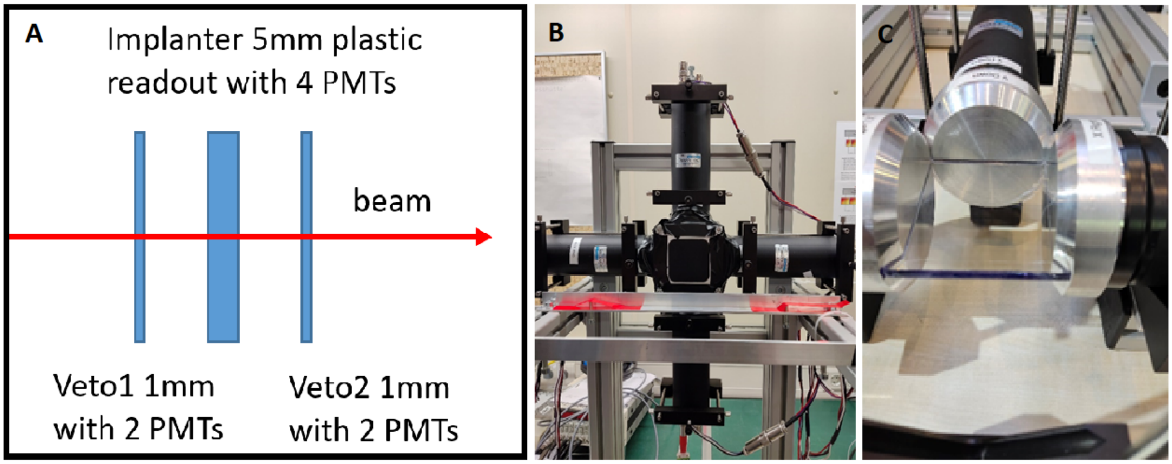

Figure 3.1: In A) a schematic representation is shown of the implantation system used during the experiment at GSI made of three plastic scintillator layers, where the middle one is called "implanter" and the other two called "VETO". B) displays a picture of the "implanter" plastic scintillator coupled to 4 photomultipliers at each of its sides, C) shows the bare system of the implanter and three of its four photomultipliers before light-tight wrapping of the scintillator sled.

3.2 FRS-IC technical description

As explained in the first chapter, the beam of reaction products produced by the fragmentation mechanism is then separated in-flight and delivered downstream to the FRS-IC. The FRS-IC is constituted of 3 main parts: a Cryogenic Stopping Cell (CSC) where the beam enters and is slowed down, a Radio-Frequency Quadrupole beamline (RFQ) that selects the beam constituents by their m/q ratio and guides the beam to a Multiple-Reflection Time-Of-Flight Mass Spectrometer (MR-TOF-MS). These components will now be introduced.

3.2.1 Cryogenic Stopping Cell (CSC)

The CSC accepts a beam of few MeV/u in ultra pure He gas at 70 K with an areal density of up to 9 mg/cm^2, resulting in a stopping efficiency of $15-20\%$ [105, 106], an extraction efficiency of circa 60% measured online [50], a mean extraction time of about 25 ms, and a rate capability of 10^4 ions/s [107]. In order to enable the experiment dedicated to fission isomers reported in this work, technical modifications had to be introduced to the system, improving both the extraction time and the rate capability. These two points are extensively described in this and the next sections.

The Cryogenic Stopping Cell (CSC) is constituted, starting from the outside towards the inside, by an insulation vacuum chamber at room temperature, an inner cold chamber operated at 70-80 K, the DC electrode cage and an RF carpet with a central hole towards an extraction RFQ. A sectional view of the stopping cell is shown in Fig. 3.2.

Both chambers are made of stainless steel. The insulation chamber has an entrance flange with a diameter of 69.5 cm and a thickness of 2.4 cm and a rectangular window of width 25 cm and height 10 cm and thickness of 100 μm.

The cold chamber in Fig. 3.3, is situated inside the insulation vacuum chamber. Between the two chambers there is an insulation vacuum at circa 10^{-5} mbars. The length, diameter and wall thickness of the inner chamber are 120 cm, 45.6 cm, and 0.3 cm, respectively.

To achieve cryogenic conditions (around 70 K) within the cold chamber, a cooling system has been designed using a network of helium gas pipes. Two lines filled with 6.0 He gas pass through a co-axial heat exchanger, the first one, called buffer line, then fills the cold chamber, the second one called cooling line, goes into a cryocooler system. This is made of a compressor where the gas is compressed and guided into, first, a LN2 pre -cooler device (or a faster cooling), and then, into a cryocooler system at circa 40 K where the gas is further cooled down up to 70 K and is circulated by a cryofan. After the cryofan the cooling gas line goes around the cold chamber to provide the cooling of the cold chamber. To keep the external surface of the cold chamber stable at the same (cold) temperature, the pipe is welded in a helicoidal structure around the cold chamber that makes the pipe to recirculate the He back into the cryocooler system.

The entrance flange of the inner chamber has a diameter of 42 cm and a thickness of 2.8 cm. Similar to the entrance flange of the outer vacuum chamber, this flange has a Ti

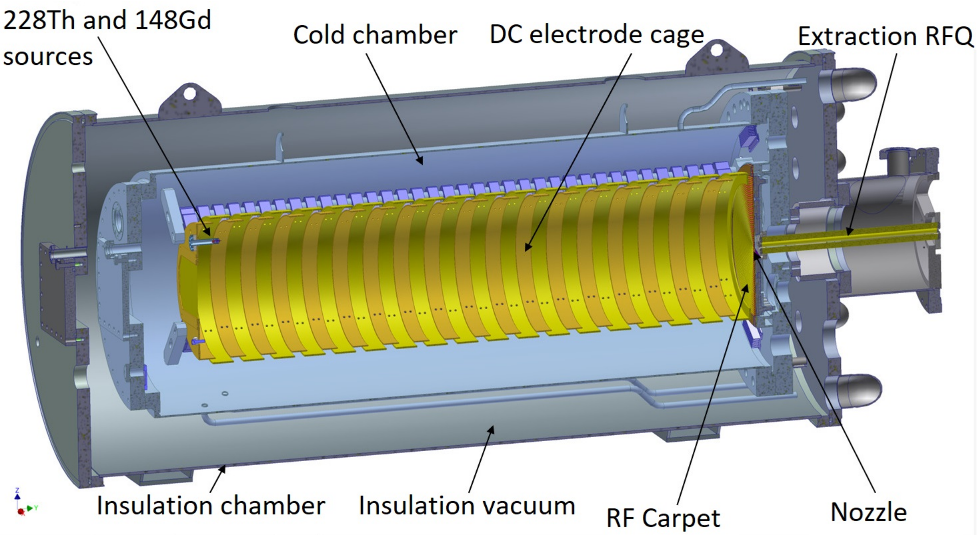

Figure 3.2: CSC in sectional view. The Cryogenic Stopping Cell (CSC) is a cylindrical stainless steel structure with a length of 120 cm and a diameter of circa 50 cm. It is constituted, starting from the outside towards the inside, by an insulation vacuum chamber at room temperature, a cold chamber at 70-80 K, the DC electrode cage and an RF carpet with a central hole towards an extraction RFQ.

rectangular beam inlet window of 25 × 10 cm^2 in the center and 100 μm thickness.

Inside the cold chamber is the DC electrode cage. The DC cage (so called "short DC cage" because in previous experiments at this facility a DC cage with double the length has been used) is a cylindrical structure (Fig. 3.4) consisting, in the case of the experiment concerning this work, of 27 ring electrodes with a pitch of 2 cm, with a length of 48.2 cm and an inner diameter of 26.7 cm.

On the surface of the DC cage first electrode (beam side) there is a metallic plate that can be the IN Cell Reaction System (INCREASE) [108] or a simpler metallic plate (this one was used during the beam time of this work). The last one has, in its central part, a degrader (a Ti foil serving also as energy degrader for the impinging energetic reaction products) and can host a maximum of three radioactive sources installed each in one source holder. For the S530 experiment only two source holders were installed to allow for a positioning of radioactive sources inside the DC cage's first electrode plate. The arrangement of the three sources: ^{252}Cf on the right side of the picture, ^{228}Th and ^{148}Gd on the left is illustrated in Fig. 3.5. In this picture the source holders of ^{228}Th and ^{148}Gd are closed to shield the radiation coming from them while working on the removal of the ^{252}Cf source that was not used for the experiment related to this work.

With the goal in mind of maximizing the extraction efficiency of radioactive source products we minimized the source offsets from the beam axis (81.6 mm) and made sure that the surface of the source holder, on the side where the source sits, is at the same height of the edge of the DC cage cover plate. The radioactive sources are used as calibrants for the beam line and for offline tests. The beam entering the CSC through a Ti entrance

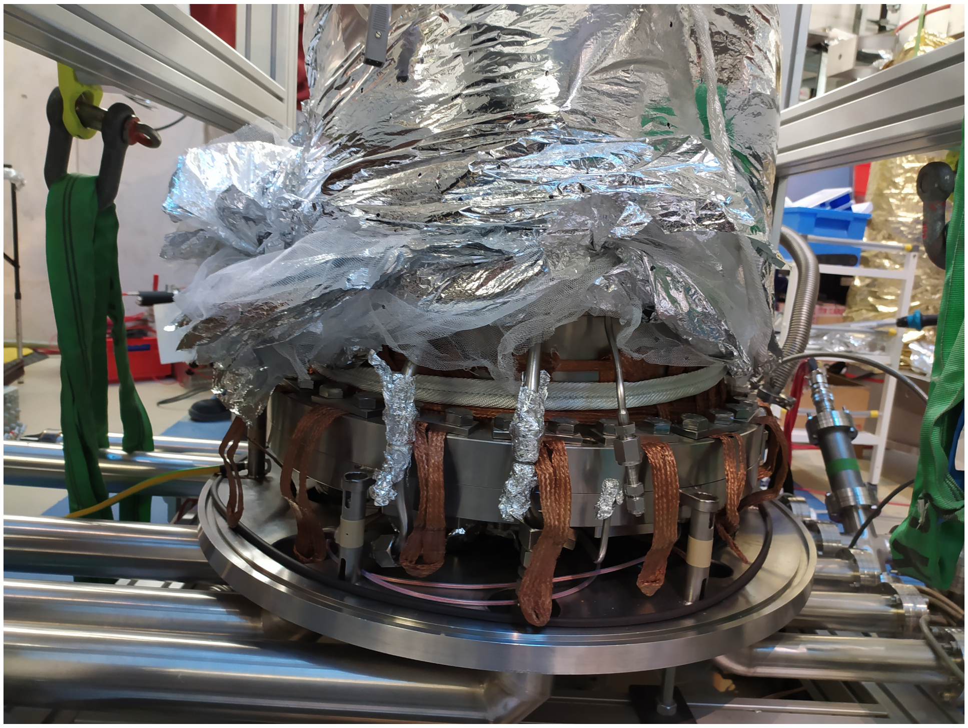

Figure 3.3: A view of the cold chamber around the sealing region in the bottom part. The small pipes are the cooling He inlet, the cooling He outlet and the He buffer gas inlet of the cooling system providing a temperature of 70-80K inside the cold chamber.

Figure 3.4: The "short" DC cage shown in this picture is a cylindrical electrode structure consisting of 27 rings with a length of 48.2 cm and a diameter of 26.7 cm.

Figure 3.5: The first ring of the DC cage is a metallic place installed at the entrance side on top of the DC cage is made up of 3 sections to place the source holders and in the central part a window made up of a degrader (a Ti foil of 30 μm thickness). The source holders on the left have ^{228}Th and ^{148}Gd radioactive sources installed, in the source holder on the right ^{252}Cf source is installed.

window, crosses the degrader Ti foil to enter the DC cage. The DC cage has the purpose to create a gradient DC electric field applying a certain potential to the first ring (1-2 kV are applied to the first electrode) and to the last electrode (50 to 100 V, accordingly to the necessity). The potential scales from the first to the last electrode using a resistor chain installed all along the length of the DC cage. To let the ions traverse the CSC, they are then focused on an extraction nozzle of a 0.6 mm diameter. For this purpose, on the downstream end of the DC cage a PCB - based radio-frequency carpet (RF-carpet) is installed, as visible in Fig. 3.6.

The RF carpet is a PCB disk with a diameter of 25 cm and 1.3 mm thickness, and has a 5-layer design as schematically indicated in Fig. 3.7 [109].

- The first layer contains 500 concentric ring electrodes with a density of 4 electrodes/mm which generate the repulsive RF field that prevents the ions from hitting the electrodes. On top of the RF repulsive field, a superimposed DC electric field, from the most peripheral ring to the most internal, transports the ions to the center of the RF carpet.
- The second layer, so called first inner layer, is segmented into 10 electrodes of circular shape (circa 12 mm wide each). It is used for the reduction of push field penetration through the carpet that could hit the last layer where electric components are installed. A second purpose is to allow the RF carpet to be operated at any offset potential. It is relevant when the DC electrode cage is operated at high push field and the pressure in the CSC is low. In this case the ions flies very close to the carpet and to the space around the nozzle such that an ions could pile up providing a nozzle blocking.
- Third layer called second inner layer, is a ground protection.
- The fourth layer has electrical components such as connectors and resistors to apply RF and DC field to the carpet.
- The last layer extends not across the full carpet size, it shields the extraction nozzle from electronics and protects it from possible electrical discharges.

Between each conductive layer there is an insulation layer to protect the different electrical layers from touching each other. The extraction nozzle is positioned in the center of the RF carpet, it has a copper cylindrical shape and a diameter of 0.6 mm that goes all through the carpet thickness. The RF carpet repels and guides the ions towards the extraction nozzle with a combination of a repelling RF field and a radial DC focus electric fields. This part of the CSC, as well as the electric fields in the vicinity of the RF carpet, are shown schematically in Fig. 3.8.

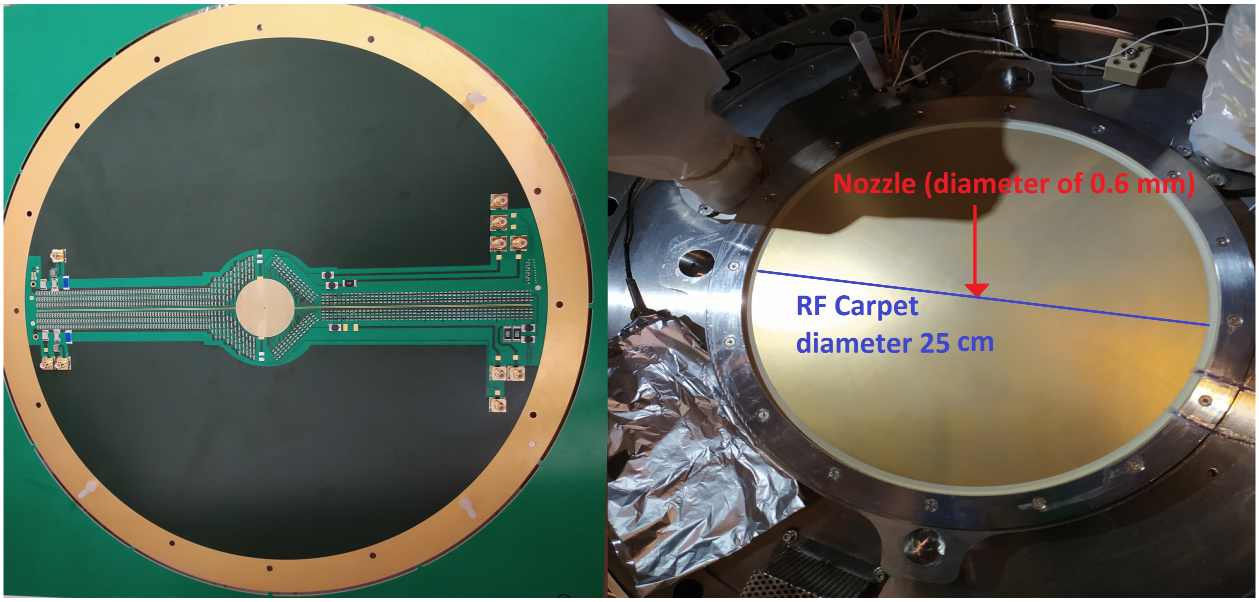

Figure 3.6: PCB- based Radio-Frequency carpet (RF-carpet). The RF carpet repels and guides the ions towards the extraction nozzle with a combination of RF and a radial DC electric fields [109]. On the left is the back side of the carpet, on the right is the carpet's front side.

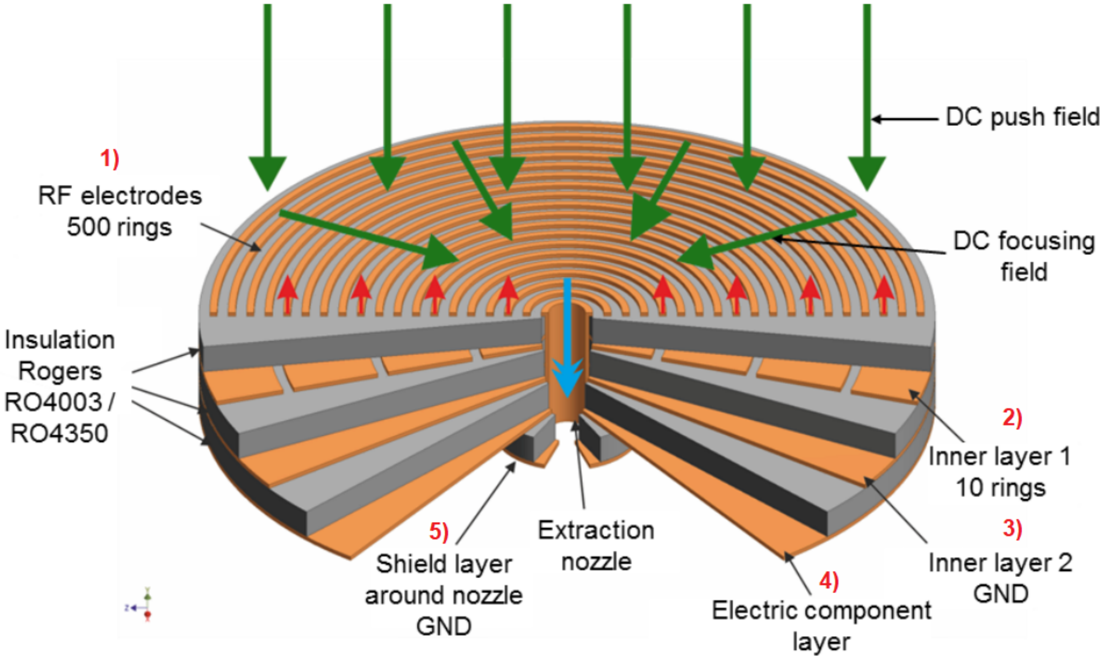

Figure 3.7: The RF carpet consists of a disk shape with a diameter of 25 cm, a thickness of 1.3 mm, and has a 5-layer design. The first layer contains 500 concentric ring electrodes with a density of 4 electrodes/mm. It generates a repulsive RF field that keeps ions away from the electrodes and the superimposed DC field guides ions towards the center. The second layer (Inner Layer 1) is composed of 10 segmented electrodes of circular shape (each about 12 mm wide). It minimizes push field penetration through the carpet thickness. The third layer (Inner Layer 2) acts as ground protection. The fourth layer houses electrical components like connectors and resistors needed to apply RF and DC fields to the carpet. The fifth (last) layer shields the extraction nozzle from electronics and protects it from possible electrical discharges. The extraction nozzle is positioned in the center of the RF carpet, it has a cylindrical shape and a diameter of 0.6 mm [109].

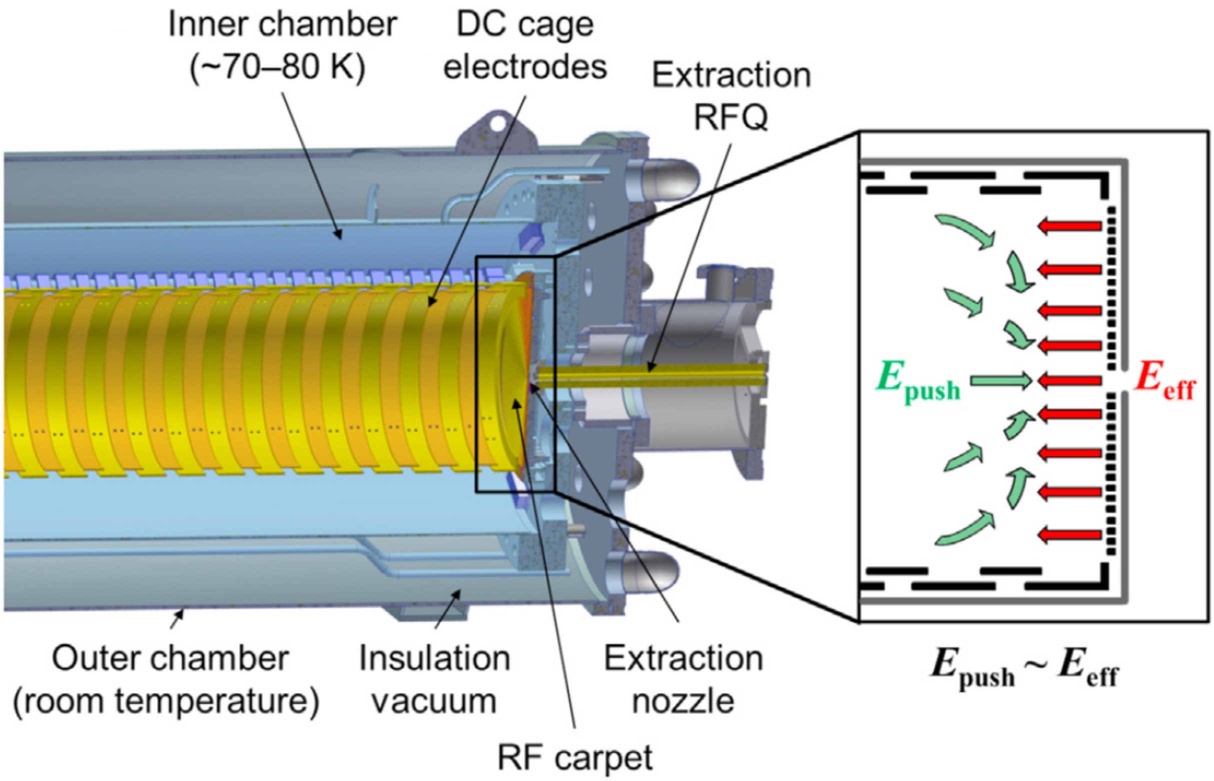

Figure 3.8: Scheme of the electric fields in the vicinity of the RF carpet.

3.2.2 Radio-frequency quadrupole beamline

The ions that reach the nozzle are extracted from the stopping cell by the dragging force of the supersonic gasjet forming in the vicinity of the nozzle. Subsequently, they may be pre-filtered for a certain mass-over-charge ratio of interest via the extraction RF quadrupole (RFQ) operated as quadrupole mass filter (QMF) that directly follows downstream of the extraction nozzle [110]. The RFQ is a multi-purpose ion-guide system, where ions are separated from the buffer gas jet, get phase-space cooled and bunched [111, 112]. The ions then enter a low-energy (∼eV) RFQ beamline which also provides first diagnostics and calibration tools. It also guides the transport of the ions, and induces isolation and dissociation of molecules attached to ions of interest or of undesired molecules with same m/q ratio of our ions of interest [113]. Furthermore, it is suitable as cooling and trapping system. This section will be from here on referred to as the DISTRICT module (DISTRICT, Diagnostics, Ion Sources, Transport, Isolation, Cooling and Trapping module). For the diagnostic and calibration, it is installed at DISTRICT a remote-controlled linear translation stage. It is equipped with a channeltron detector (Photonis 5901 Magnum Electron Multiplier) [114], two silicon surface barrier detectors (Ortec Ultra BU-016-150-100 bakeable) [115], an RFQ segment and a ^{133}Cs source and a three-line alpha source (a mixture of alpha-decaying ^{239}Pu, ^{241}Am, and ^{244}Cm isotopes). The detectors are suited to determine information on the beam extracted by the CSC. The ions in the beam can either be identified and quantified by their alpha-decay energy and half-life or transmitted downstream to the multiple-reflection time of flight mass spectrometer (MR-TOF-MS) within a flight time of circa 20 milliseconds. The calibrant sources allow the calibration of detector positions with respect to the beam direction and the alignment of the beam in the beamline towards the MR-TOF to minimize both beam lost and the time for the beam to reach the detector.

Furthermore, the RFQ beamline provides an additional differential pumping stage between the CSC and the MR-TOF-MS. This allows the MR-TOF-MS to operate at the top at circa $10E-6$ mbar while at the bottom at circa $10E-8$ mbar and the CSC operates at its highest areal density.

3.2.3 Multiple-reflection time-of-flight mass spectrometer

The RFQ beamline is followed by the MR-TOF-MS. The MR-TOF-MS itself is a powerful and universal mass spectrometer with single-ion sensitivity, a mass resolving power (FWHM) as high as up to 10^6 and a mass accuracy in the low 10^{-8} range [116]. In the upper part of the MR-TOF-MS in Fig. 4.11, the injection trap, the ions are accumulated, cooled by collisions with helium buffer gas in the trap system, and bunched. The bunched ions are injected into a time-of-flight (TOF) analyzer. The analyzer consists of a field-free drift tube and two reflecting electrostatic mirrors on both ends. In the center of the analyzer, the mass-range selector (MRS) is installed. This is a quadrupolar deflector, which can be pulsed in order to deflect the unwanted ions and thus purify the measured spectra. In the analyzer, the ions propagate for a certain number of turns (1 turn corresponds to the trajectory in the analyzer from the first mirror to the second one and back to the first mirror) until they exit the analyzer. After a selectable number of turns in the analyzer, the ions move towards a movable sled. Given the position of the sled in front of the MR-TOF exit, the ions can impinge on a certain time-of-flight detector for mass measurements. By the time of the present experiment three detectors were installed at the movable sled at the end of the MR-TOF. These are: an isochronous secondary electron multiplier (ETP MagneTOF) detector [117], the α-TOF detector [118], a silicon surface barrier detector. The α-TOF detector was installed for the first time for a beam time during the commissioning of the experiment S530 as is depicted in Fig. 3.9.

A Bradbury-Nielsen gate (BNG) [119] installed upstream the detectors enables additional post-analyzer TOF separation. The Bradbury–Nielsen Gate (BNG) is a thin grid used for mass-selective ion transport. When pulsed, it deflects unwanted ions and lets only the selected species pass to the detector. This allows clean decay spectra or measurements for short-lived isotopes that would otherwise be obscured by other species.

The MR-TOF-MS can be operated in several modes which are illustrated in Fig. 3.10:

1. **Time-focus shift (TFS) mode.** In this mode, all ions contained in the bunch that is released from the trap system are accelerated to the detector and get detected at the same time. This mode is also called the “pass-through” - mode, because the ions are basically passing through the tracking system without any interactions. With this the masses of the isobars impinging on the detector can be measured, the resolution, however, is not very high (mass resolving power of ~ 2000).

2. **High-resolution mass measurement mode.** The ions undergo multiple reflections in the TOF analyzer, resulting in a slight change of the path for different isobars. This leads to the isobars hitting the detector at the same, but at different points, allowing their masses to be separated more precisely and to improve the resolution of the mass spectra. A mass resolving power of $\sim 10^6$ was demonstrated in [120, 116].

3. **Isobar or isomer separation mode.** After a sufficient separation has been achieved in the TOF analyzer, extracted ions pass through the Bradbury– Nielsen gate (BNG) which selectively transmits an isobar or an isomeric state of interest, while suppressing the others.

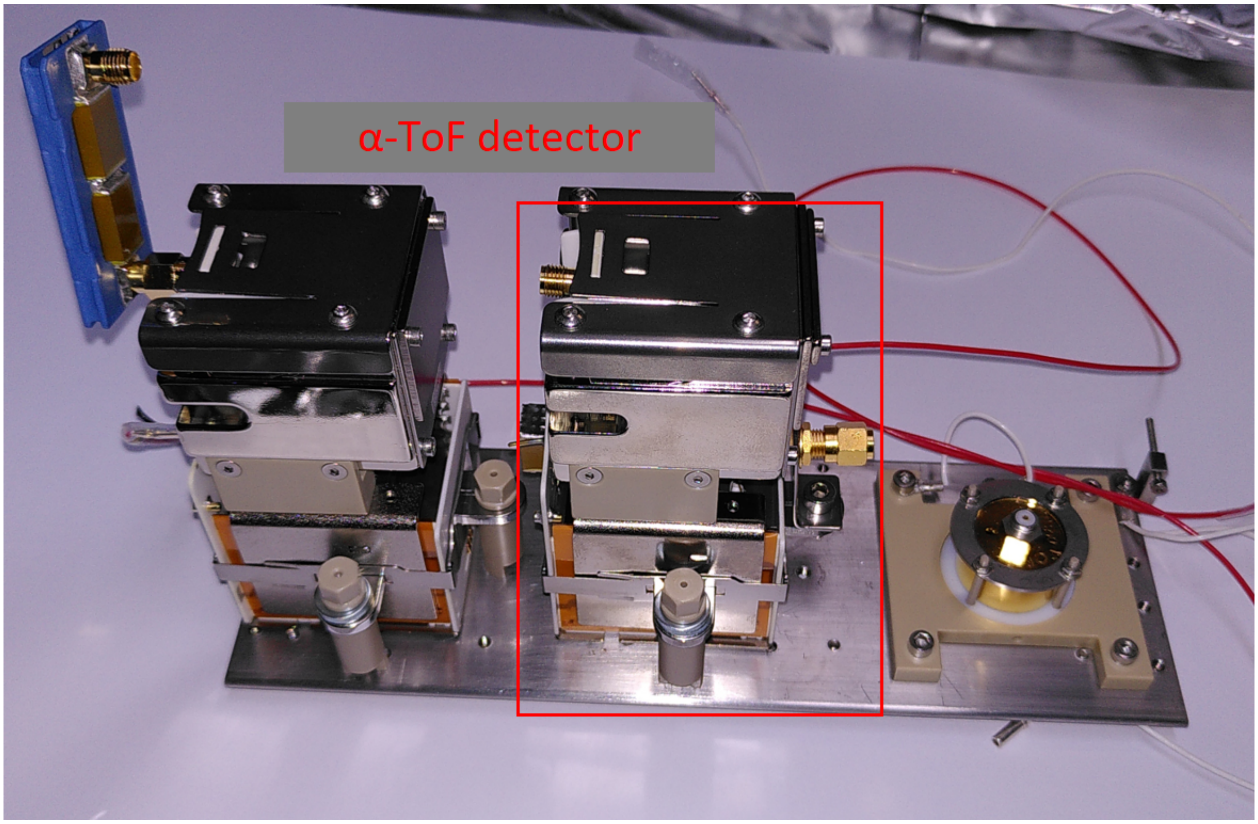

Figure 3.9: Photograph of the $\alpha-$TOF detector (highlighted by the red rectangular frame) attached to the MR-TOF detector section mounted to a movable sled. To the left of the $\alpha-$TOF detector is installed an ETP MagneTOF detector (installed for everyday use), to the right a silicon surface barrier detector.

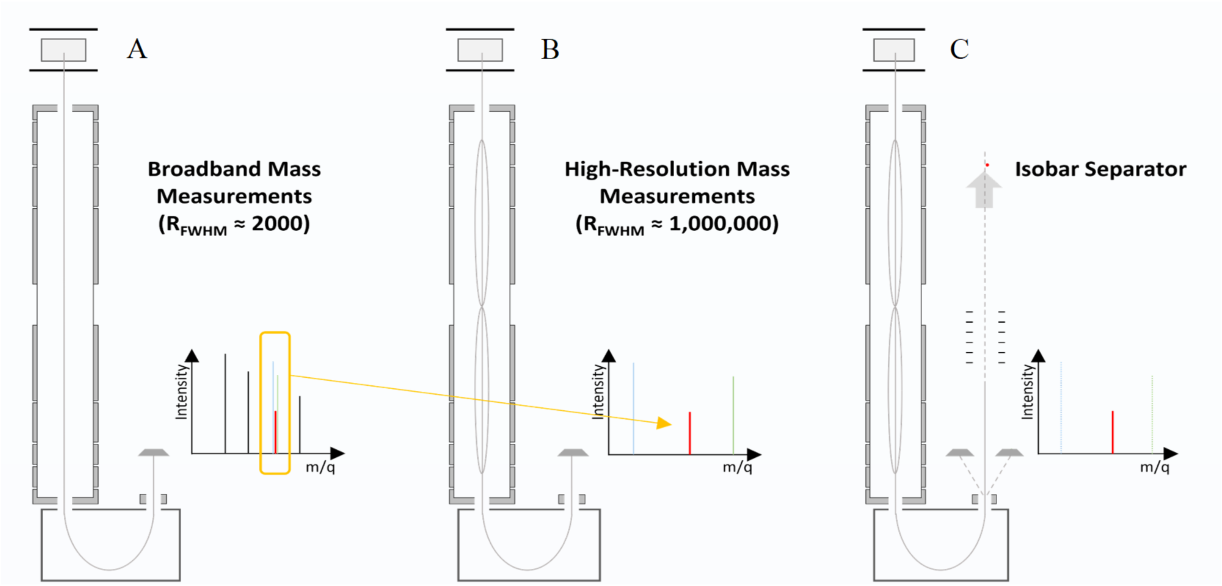

Figure 3.10: Schematical illustration of the MR-TOF operation modes. A) Diagnostics mode (Full mass range, mass resolving power (FWHM) ~ 2000), B) High resolution mass measurement of (short-lived) nuclei (mass range = 1 u, mass resolving power up to mass 10^6, accuracy $10^{-6} - 10^{-7}$), C) Isobar or isomer separation mode for experiments with exotic nuclei in the presence of strong isobaric contamination. . Unpublished internal presentation by Jiajun Yu, 2022

The α-TOF detector

The $\alpha-$TOF detector [118] is a commercial MagneToF detector (ETP $14DM572$) [121], modified by replacing the central portion of the impact plate with a silicon surface barrier detector (SSD, Hamamatsu S-3590).

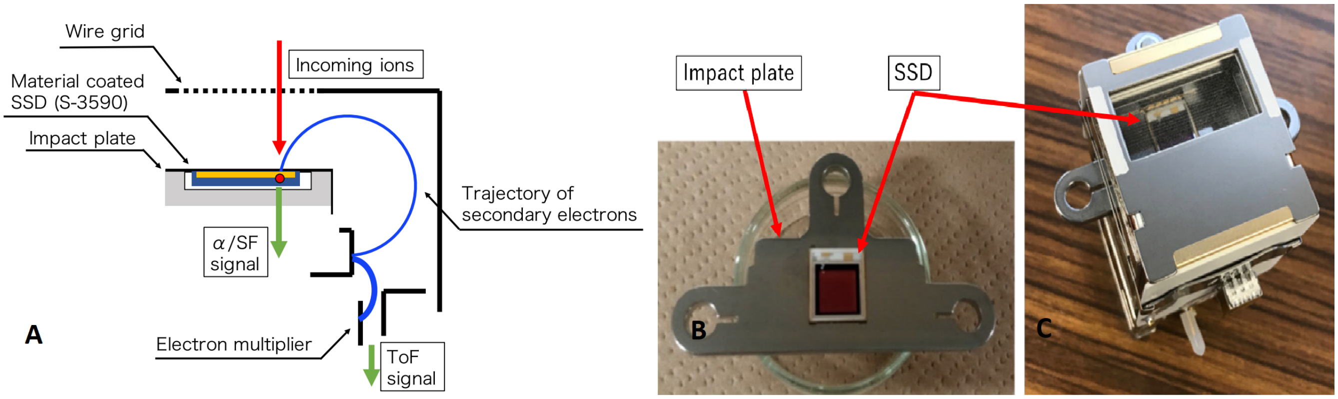

Figure 3.11: $\alpha-$TOF detector installed at the FRS-IC setup. In panel A) a scheme of the detector details is depicted, panels B) and C) show photographs of the front-side impact plate and the silicon surface barrier detector SSD, respectively [118].

As shown in Fig. 3.11, the α-TOF detector consists of an impact plate, at the center of which a silicon surface barrier detector (SSD, Hamamatsu S-3590, with an active area of 10 mm^2 and a depletion layer thickness of 0.3 mm) is mounted. The detector also includes an internal circuit for generating a suitable bias potential (50–100 V) for the SSD, permanent magnets, and an electron multiplier.

When an ion strikes the detector, it first hits the impact plate, causing the emission of secondary electrons. These electrons are isochronously guided by crossed electric and magnetic fields to an electron multiplier section, where they are amplified to produce a fast timing signal of the incident ions.

The impact plate and the SSD surface are both gold-coated and electrically connected via wire bonding to maintain a constant potential across the impact plate. In addition, the SSD surface is coated with an MgO layer of about 10 nm thickness to enhance secondary electron emission. During normal operation, the α-TOF detector impact plate is held at a high negative potential (approximately –2 kV), while the SSD is biased at –70 V by an optically isolated circuit, which also amplifies the decay signal.

The output from the Si detector is processed by two charge-sensitive preamplifiers with different gains, allowing the measurement of either α-particle signals (high-gain) or spontaneous fission signals (low-gain).

The Si detector data and the time-of-flight data are recorded separately, event by event, with absolute time stamps. Commissioning tests have demonstrated that the α-TOF detector achieves an energy resolution of 141.1(9) keV for 5.48 MeV α particles and a time resolution of 250.6(7) ps [118].

3.3 Technical improvements

The fission isomer experiments S530 at the FRS facility aimed to explore the island of fission isomers in the actinide region. In particular, with the FRS-IC setup the focus was directed towards measuring fission isomers with half-lives in the ms regime. Suitable fission isomer candidates in this region and available to be produced via projectile-fragmentation at the FRS, are ^{219}Ra (half-life 9.0(20) ms [122]) and ^{235}U (a recent study indicates a half-life of 11(3) ms [86]).

3.3.1 Installation of a shorter DC cage

Expecially for experiments involving isotopes with low production rates (such as fission isomers), the ability for a setup to handle higher beam rates is an important factor to be considered, since a higher beam current turns into a higher rate of recorded events of interest. For this reason at the FRS-IC a lot of effort was devoted to study the count-rate capability of the CSC when thermalizing the beam. This section describes studies of the rate capability when a DC cage with a length of 105.4 cm and a diameter of 25 cm is installed. These studies led to the development of a shorter DC cage to allow for detecting shorter-lived isotopes with increased impinging ion count rate. This new component was finally installed in the experiment S530.

As a starting point a SIMION simulation [107] was performed to determine the trajectories of the ions for being thermalized and extracted from the CSC together with the trajectories of He buffer gas ions created by the collisions between the beam particles and the He gas filling the CSC. For the simulation the applied external electric fields, the space charge field created by the ions and the mobility and diffusion of the ions in the helium stopping gas have been taken into account. The external electric fields were calculated from the voltages applied to the CSC's DC electrodes and the known geometry of the electrodes. The space charge fields were obtained using SIMION's Poisson solver, which implements a particle-in-cell method. The space charge potential has been recalculated at each time step of the simulation. The motion of the ions is given by the following formula:

$$\ddot{r} = \frac{e}{m}E - \frac{\dot{r}}{l}$$

where m, e and E are the mass, the charge and the electric field of an ion, $\ddot{r}$ and $\dot{r}$ denote the acceleration and velocity of the ion, respectively, while the influence of the helium stopping gas was considered by using the ion mobility l.

In this simulation (reported in [107]) only the transport of the ions from the beginning to the end of the DC cage have been considered, the motion on the RF carpet or in the nozzle was not included. Nevertheless, the measured extraction time is the sum of the motion up to the carpet plus the time of the ion's motion along the carpet.

In Figure 3.12, the simulated trajectories of the ions injected into the CSC are shown, as well as those of the He ions created in the CSC for two different beam intensities. The ions enter the CSC from the left side, and the DC electric field pulls them towards the

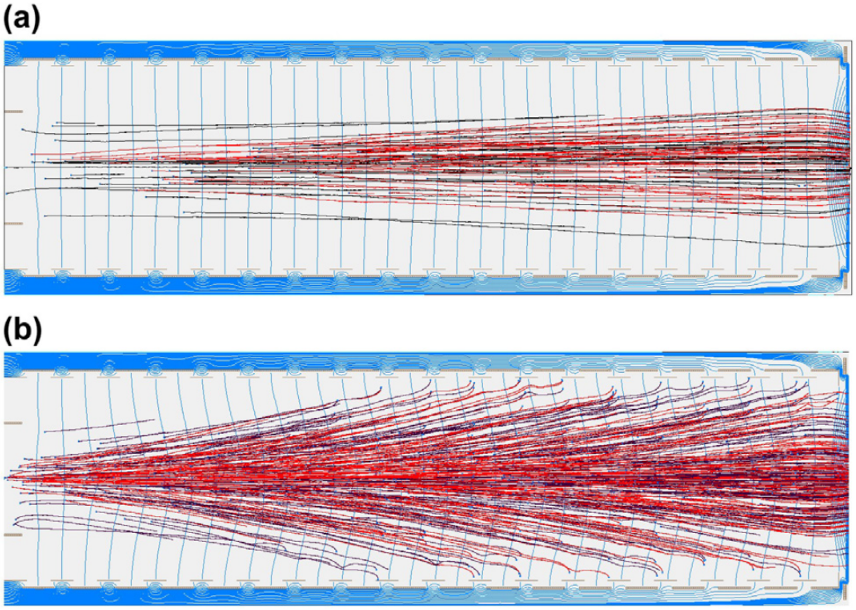

Figure 3.12: Equipotential lines (blue) of the electric field and trajectories of stopped ions (black) and He ions (red) in the CSC at two different ionization rates. The ions enter the CSC from the left and are transported to the RF carpet on the exit side of the CSC using electric DC fields. (a) At an ionization rate of 10^{11} $^3\mathrm{He}^+$/s all ions are transported to the RF carpet. (b) At an ionization rate of 10^{12} $^3\mathrm{He}^+$/s the ions stopped in the entrance region of the CSC are defocused by the space charge and impinge on the electrodes of the CSC [107].

extraction side of the CSC on the right side. At an ionization rate of 10^{11} $^3\mathrm{He}^+$/s, all ions are transported to the RF carpet. However, at a rate of 10^{12} $^3\mathrm{He}^+$/s, the space charge of the ions causes ion deflection. The ions that start in the entrance region of the CSC are deflected towards the ring electrodes of the CSC and are lost. Only ions originating from locations closer to the exit side of the CSC are extracted successfully. The simulation shows that the strength of the deflection increases with ionization density, and the region of ions to be successfully extracted is reduced to smaller volumes close to the extraction nozzle of the CSC.

Another aspect to be considered in the simulation is the spill length of the beam. For spill lengths much shorter than the time required for removal of the charge from the CSC, the space charge is not affected by the ion rate. Conversely, when the spill length is much longer than the time to remove the charges from the CSC, the strength of the space charge effect depends on the ion rate. The time defining the transition between these two regions is called the characteristic time t_{ch} and approximately given by the formula:

$$I = \frac{N}{\sqrt{t_{spill}^2 + t_{char}^2}}$$

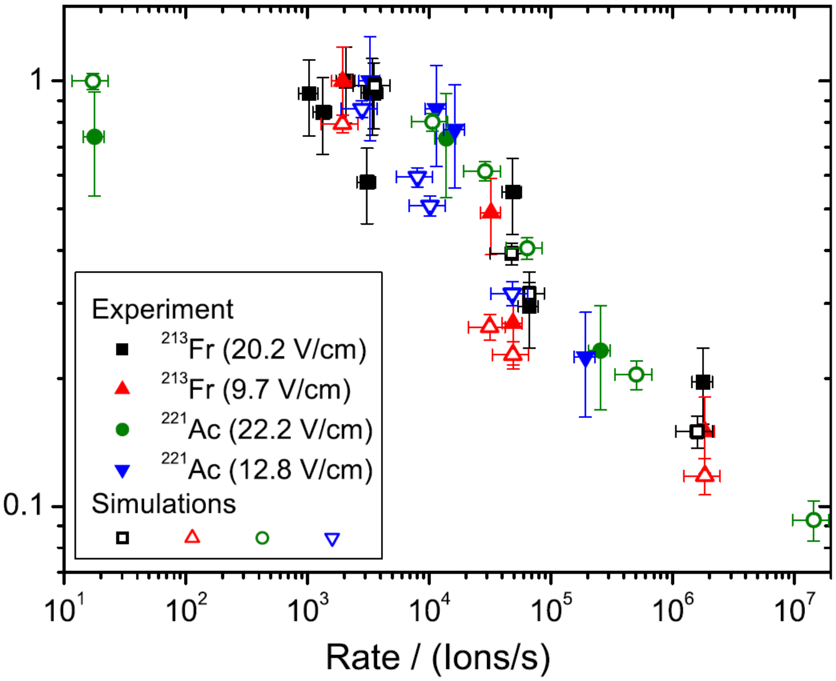

Figure 3.13: Extraction efficiencies for ^{213}Fr and ^{221}Ac in dependence of the beam rate from experiments (solid symbols) and simulations (open symbols) for two different electric DC field strengths. Every data series has been normalized independently to its maximum extraction efficiency of unity [107].

where I is the ionization rate of the DC beam in ion–electron pairs per unit time, N is the number of ion–electron pairs created by the pulsed beam and t_{spill} is the spill length of the pulsed beam.

The first online experimental investigation [107] included in the data shown in Fig. 3.13 was done for ^{213}Fr and ^{221}Ac fragments thermalized in the CSC with a spill length of $4-6$ ms and a time between spills of about 8 and 6 s, respectively. The rate has been converted to the equivalent rate of a DC beam and the extraction efficiencies were normalized to the maximum for each series. The extraction efficiency stays constant up to a rate of 10^4 ions/s injected into the CSC, while it decreases for higher beam rates. The extraction efficiency also increases, at a given beam rate, by increasing the DC field.

In a further study [109] it was investigated how the RF voltage at the RF carpet affects the rate capability in terms of extraction efficiency and space charge. This effect was neglected in the simulation. In this study a primary beam of ^{238}U with a spill length of 1 second was thermalized and the beam intensity was scanned at three different RF voltages applied to the RF carpet of 94 V_{PP}, 40 V_{PP}, and 28 V_{PP}, respectively, corresponding to ion transport efficiencies of 100%, 100% and 40%, respectively. The RF carpet settings did not influence the onset and the slope of the extraction efficiency trend. This result confirmed the hypothesis that the extraction efficiency decrease is due to the space-charge in the bulk of the stopping medium and not due to an insufficient repelling force exercised by the RF carpet, which could impact the ion motion in the region of the RF carpet or at the nozzle.

This analysis suggests that considering a modified DC cage filled with the same gas density, however shorter in length, could provide two benefits:

- For the same DC field as applied at a longer cage, the push field increases as does the extraction efficiency.
- At higher beam rates, when the ions start to deviate towards the DC electrodes, a shorter orthogonal dimension (for the beam with respect to the extraction plane) reduces the ion losses.

For those reasons a newly designed DC cage was installed during the commissioning of the experiment S530. The ring electrodes of the new DC cage have a 7% larger diameter and a length of 48.2 cm and 2.3 time smaller length-to-diameter aspect ratio. In Tab. 3.1 there is a comparison between the parameters of the long and the short DC cage. The latter enables the transport of ions that are stopped closer to the DC cage rings by reducing the near-field distortions. Simulations for these changes in the DC cage resulted in an increase of the stopping efficiency by up to 30% and a shorter mean extraction time of < 10 ms is expected. This estimation for the extraction time is the most important benefit of the short DC cage for the present fission isomer experiment, since only such a shorter extraction time enable the possibility of detection of isomers as ^{220}Ac and ^{235}U.

	Long DC cage	**Short DC cage**
Length	105.4 cm	48.2 cm
Ring inner diameter	25 cm	26.7 cm
Number of rings	36	14
Areal density	up to 9 mg/cm^2	up to 4.5 mg/cm^2 (expected)
Stopping efficiency	15-20%	up to 30% (expected)
Mean extraction time	25 ms	less than 10 ms (expected)
Rate capability	10^4 ions/s	>10^4 ions/s (expected)

Table 3.1: Comparison of Long and Short DC cages

In Sect. 5.1 the performance of the short DC cage under online conditions will be presented.

3.3.2 Repetition rate of the MR-TOF

The ions need time to be extracted from the CSC, to reach the MR-TOF and time to traverse the MR-TOF from the trap system to the detector. Each of these pathways need to be optimized with the respect to the time duration and efficiency. The first path is optimized by finding the DC value settings along the DC cage and the DC and RF fields applied to the RF carpet by measuring the decay rate registred from the ^{228}Th radioactive source on the Si detector installed in the DISTRICT module. The flight-time all along the beam line up to the top of the MR-TOF is brought to its achievable minimum by optimizing the voltage profile along the beamline together with the pressure conditions in the various sections. The best configuration is found by measuring the rate on a silicon detector installed at the entrance of the MR-TOF (or at the exit of the MR-TOF when knowing the expected efficiency). The shortest time for the ions to move from the top to the bottom of the MR-TOF is achieved by finding the best voltage setting for the MR-TOF's electrodes, the cycle time duration for its pulsed trapping potential and by reducing the repetition frequency. The repetition frequency, or repetition rate, is the inverse of the time needed for ions to propagate from the first trap to the detector (this is called the cycle time). For example, a repetition rate of 50 Hz allows for 20 ms as cycle time; in this case very short-lived exotic nuclei, with decay times shorter than 20 ms, would be cut off. Since one wants to be able to select the repetition rate according to the nuclear species of interest to be detected for a specific beam time, there is the need of a device to quickly change the MR-TOF repetition frequency in a user-friendly way by reading the time-averaged real voltages of the MR-TOF analyzer electrodes. To support a faster and more convenient change of the MR-TOF-MS repetition rate, an 8-fold resistive voltage divider has been installed, which enables a continuous monitoring of the voltages at the TOF analyzer electrodes. The voltage divider is mounted in a thermally insulated and heated aluminum enclosure. The enclosure is held at a constant temperature (within a 0.5 °C interval) by electronic control. Photograph of this device is shown in Fig. 3.14.

Figure 3.14: Voltage divider installed at the FRS-IC setup. It is made of an 8-fold resistive voltage divider, which enables a continuous monitoring of the voltages at the TOF analyzer electrodes.

3.4 Description of the data acquisition system at GSI

In this section the data acquisition system for experiment S530 will be discussed. Since only the data analysis regarding the FRS-IC setup (Sect. 3.2) has been taken into consideration for this thesis, the description of the data acquisition system is restricted to this part and is shown in Fig. 3.15. As explained in Sect. 3.2.3, at the end of the FRS-IC system are installed silicon detectors such as the MagneToF and the $\alpha-$ToF detectors. The last one provides two output signals, one for the time-of-flight signal and the second one dedicated to the energy signal. Starting from the time-of-flight output, the signal is sent to two time-to-digital converters (TDC) (both FAST Comtec model msca6) with a time resolution of 0.8 ns. To distinguish between the two, the first TDC is called TDC1, the other TDC2. At TDC 1 the time-of-flight signal is recorded as 'step signal', it receives its start signal generated by a TTL signal from a TTL box with 30 outputs each of them with a customized TTL signal. For the TDC 1 the TTL signal comes from output 10 and it restarts periodically every 5 ms with a 200 Hz repetition rate (ON for 100 μs then OFF for 4.9 ms). The start signal is in coincidence with the opening time of the exit mirror of the analyzer at the MR-TOF which runs at 200 Hz. The data are collected by the TOFControl software developed at Giessen University [123]. At the TDC 2 the first two channels are dedicated to record the ToF signal at different thresholds, a third channel takes the energy signal coming from the detector. At the TDC 2 the main aim was to measure the α energy signal from the $\alpha-$ToF detector, in particular to test its ability to differentiate the fission fragment (FF) events from the α decay events. Since the FF events occur at any time, the setup is made in a way to maximize the acquisition time and minimize the dead time window. The start time signal has been done by a TTL signal (output 12) of 100 μs ON/OFF that triggers on the output 10 signal. A scheme of this trigger signal is shown in Fig. 3.16. The energy output signal from the detector is also sent to a commercial digitizer module (CAEN, DT5780SDM [124]) as data acquisition (DAQ) module. This DAQ has an internal clock of 10 MHz and it records time stamp and energy of the events acquired.

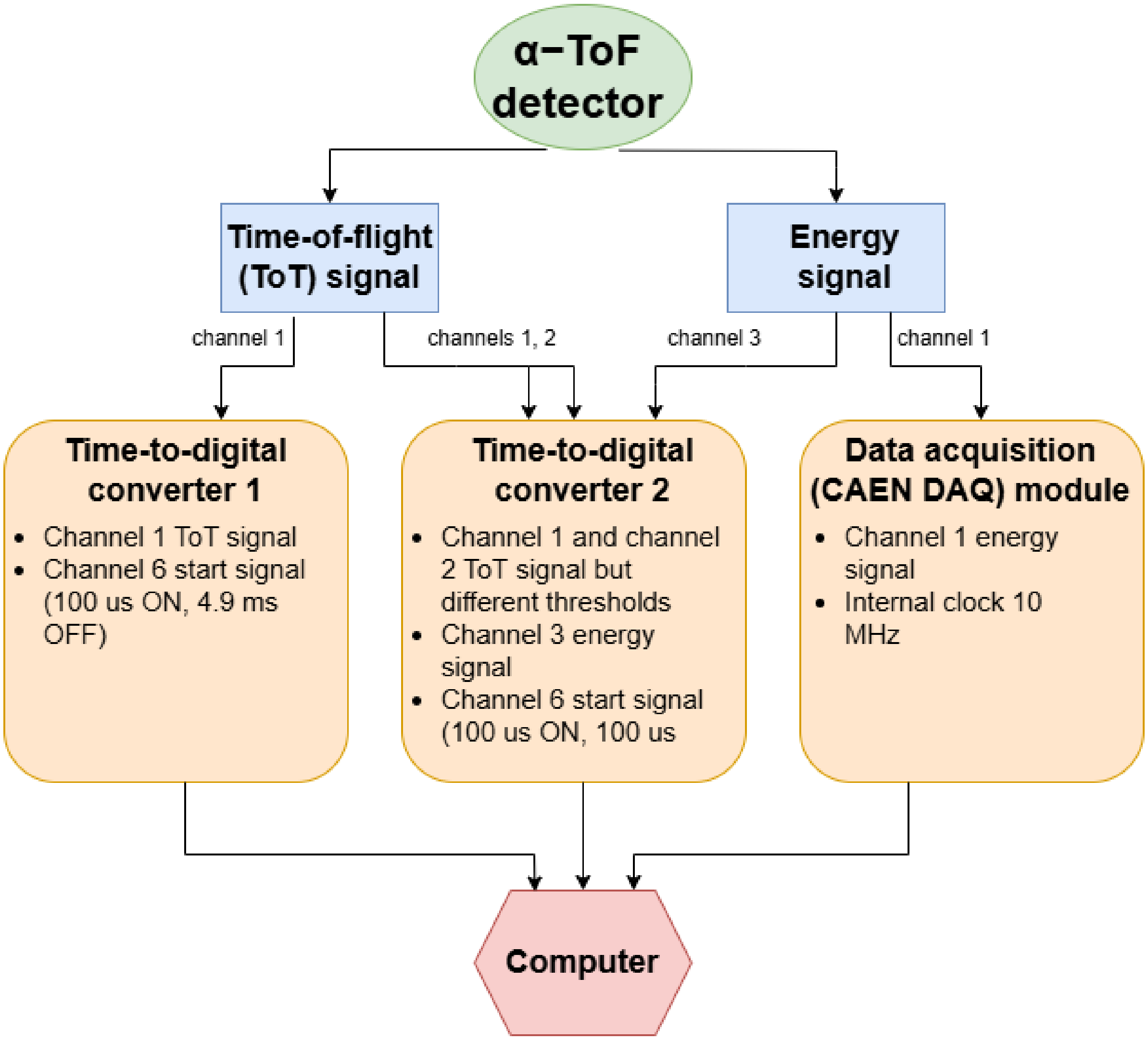

Figure 3.15: Block diagram of the signal processing and data acquisition system for the experiment S530. At the end of the FRS-IC system, silicon detectors such as a MagneToF and an $\alpha-$ToF are installed. The $\alpha-$ToF detector has been used for the data acquisition. It provides two signal outputs: one for time of flight (ToF) and another one for the energy signal. The ToF signal is routed to two FAST Comtec TDCs, with TDC 1 recording the ToF signal using a TTL start signal synchronized with the opening of the exit mirror of MR-TOF analyzer. Data collection is managed by the TOFControl software from Giessen University. TDC 2 captures the ToF at varying thresholds and the energy signal from the detector, aiming to distinguish an α decay event and a fission fragment (FF) event. TDC2 is triggered by a 100 μs TTL signal at 1 ms intervals. The energy channel also connects to a CAEN DT5780SDM digitizer with an internal clock of 10 MHz.

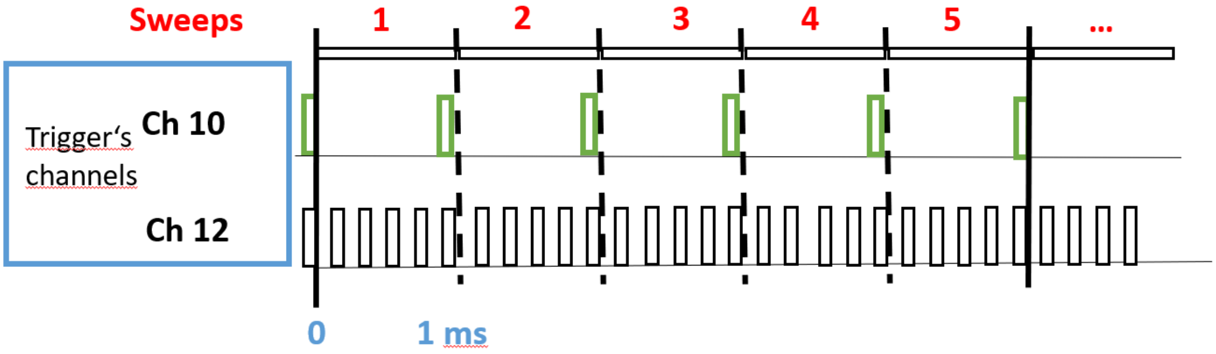

Figure 3.16: Sketch of the start time signal for the TDC 2 module provided by a TTL signal (output 12 of the TTL generator box) of 100 μs ON/OFF that triggers on the output 10 (signal generated by the TTL generator box at channel 10) (100 μs ON/ 0.9 ms OFF).

3.5 Fission Isomer Experiment at IGISOL

The IGISOL facility, renowned for its high performance and scientific impact, was employed to determine the excitation energies of fission isomers during an experimental campaign at the accelerator laboratory of the University of Jyväskylä (JYFL), Finland. In this experiment (coded as I290), fission isomeric states in ^{240}Am and ^{242}Am were populated through fusion-evaporation reactions induced by deuterons from the K130 cyclotron impinging on a ^{242}Pu target (^{242}Pu(2d,2n) ^{242f}Am or ^{242}Pu(2d,4n) ^{240f}Am). The target was produced at the University of Mainz using the drop-on-demand (DoD) inkjet printing method [125] and was installed in a light-ion guide within the target chamber. From there reaction products were extracted via gas flow within a short time frame, approximately one millisecond [126]. Within this time window, potential contamination products with short half-lives (like the fission isomer ^{243f}Pu with a half-life of about 45 ns) will not survive long enough to reach the detector, whereas longer-lived ions, such as the 14 ms fission isomer in ^{242}Am, can be extracted and accelerated towards the detection stations. After mass separation via a magnetic dipole, the selected ions of interest will be implanted into a system of silicon detectors, and their decay via fission will be recorded. With the silicon detector registering individual fission fragments from the fission isomeric states, the yields of fission isomers ^{240f}Am and ^{242f}Am at various beam energies, along with their decay times and excitation energies, can be measured. The setup of three silicon detectors and the correlated acquisition system will be described below.

The fission isomer in ^{242}Am was also measured using the MR-TOF-MS. Despite being installed downstream of the entire setup and requiring a separation time of about 10 ms, the 14 ms fission isomer in ^{242f}Am can still be measured, although this comes with a 50% decay loss. This measurement made for multiple beam energies yields the excitation energy function of the fission isomer ^{242}Am. In contrast, this is not feasible for the fission isomer ^{240f}Am due to its short half-life of 0.9 ms.

While the half-lives for the isomeric states were measured using the silicon detectors (as will be discussed in the next Sect. 3.6), the half-lives of the ground states of ^{240}Am and ^{242}Am, which are 50.8(3) hours and 16.02(2) hours, respectively, were determined by transporting the ions to the JYFLTRAP Penning trap system. The ratio of fission isomer to ground state yields provides the population ratio between the two and will not be presented here, as the analysis is still being carried out by other members of the collaboration.

The IGISOL setup discussed here in the configuration prepared for the experiment I290 is shown in Fig. 3.17.

The half-life values for the isomers ^{240f}Am and ^{242f}Am are well established from previous indirect measurements [127]. However, the new measurements presented here demonstrate that the study of fission isomers is feasible at IGISOL, along with direct mass measurements of ^{240}Am and ^{242}Am, as well as measurements of the excitation function and excitation energy for the fission isomeric state in ^{242}Am. The accessibility of this isomeric state is crucial, as ^{242m}Am is a candidate for investigating the fundamental nuclear excitation mechanism of excitation via nuclear electron capture (NEEC) [58, 59, 60, 128].

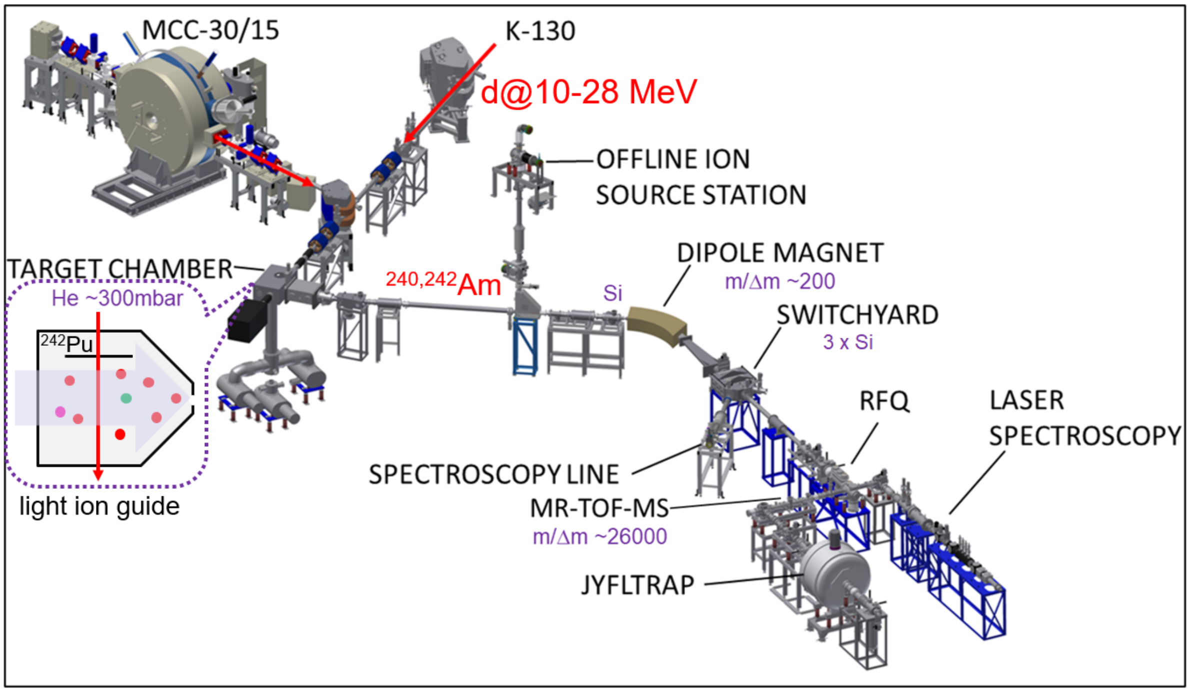

Figure 3.17: IGISOL setup prepared for experiment I290. The production of fission isomers ^{242f}Am and ^{240f}Am is achieved by light ion fusion-evaporation reactions with the light-ion guide where a deuteron beam of 10 to 28 MeV produced by the K130 cyclotron impinges on a ^{242}Pu target. The separation and selection of the ions of interest is done by the dipole magnet at IGISOL. The selected beam proceeds towards the switchyard on 3 Si detectors here installed or it proceeds downstreams to the MR-TOF.

3.6 Description of the data acquisition system at IGISOL

This section focuses on the presentation of the signal processing and data acquisition of the silicon detectors positioned at the switchyard, since only this part will be used for the data analysis discussed in the next chapter. At the switchyard, three silicon detectors (Ortec TB-22-200-300) [129] are installed in the geometrical configuration shown in Fig. 3.18. The detectors are called 0,1 and 2 looking from the left side. Detector 1 is oriented such that it aligns with respect to the beam direction, while the detectors on the left and right are mounted at 90° relative to the beam and the control detector. The detector signals are sent to an ORTEC-142 preamplifier and then to a three channels of a four-channel MCA digitizer DT5724. To determine the time when the signal yield growth after the implantation in one of the detectors stops and the decay starts, a signal derived from the electrostatic kicker that determines the beam direction in the switchyard was used as trigger signal. The ion beam is sent to the switchyard and to the MR-TOF in a specially selected fine structure based on the fission isomer of interest as indicated in Fig. 3.19. Therefore, the beam changes its direction after a time equal to 3-4 times the half-life of the isomer. The kicker signal encodes the time when the beam changes its direction towards the MRTOF or the Si detectors. This logic signal is recorded in the fourth channel of the DT5724 digitizer. The acquisition system provides data in text file format as will be explained in Section 4.1, but this time a fourth column is included to identify the origin of the signal. Channel 1-3 represent Si detectors, channel 4 contains the kicker signal information.

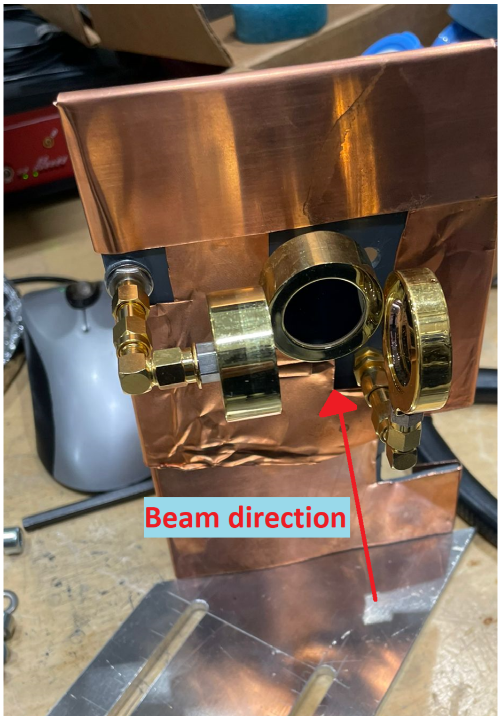

Figure 3.18: Silicon detectors installed at the switchyard of the beam line system (see Fig. 3.17). The detectors are labelled 0,1 and 2 looking from the left side. The detector 1 is oriented in a way that it aligns with the beam direction, the detectors on the left and right are mounted at 90° relative to the beam direction and the central detector.

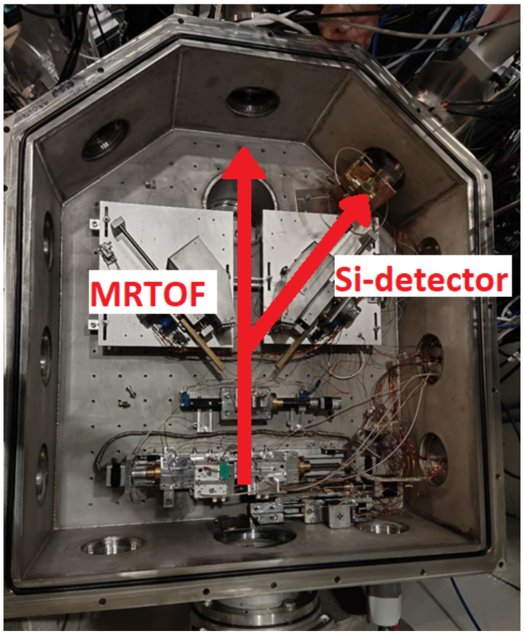

Figure 3.19: Top view of the beam switching device allowing to direct the ions towards the MR-TOF (straight arrow) or alternatively to the arrangement of the three silicon detectors shown in Fig. 3.18. The ion beam is sent via the switchyard either to the MR-TOF or on the silicon detectors in a specifically selected time-structure based on the expected half-life of the fission isomer of interest. Therefore, the beam changes direction periodically after a time equal to 3-4 times the half-life of the isomer. The kicker signal encodes the time when the beam changes direction.

Chapter 4

Experimental procedure and data analysis

During experiment S530, projectile fragmentation of a ^{238}U primary beam at an energy of 1000 MeV/u was carried out using a beryllium target with an areal density of 0.66 g/cm^2. The secondary beams were separated and identified in-flight at the Fragment Separator (FRS).

Initially, a secondary beam was selected at the FRS to test the alignment between the beam exiting the FRS and entering the CSC. This process was performed in two steps, using the monoenergetic achromatic degrader at the FRS and the variable degrader positioned at the final focal plane between the FRS and the CSC (for the layout of the degrader installation, see Fig. 3.2).

In the first step, the monoenergetic achromatic degrader is used for mean range bunching. This involves adjusting the degrader thickness until finding a value that allows multiple ion beam species, that have been selected and transported up to that point, to pass through the degrader with maximum efficiency. In Fig. 4.1 is shown the case of a degrader scan made during S530. The ions $^{237-234}$U^{16}O^{++} from the FRS move to the MRTOF where the number of counts is measured for each detected ion species, and normalized by the number of ions of the separated beam that impinges onto the scintillator detector positioned in the final focal plane before entering the CSC. The measurement is repeated for different degrader thicknesses. The final degrader thickness is chosen as the one that allows the transport of all ion species with maximum intensity. Accordingly to Fig. 4.1, this value amounted to 4710 mg/cm^2.

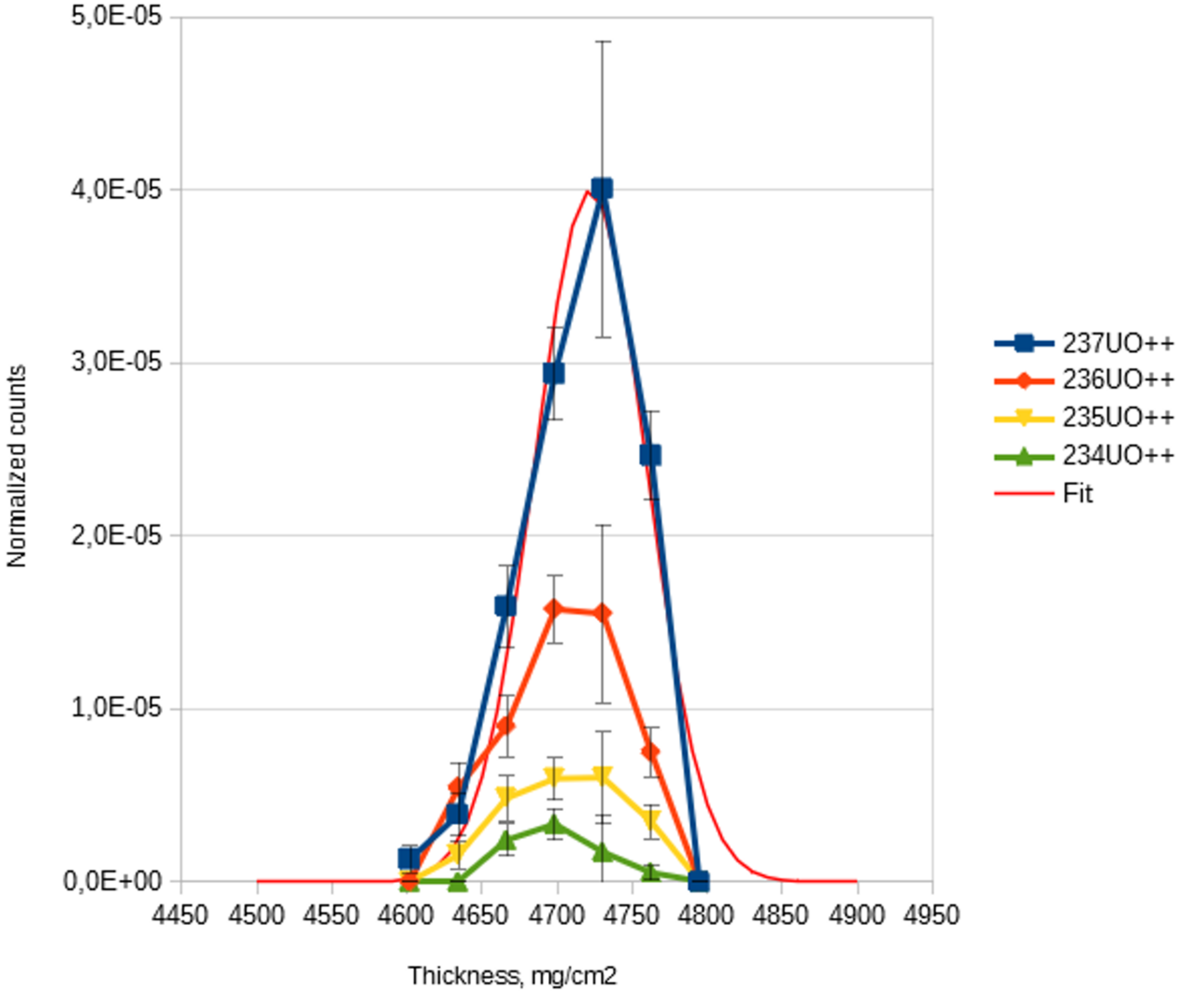

Figure 4.1: Thickness selection for the monoenergetic achromatic degrader behind the FRS. The $^{237-234}U^{16}O^{++}$ ion counts are measured by the MRTOF and normalized to the number of ions detected by the scintillator in the final focal plane before the CSC. The measurement is repeated for various degrader thicknesses, with the optimal thickness of 4710 mg/cm^2 selected to achieve maximum transport efficiency for all ion species.

The second step focuses on optimizing the beam exiting the FRS. This optimization procedure sets the degrader thickness of the variable degrader to maximize the number of ions stopped at the mid-length of the CSC. In Fig. 4.2 is shown a case of a variable degrader scan made during S530. In the case presented, the degrader thickness optimization refers to the case of $^{235}U^{16}O^{++}$. The number of counts are measured by the MRTOF and normalized to the counts of the ion beam impinging onto the scintillator detector while scanning multiple degrader thicknesses. The optimum thickness coincides with the mean value of the fit function of the acquired data points, in the case shown is 4735 mg/cm^2.

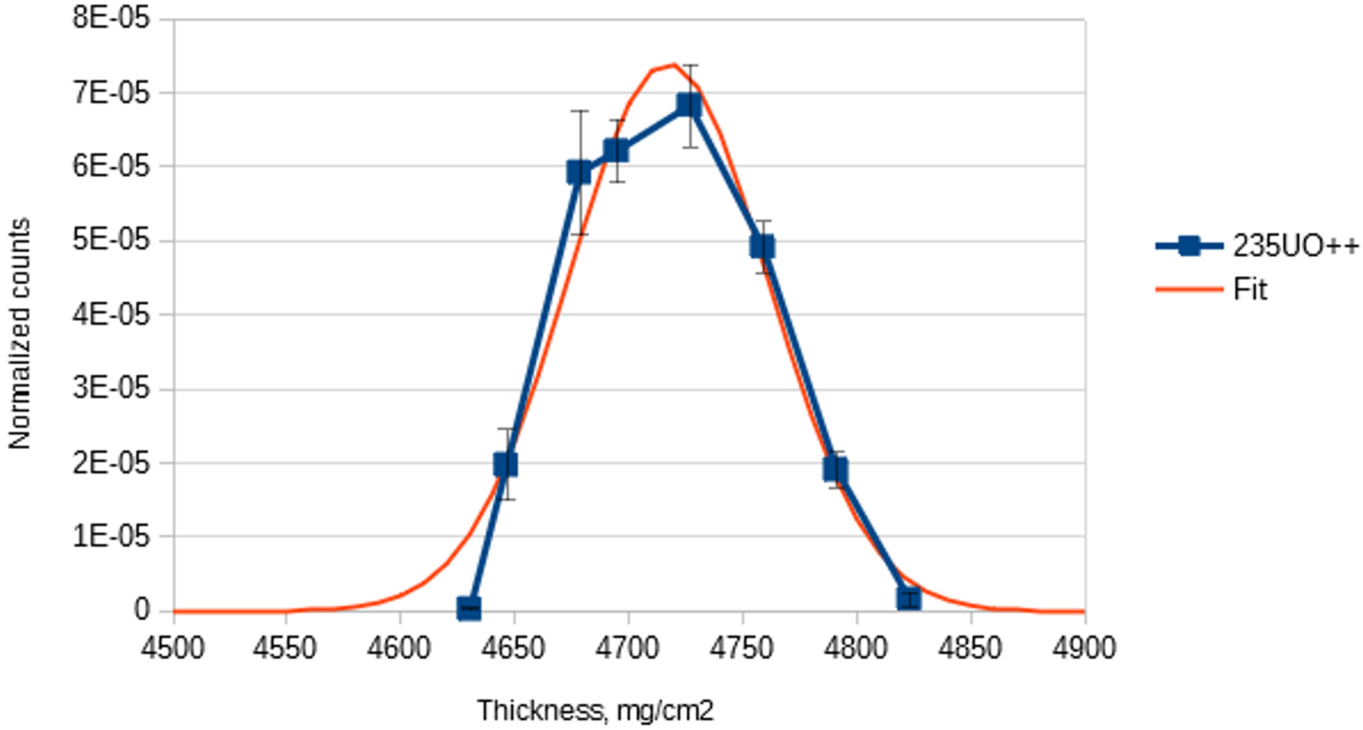

Figure 4.2: Thickness selection for the variable degrader. The degrader thickness optimization is specific to $^{235}U^{16}O^{++}$ ions. Counts are measured by the MRTOF and normalized to the number of counts of the ion beam acquired with the scintillator detector, using multiple degrader thicknesses. The optimal thickness corresponds to the mean value of the Gaussian fit function applied to the acquired data points, here amounting to 4735 mg/cm^2.

For the S530 experiment, the ion beam, produced by the fragmentation reaction and selected by the FRS, is injected into the CSC, which is filled with helium at an areal density of (1.09 ± 0.15) mg/cm^2 (i.e., a pressure of (35 ± 5) mbar and a temperature of 75 K) and subjected to a DC push field of 30.4 V/cm. The RF carpet was operated with 100% ion transport efficiency.

The ions extracted by the CSC continue their trajectories along the beamline, reaching the MRTOF and eventually impinging on the detector at its end.

During the beamtime the FRS selected mainly three secondary beams for the acquisition with the FRS-IC:

- Beam transport $^{234-236}$U
- Beam transport $^{223-224}$Th
- Beam transport $^{220-221}$Ac

The selection settings applied at the FRS are tested online using the PID detectors. From the information taken by both PID detectors and knowing the spatial distance between them, a plot similar to the one in Fig. 4.3 is produced. It shows a PID plot for the selection settings centering $^{235-236}$U. The y-axis shows the atomic number, while the x-axis displays the mass over charge ratio. The identification made via the PID detectors allows to determine which species are transported further and to set the MRTOF parameters accordingly to allow the same species to be detected. The way these species are identified and characterized with the FRS-IC is presented in the following sections.

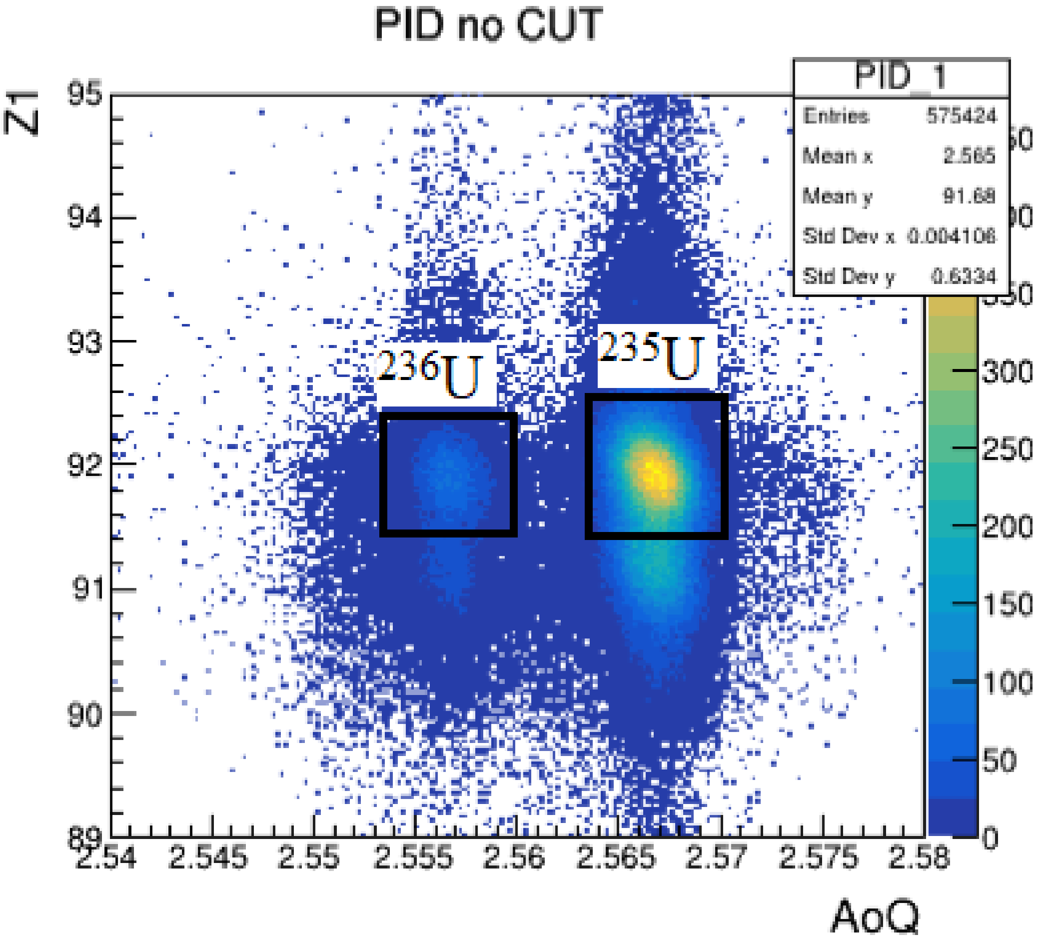

Figure 4.3: An example of a PID plot at the focal plane of the FRS is shown. The FRS selection settings were chosen to center $^{235-236}$U. On the y-axis the atomic number is plotted, while on the x-axis the mass over charge ratio is shown. The particle identification made via the PID detectors allows to determine which species are further transported downstream and to set the MRTOF parameters accordingly to allow the same species to be detected.

4.1 Data acquisition for alpha energy spectra

For each selection settings applied to the FRS, data have been acquired in multiple ways as illustrated in Fig. 3.15. This section is dedicated to the acquisition of events from the energy channel of the α - TOF detector. The data file generated by the CAEN DAQ module is a text file with 3 columns: i) absolute time (clock runs continuously from the start of the acquisition) for each event in 10 ns units, ii) energy given in digital channel units (needs to be calibrated using the internal ^{228}Th calibration source), iii) extra information about the way a certain event has been acquired (for example when a dead time occurred before a recorded event).

Looking at the alpha energy spectra acquired with the CAEN DAQ digitizer, it is possible to obtain a quick online identification of the beam selection. Indeed, knowing the alpha decay line of the ions transported in the beam, it was possible to see if the alpha energy decay signal was registered in the expected spectral region and thus confirm the selection settings. The α energy decay lines expected for the $^{223-224}$Th and $^{220-221}$Ac selections are reported in the following Tabs. 4.1 and 4.2, respectively. In the case of the settings for $^{234-236}$U, the expected alpha lines appear in this case the dominant low - energy tail region of the ^{212}Po peak at 8784 keV originated from the ^{228}Th internal source and therefore an online identification, was not possible. The energy resolution achieved for the online α - energy registration amounted to 150 keV.

Isotope	**Half-life**	**Intensity %**	**Energy (keV)**
220Ac	26.4 ms	9	7652
		11	7709
		10	7792
		26	7855
		8	7670
221Ac	52 ms	7	7374
		20	7437
		72	7642
216Fr	0.7 μs	10	8933
217Fr	22 μs	100	8315
213At	124 ns	100	9079
212At	558 ns	31	7888
		68	7826

Table 4.1: Decay data for isotopes of the $^{220-221}$Ac FRS selection settings. In the table are reported the half-life, the energy for the alpha decay and the related intensity for the isotopes listed [122]

.

The energy spectra acquired online are calibrated based on the alpha - energy lines obtained from the internal ^{228}Th source (as listed in Tab. 4.3).

Isotope	**Half-life**	**Intensity %**	**Energy (keV)**
223Th	0.6 s	26	7286
		55	7298
		13	7323
224Th	1.04 s	19	7000
		79	7170
219Ra	9 ms	66	7678
		30	7988
220Ra	18 ms	99	7453
215Rn	2.3 μs	100	8674
216Rn	45 μs	100	8050
211Po	0.5 s	99	7450
212Po	295 ns	42	10180

Table 4.2: Decay data for isotopes for the $^{223-224}$Th FRS selection settings. In the table are reported the half-life, the energy for the alpha decay and the related intensity for the isotopes listed [122]

.

Isotope	**Energy (keV)**	**Decay time ($\mathbf{T_{1/2}}$)**
224Ra	5685	3.26 d
220Rn	6288	55.6 s
216Po	6778	0.145 s
212Bi	6090	60.55 m
212Po	8784	0.299 μs

Table 4.3: Isotopes from the decay chain of the internal ^{228}Th source calibration with corresponding α energies and decay half-lives.

The peaks related to those lines are fitted by a multi-Gaussian fit as shown in Fig. 4.4. The multi-Gaussian peak fit provides the line centroid and width (sigma) of the α-decay lines. The centroid values are used to determine a linear calibration function (in keV) for the spectra.

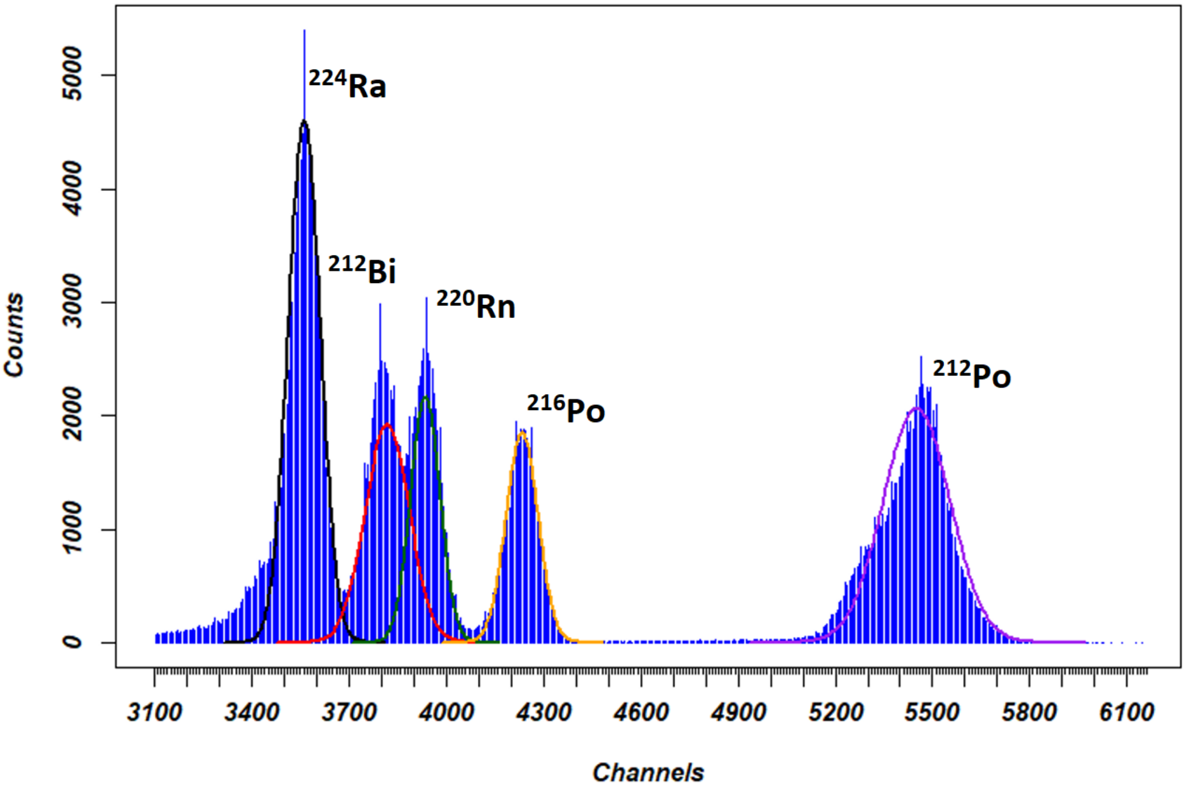

Figure 4.4: Multi-Gaussian fit of the calibrant peaks obtained from the internal ^{228}Th source. The multi-Gaussian peak fit provides the peak and the sigma of α decay lines.

In Figs. 4.5 and 4.6 the calibrated α - energy spectra are shown for the acquisition settings of $^{220-221}$Ac and $^{223-224}$Th, respectively.

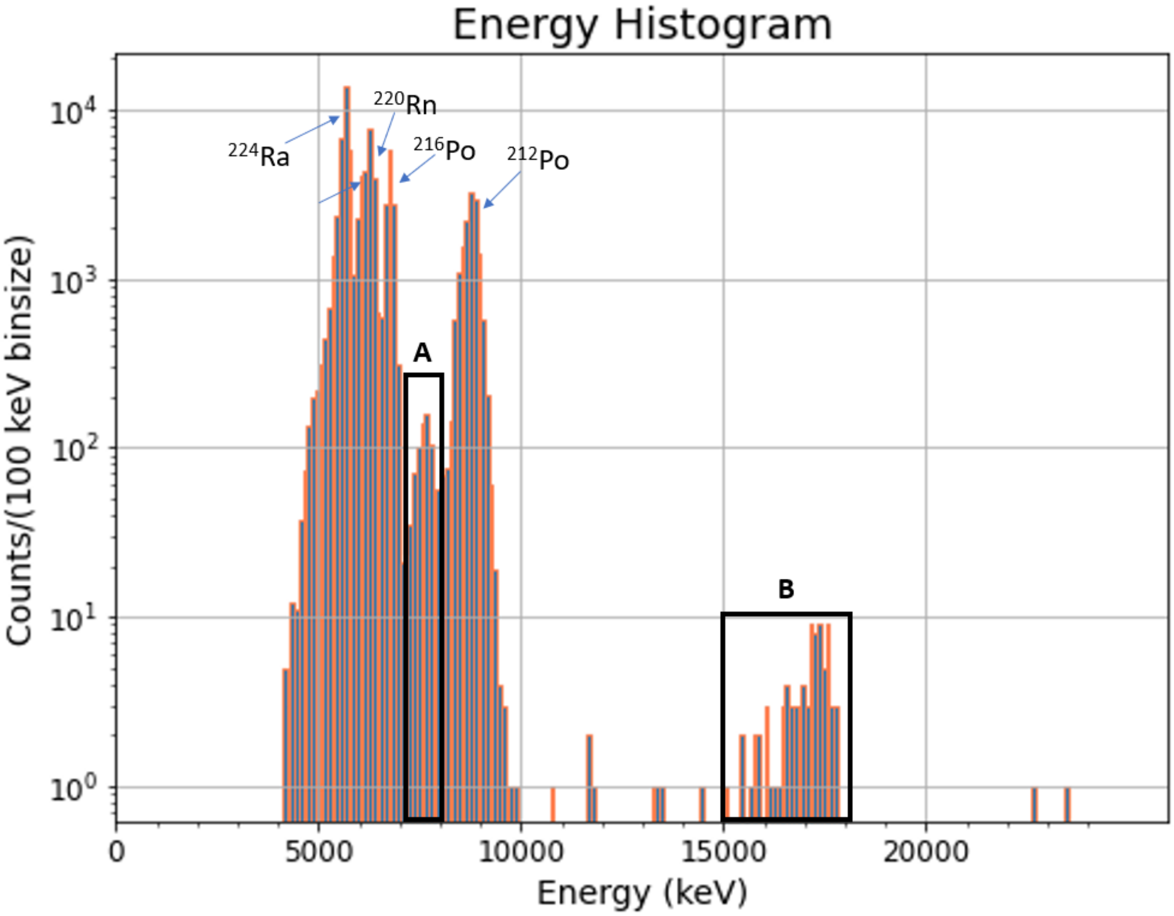

Figure 4.5: Calibrated α - energy spectra for the FRS acquisition settings of $^{220-221}$Ac. The dominant peaks correspond to the internal ^{228}Th source, as indicated, while the black rectangle A marks the region where alpha decay events are expected to show up and the black rectangle B indicates the area where their summing coincidences are expected (see Tab. 4.1) based on the beam settings. The broadest high-energy peak in B suggests overlapping contributions from coincident alpha decay lines, as its width exceeds the expected 200 keV for a single pair of coincident α decays.

The strongest peaks in Fig. 4.5 are those related to the internal source ^{228}Th as indicated in the picture, while the regions delimited by the two black rectangles indicate the region of the spectra where alpha decay events (A) or summing coincidences of these events (B) should appear, as expected by the FRS beam separation settings. Although alpha spectroscopy is not the main focus of this discussion, it is interesting to invest a closer look on the highest energy part within the "B"-area that is found in both Figs. 4.5 and 4.6 but in a different energy range. Those peaks are candidates for a distribution of

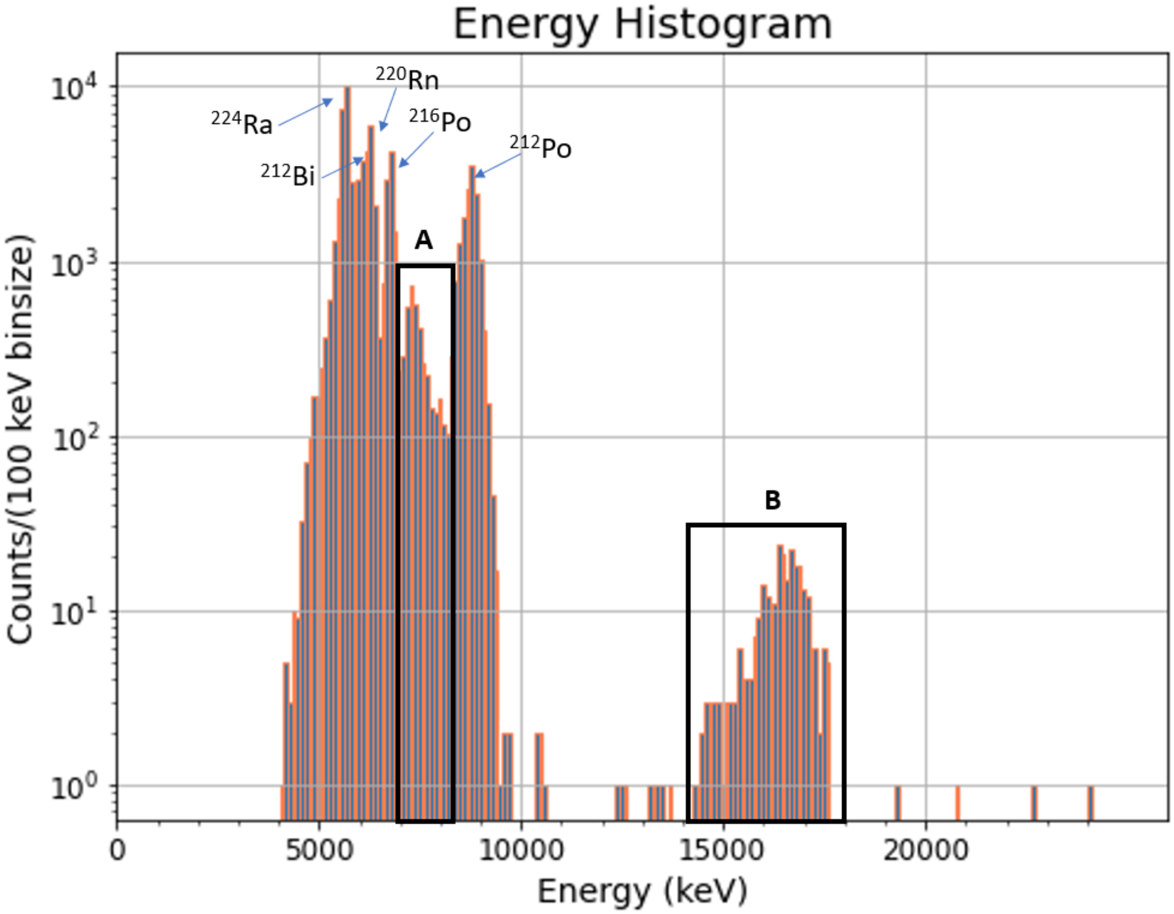

Figure 4.6: Calibrated energy spectra for the FRS acquisition settings of $^{223-224}$Th. The dominant peaks correspond to the internal ^{228}Th source, as indicated, while the black rectangle A marks the region where alpha decay events are expected to show up and the black rectangle B indicates the area where their summing coincidences are expected (see Tab. 4.2) based on the beam settings. The broadest high-energy peak in B suggests overlapping contributions from coincident alpha decay lines, as its width exceeds the expected 200 keV for a single pair of coincident α decays.

coincident alpha decay lines from the internal source and from the beam. The width of the spectral feature in area B by far exceeds the convoluted line width of two coincident α-energies, which would result in about 200 keV from the individual resolution of 150 keV. Therefore it has to be concluded that in this highest - energy part of the spectrum overlapping contributions from coincident α - transitions (from the internal calibration source and beam-related decay events) will show up.

To verify this hypothesis, the energy sum for each possible pair of α - decay energies has been considered, including the probability for a certain coincidence combination via the product of the intensity of alpha decays involved in possible coincidences, have been com-

piled together with a normalized probability.
Figures 4.8, 4.7 show a sum matrix for the combination of any possible coincidence of two alpha decay lines detected by the α-TOF detector. The elements of the matrix reflect the sum of the energies of the two coincident α decays. The probability for each element of the matrix is shown with a color code as represented by the colorbar on the right of the matrix plot.
The matrix values in yellow and light green have, based on this simple probability calculation, the highest probability to happen. As expected, the energy of those combinations appears in the range of the energy distribution of the high - energy feature in the B area of Fig. 4.7 and 4.8 we are investigating and, moreover, the combinations with lowest probabilities are excluded by the energy range of interest. For the Ac setting, the most likely pile up or summing coincidences occur between the 8375 keV α - line from ^{217}Fr with the 9079 keV α - line from ^{213}At, while for the Th settings more combinations contribute the spectral range from 17 - 18 MeV in Fig. 4.6, as visible by the yellow marked combinations in Fig. 4.8.

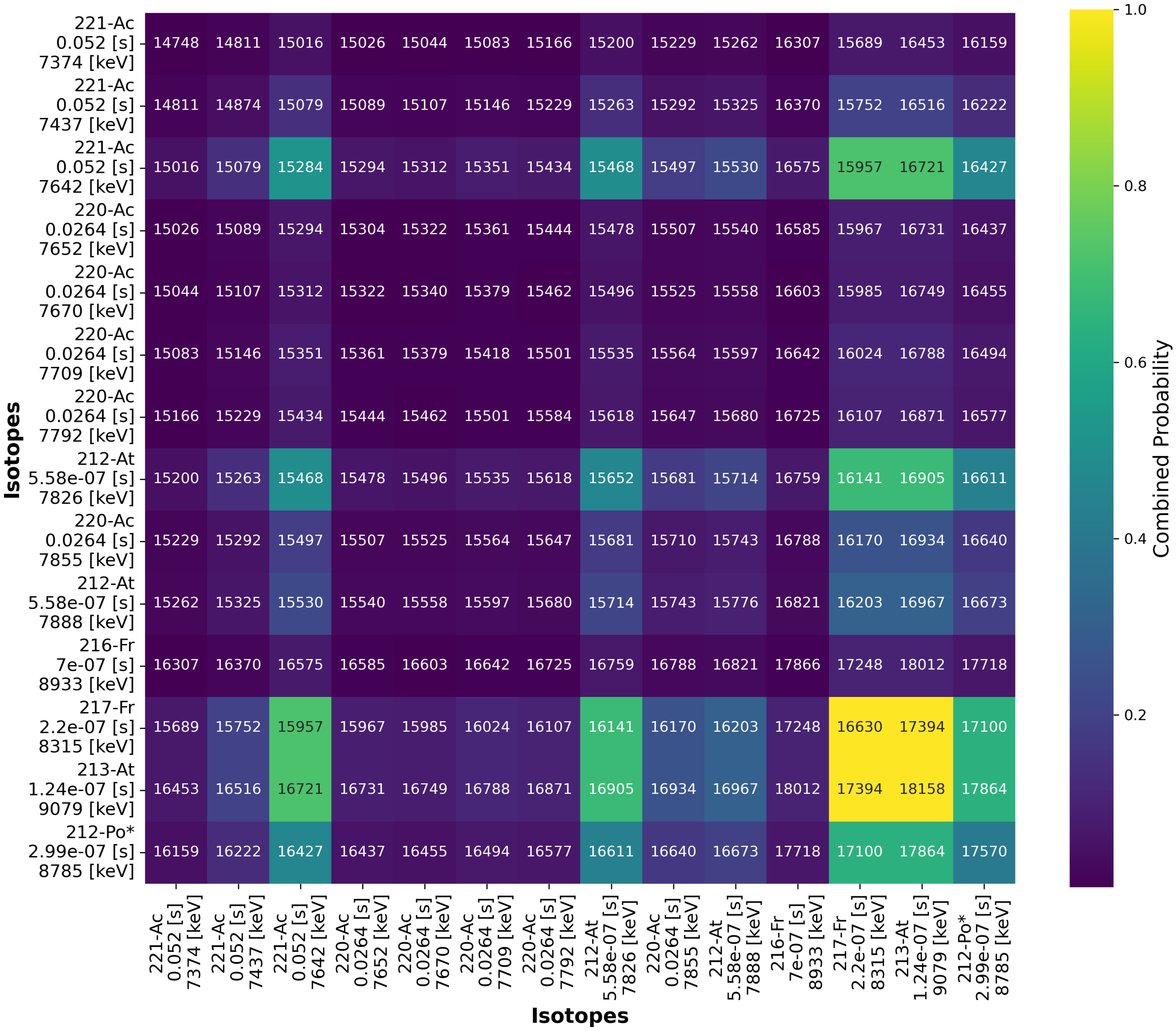

Isotopes	221-Ac 0.052 [s] 7374 [keV]	221-Ac 0.052 [s] 7437 [keV]	221-Ac 0.052 [s] 7642 [keV]	220-Ac 0.0264 [s] 7652 [keV]	220-Ac 0.0264 [s] 7670 [keV]	220-Ac 0.0264 [s] 7709 [keV]	220-Ac 0.0264 [s] 7792 [keV]	212-At 5.58e-07 [s] 7826 [keV]	220-Ac 0.0264 [s] 7855 [keV]	212-At 5.58e-07 [s] 7888 [keV]	216-Fr 7e-07 [s] 8933 [keV]	217-Fr 2.2e-07 [s] 8315 [keV]	213-At 1.24e-07 [s] 9079 [keV]	212-Po* 2.99e-07 [s] 8785 [keV]
221-Ac 0.052 [s] 7374 [keV]	14748	14811	15016	15026	15044	15083	15166	15200	15229	15262	16307	15689	16453	16159
221-Ac 0.052 [s] 7437 [keV]	14811	14874	15079	15089	15107	15146	15229	15263	15292	15325	16370	15752	16516	16222
221-Ac 0.052 [s] 7642 [keV]	15016	15079	15284	15294	15312	15351	15434	15468	15497	15530	16575	15957	16721	16427
220-Ac 0.0264 [s] 7652 [keV]	15026	15089	15294	15304	15322	15361	15444	15478	15507	15540	16585	15967	16731	16437
220-Ac 0.0264 [s] 7670 [keV]	15044	15107	15312	15322	15340	15379	15462	15496	15525	15558	16603	15985	16749	16455
220-Ac 0.0264 [s] 7709 [keV]	15083	15146	15351	15361	15379	15418	15501	15535	15564	15597	16642	16024	16788	16494
220-Ac 0.0264 [s] 7792 [keV]	15166	15229	15434	15444	15462	15501	15584	15618	15647	15680	16725	16107	16871	16577
212-At 5.58e-07 [s] 7826 [keV]	15200	15263	15468	15478	15496	15535	15618	15652	15681	15714	16759	16141	16905	16611
220-Ac 0.0264 [s] 7855 [keV]	15229	15292	15497	15507	15525	15564	15647	15681	15710	15743	16788	16170	16934	16640
212-At 5.58e-07 [s] 7888 [keV]	15262	15325	15530	15540	15558	15597	15680	15714	15743	15776	16821	16203	16967	16673
216-Fr 7e-07 [s] 8933 [keV]	16307	16370	16575	16585	16603	16642	16725	16759	16788	16821	17866	17248	18012	17718
217-Fr 2.2e-07 [s] 8315 [keV]	15689	15752	15957	15967	15985	16024	16107	16141	16170	16203	17248	16630	17394	17100
213-At 1.24e-07 [s] 9079 [keV]	16453	16516	16721	16731	16749	16788	16871	16905	16934	16967	18012	17394	18158	17864
212-Po* 2.99e-07 [s] 8785 [keV]	16159	16222	16427	16437	16455	16494	16577	16611	16640	16673	17718	17100	17864	17570

Figure 4.7: Sum energy matrix for the FRS $^{220-221}$Ac settings. The sum matrix shows all foreseeable combinations of coincident alpha - decay energies detected by the α-TOF detector, represented by the summed energy of the two coincident alpha decays. The probabilities of these combinations, calculated as the normalized product of the intensity value of the coincident alpha - decay energies, are displayed with a color code as indicated by the colorbar. The highest-probability combinations (yellow and light green) align with the energy range of the investigated peak, while the lowest-probability combinations fall outside the relevant energy range. The ^{212}Po* is the only alpha decay line related to the internal source that has been taken into consideration, since the other lines have too low energies to compete with the coincidence events that populate the considered spectral range from 17-18 MeV in Fig. 4.5.

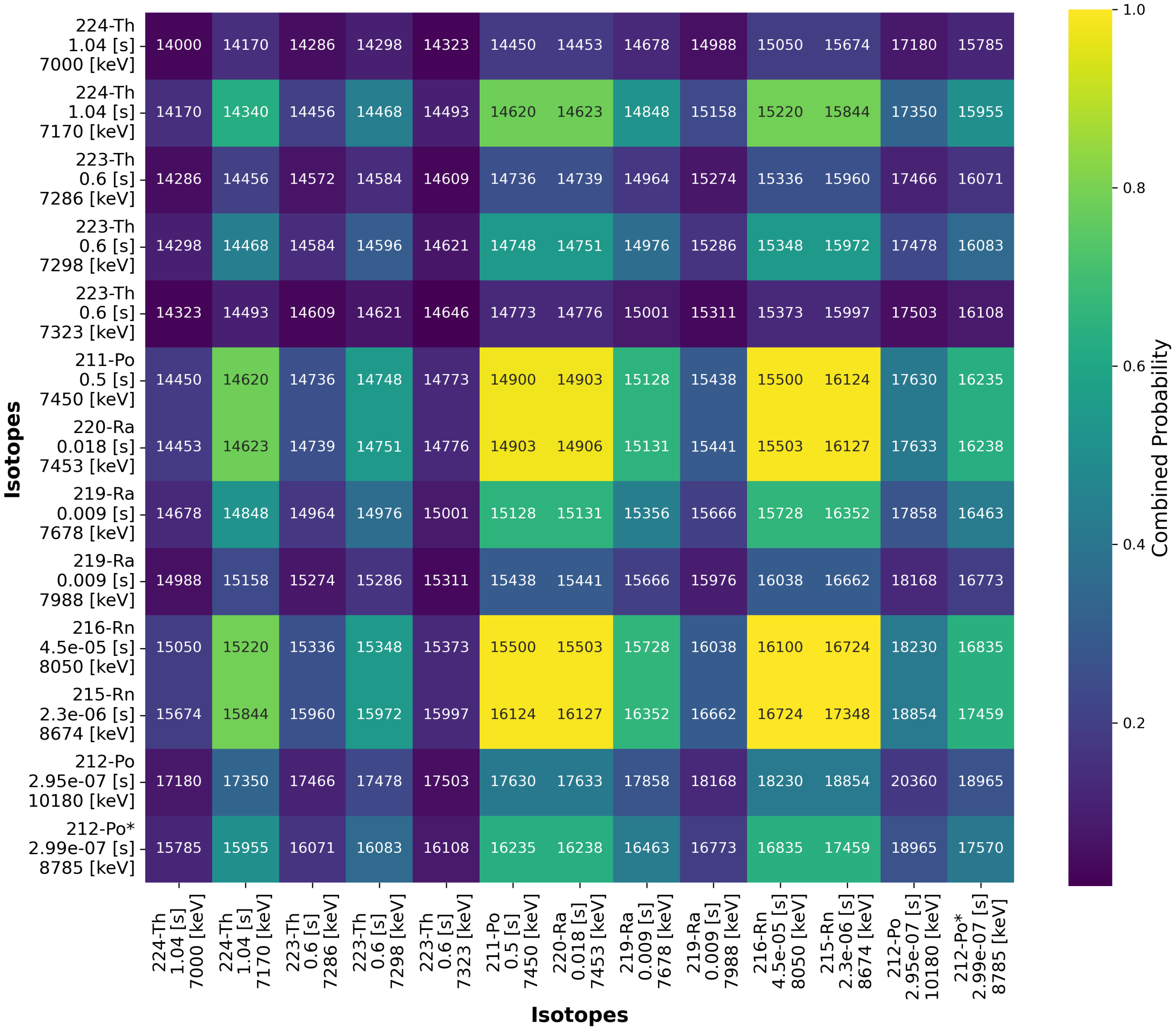

	224-Th 1.04 [s] 7000 [keV]	224-Th 1.04 [s] 7170 [keV]	223-Th 0.6 [s] 7286 [keV]	223-Th 0.6 [s] 7298 [keV]	223-Th 0.6 [s] 7323 [keV]	211-Po 0.5 [s] 7450 [keV]	220-Ra 0.018 [s] 7453 [keV]	219-Ra 0.009 [s] 7678 [keV]	219-Ra 0.009 [s] 7988 [keV]	216-Rn 4.5e-05 [s] 8050 [keV]	215-Rn 2.3e-06 [s] 8674 [keV]	212-Po 2.95e-07 [s] 10180 [keV]	212-Po* 2.99e-07 [s] 8785 [keV]
224-Th 1.04 [s] 7000 [keV]	14000	14170	14286	14298	14323	14450	14453	14678	14988	15050	15674	17180	15785
224-Th 1.04 [s] 7170 [keV]	14170	14340	14456	14468	14493	14620	14623	14848	15158	15220	15844	17350	15955
223-Th 0.6 [s] 7286 [keV]	14286	14456	14572	14584	14609	14736	14739	14964	15274	15336	15960	17466	16071
223-Th 0.6 [s] 7298 [keV]	14298	14468	14584	14596	14621	14748	14751	14976	15286	15348	15972	17478	16083
223-Th 0.6 [s] 7323 [keV]	14323	14493	14609	14621	14646	14773	14776	15001	15311	15373	15997	17503	16108
211-Po 0.5 [s] 7450 [keV]	14450	14620	14736	14748	14773	14900	14903	15128	15438	15500	16124	17630	16235
220-Ra 0.018 [s] 7453 [keV]	14453	14623	14739	14751	14776	14903	14906	15131	15441	15503	16127	17633	16238
219-Ra 0.009 [s] 7678 [keV]	14678	14848	14964	14976	15001	15128	15131	15356	15666	15728	16352	17858	16463
219-Ra 0.009 [s] 7988 [keV]	14988	15158	15274	15286	15311	15438	15441	15666	15976	16038	16662	18168	16773
216-Rn 4.5e-05 [s] 8050 [keV]	15050	15220	15336	15348	15373	15500	15503	15728	16038	16100	16724	18230	16835
215-Rn 2.3e-06 [s] 8674 [keV]	15674	15844	15960	15972	15997	16124	16127	16352	16662	16724	17348	18854	17459
212-Po 2.95e-07 [s] 10180 [keV]	17180	17350	17466	17478	17503	17630	17633	17858	18168	18230	18854	20360	18965
212-Po* 2.99e-07 [s] 8785 [keV]	15785	15955	16071	16083	16108	16235	16238	16463	16773	16835	17459	18965	17570

Figure 4.8: Sum energy matrix for the FRS $^{223-224}$Th settings. The sum matrix shows all foreseeable combinations of coincident alpha - decay energies detected by the α-TOF detector, represented by the summed energy of the two coincident alpha decays. The probabilities of these combinations, calculated as the normalized product of the intensity value of the coincident alpha - decay energies, are displayed with a color code as indicated by the colorbar. The highest-probability combinations (yellow and light green) align with the energy range of the investigated peak, while the lowest-probability combinations fall outside the relevant energy range. The ^{212}Po* is the only alpha decay line related to the internal source that has been taken into consideration, since the other lines have too low energies to compete with the coincidence events that populate the considered spectral range from 16-17 MeV in Fig. 4.6.

4.2 Alpha spectroscopy at the FRS-IC

In Section 4.1 the energy spectra acquired during the S530 experiment have been discussed. In that case the acquisition settings were made for the purpose of isotope identification and no alpha spectroscopy was performed.

In this section it is shown that alpha spectroscopy can be performed at the FRS-IC. This has been done during another experiment at the FRS-IC. Using the same acquisition setup made of a Si detector and a DAQ digitizer, as in the decay time measurement, it is possible to use it as a tagger for alpha decaying nuclides with half-lives ranging from few milliseconds up to few minutes providing the Q_α values of the decay events. In the experiment presented here, short-lived nuclides produced by ^{238}U projectile fragmentation at 1000 MeV/u were thermalized in the stopping cell and measured using a Si detector in DISTRICT. A silicon ion-implanted charged particle detector was used, manufactured by ORTEC from the ULTRA series with 100 μm depletion depth and 150 mm^2 active area (Ortec Ultra $BU - 016 - 150 - 100$ bakeable). The detector and its data acquisition (DAQ) system (CAEN DT5780SDM) are optimized to achieve optimum energy resolution, typically with a sigma between 30 to 60 keV. The silicon detector was calibrated using the ^{223}Rn decay chain from the internal source inside the CSC and alpha lines from the 3-line alpha source, both installed at DISTRICT. In order to determine the alpha energies of the projectile fragments, all peaks were fitted with Gaussians and exponentially modified Gaussians (HyperEMG) line shapes [130].

Fig. 4.9 shows the difference between the measured Q_α values from ^{238}U projectile fragments and previous literature values. The measured Q_α values reproduce well known literature values from specialized spectroscopy esperiments. Noteworthy is the measurement of ^{221}Ac, that in [122] was reported with large uncertainty. The energy of 7.778(10) MeV for the Q_α value of ^{221}Ac found in this experiment is within the error bars of the value provided by the literature [122], but 10 time more precise. Moreover, the value found in this experiment is in agreement with the findings of [131] where mass separated samples were used. Remarkably, the isotope ^{221}Ac has also been identified during experiment S530 in both mass spectra and energy spectra. The value reported in [131] agrees very well with the result of our measurement and confirms the reliability of the FRSIC experimental setup.

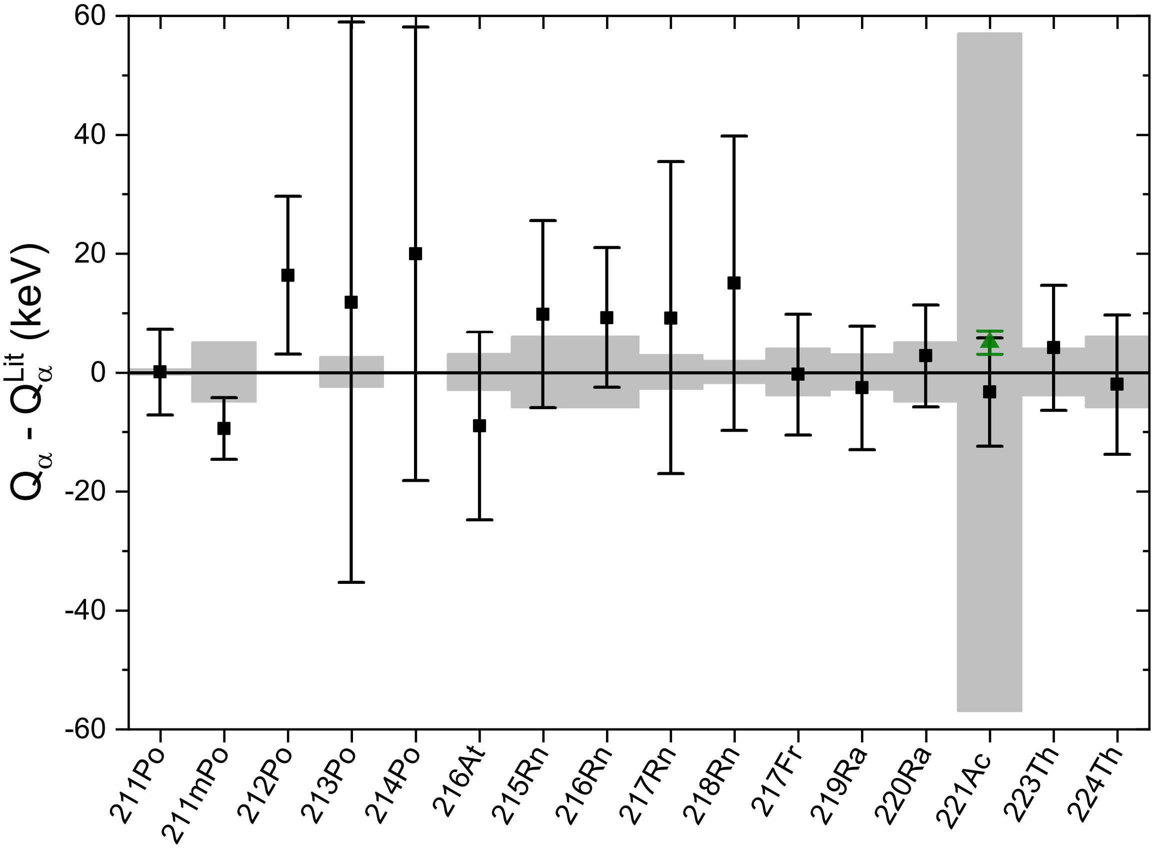

Figure 4.9: Q_α values of ^{238}U fragmentation products measured at the FRS Ion Catcher in comparison to their literature values, taken from [122]. The grey shaded area represents the uncertainty on the Q_α value accordingly to AME2020 taking into account previous measurements. An updated value for ^{221}Ac was recently reported in [131], indicated by the green data point [132]. The Q-value for this measurement is determined by measuring the alpha-particle energy (Q_α) and the gamma-ray energy (E_γ) in coincidence, ensuring accurate identification of decay processes. High-resolution detectors, such as Si(Li) and BEGe, significantly reducing uncertainties in Q-value calculations. For the ^{221}Ac two grey shaded areas are displayed, the smaller one takes into account how large the uncertainty would be if also the green measurement were taken into account.

4.3 Data analysis procedure for Time of Flight measurements

The time-of-flight (ToF) signal is acquired with the TDC 1 and TDC 2 modules as introduced in Sect. 3.4. In this section the focus is on the data acquisition using TDC 1 and the TOF Control software [123]. Subsequently, data are analyzed in a first step with the same software followed in a second step with a customized data analysis procedure written in the R language [133, 134, 135]. This second part is generated and constantly improved by the IONAS group at the University of Giessen. This section is dedicated to illustrate the data analysis procedure. Fig. 4.10 illustrates a flow chart of the data analysis procedure ultimately aiming at generating a mass value from the ToT data.

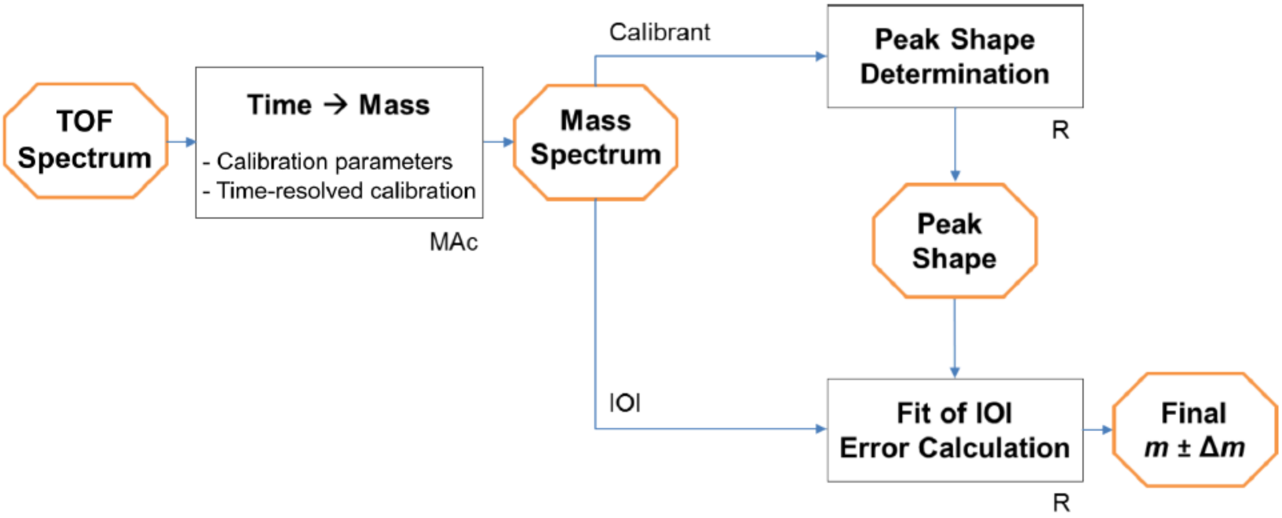

Figure 4.10: Flow chart of the data analysis procedure. The acquired ToF signal is plotted as a spectrum using the TOFControl software, before being calibrated and transformed into an m/q spectrum. The identified calibrant peaks in the spectrum are used to determine the peak shape used to fit the Ions of Interest (IOIs). Together with the error calculation, it is finally possible to derive a mass value for the Ions of Interest [136].

4.3.1 Calibration of a ToF spectrum

The time-of-flight (ToF) recorded is the time of flight t_{total} of the ions flying into the MR-TOF-MS from the injection trap to the detector (as visible in Fig. 4.11). It can be seen as the sum of the ToF from the injection trap to the detector without reflections in the analyzer, t_{tfs}, and the ToF for N_{it} reflections:

$$t_{\text{total}} = t_{\text{tfs}} + N_{\text{it}} \cdot t_{\text{it}}, \tag{4.1}$$

where N_{it} is the number of turns in the analyzer and t_{it} is the ToF per turn. The total flight path l_{total} is similarly given by:

$$l_{\text{total}} = l_{\text{tfs}} + N_{\text{it}} \cdot l_{\text{it}}, \tag{4.2}$$

where l_{tfs} is the path length from the injection trap to the detector, and l_{it} is the path length for a single turn in the analyzer. Due to the presence of the two reflecting electrostatic mirrors on both edges of the analyzer of the MRTOF it is possible to determine a relationship between the ToF and the mass-to-charge ratio (m/q) given by:

$$\frac{m}{q} = \frac{2U_{\text{eff}} \cdot t_{\text{total}}^2}{l_{\text{total}}^2}, \tag{4.3}$$

where m and q represent the ion mass and charge, respectively, and U_{eff} is the effective voltage accounting for the electric potential variation.

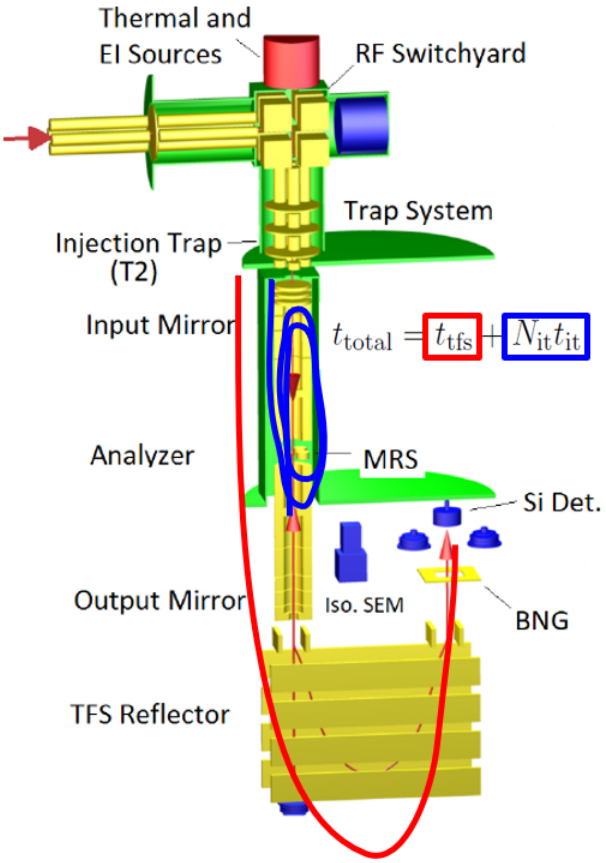

Figure 4.11: Schematic drawing of the MRTOF. The time-of-flight (ToF) recorded is the t_{total} flight time of the ions traversing the MR-TOF-MS from the injection trap to the detector. It can be seen as the sum of the ToF from the injection trap to the detector without reflections in the analyzer (red line), t_{tfs}, and the ToF for N_{it} reflections (blue line) where N_{it} is the number of turns in the analyzer and t_{it} is the ToF per turn. The total flight path l_{total} is the sum of the two contributions: $l_{\text{total}} = l_{\text{tfs}} + N_{\text{it}} \cdot l_{\text{it}}$ [119].

Based on this equation it is possible to convert the ToF signal into the mass - over - charge ratio. In practice, the experimentally recorded value of t_{total} is not exactly the theoretical one. Indeed, the measured time, t_{exp} includes an offset t_0 caused by cables and electronics:

$$t_{\text{exp}} = t_{\text{total}} + t_0. \tag{4.4}$$

Substituting Eqs. (4.1), (4.2) and (4.4) into Eq. (4.3), we obtain the equation to convert from the ToF signal into the experimentally determined value of m/q:

$$\frac{m}{q} = c \cdot (t_{\text{exp}} - t_0)^2 \left(1 + N_{\text{it}} \cdot b\right)^2 , \tag{4.5}$$

where $b = \frac{l_{\text{it}}}{l_{\text{tfs}}}$ and $c = \frac{2U_{\text{eff}}}{l_{\text{tfs}}^2}$.

The parameters c, t_0, and b of the mass-to-charge (m/q) calibration equation (Eq. (4.5)), are determined using calibrant ions. The t_0 parameter can be calculated either before or after the mass measurement of the ion of interest (IOI), provided that external cables from the analyzer to the acquisition system remain unchanged under experimental conditions. This calculation uses the ToF of at least two calibrant ion species measured without isochronous turns, in time-focus shift (TFS) mode (see Sect. 3.2).

Using the measured t_0 value, we perform an initial calibration step, referred to as the t_0 calibration. A second calibration step, called the multiturn calibration, is then carried out to determine the parameters b and c. This step requires identifying specific calibrant peaks in the spectrum.

The initial identification of these calibrant peaks involves comparing the relative number of events in peaks of the mass spectra that are supposed to belong to isotopic ions. The number of counts for each of these peaks taken into consideration is compared to the isotopic ratios of the isotopic ions we suspect to be. This identification can also be done observing the detection pattern over time in relation to the beam timing pattern. For instance, when a calibrant source has its m/q ratio within the MRS (mass range selector) setting, its peaks should appear as a continuous pattern of the ion current spectra (spectra where the number of ions detected is plotted as a function of time). In contrast, peaks of ions delivered by the FRS should follow the beam's timing structure. In our case, the beam had a spill structure of 3 ms ON and 2 ms OFF. In the present work are found peaks from Xe, Cd isotopes, from C_3F_8 and ^{133}Cs. The C_3F_8 and Xe gas are injected in a controlled way on the top of the MRTOF for calibration purposes during the experiment. The Cs comes from a thermal source mounted on the top of the MRTOF.

Table 4.4 lists the expected and actual counts for the calibration lines (within the mass range relevant to our data acquisition) from the C_3F_8 gas.

Once the identification of at least two peaks is done, a fit of the known peaks has to be performed using Eq. (4.5) to determine the parameters b and c and then convert the whole spectrum.

Since the spectra exhibit ToF fluctuations due to shifts in the analyzer's reflector potentials and thermal expansion, the peaks can be broader than the expected resolving power. These

Calibrant peak	**Mass**	**Probability(%)**	**Expected counts**	**Real Counts**
$^{12}C_2{}^{19}F_4$	99.9936	100	97263	97263
$^{12}C_1{}^{13}C_1{}^{19}F_4$	100.997	2.16	2101	2337
$^{13}C_2{}^{19}F_4$	102	0.01	10	17
$^{12}C_2{}^{19}F_5$	118.992	100	38634	38634
$^{12}C_1{}^{13}C_1{}^{19}F_5$	119.995	2.16	835	1059
$^{13}C_2{}^{19}F_5$	120.999	0.01	4	8
$^{12}C_2{}^{16}O_1{}^{19}F_3$	96.9901	100	6385	6385
$^{12}C_1{}^{13}C_1{}^{16}O_1{}^{19}F_3$	97.9935	2.2	141	156
$^{12}C_2{}^{18}O_1{}^{19}F_3$	98.9945	0.22	14	65

Table 4.4: The table lists the mass, the probability, the number of expected and experimentally registered counts for the possible (for the mass range of interest in our data acquisition) calibration lines from the C_3F_8 gas bottle installed by the time of the experiment for calibration purpose.

fluctuations are corrected with a time-resolved mass calibration (TRC) applied to the mass-to-charge spectrum. To perform the TRC, the acquired spectrum, which in our case is the sum of many spectra, is divided in groups of a certain number of spectra (typically covering the time of a beam spill) and for each group the parameter b is determined. A linear interpolation is then applied across the b values found for each group and the result of the interpolation is taken as final b value for the spectrum calibration. An example of the TRC correction is shown in the Fig. 4.12. The TRC correction is applied to one of data files obtaining during the S530 experiment. The picture illustrates how the mass resolving power of the peak (in this case ^{133}Cs^{+}) improves from the situation before (case A) and after (case B) applying the TRC. In the first case the mass resolving power is 40000, which in the second improved case it reaches 120000.

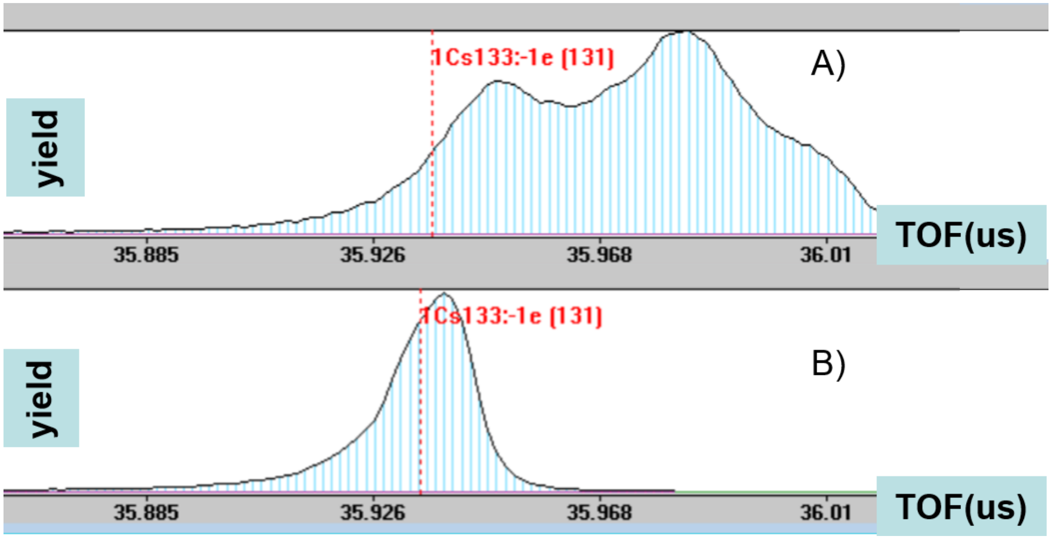

Figure 4.12: TRC calibration result for the ^{133}Cs^{+} peak. The plot shows the TOF spectrum for the mass ^{133}Cs^{+} peak before (case A) and after (case B) the TRC calibration. In the first case the resolving power is 40000, in the second improved case it reaches 120000.

4.3.2 Identification of Ions of Interest (IOI)

Based on the mass-to-charge ratio, peaks in the m/q spectra are identified. This identification is confirmed via several criteria:

- Comparing the detected rates with theoretical expectations or to results of other experimental methods (e.g., α spectroscopy, particle identification in flight with FRS detectors).
- Consistency of the identification across measurements with different MRS settings, where an ion of interest (IOI) exits the analyzer after a different number of turns compared to those made by the same ion in another configuration.
- in the case of an ion beam that possesses a spill structure, it is possible to compare the spectra for the time when the beam is ON to another time when the beam is OFF. In such a way it is possible to discard peaks that may appear in the mass region where we expect the IOI, but which are not related to the beam but rather originate from calibrants, background or impurities inside the FRS-IC.

Fig. 4.13 shows an example of IOI identifications for ^{220}AcOH and ^{221}AcOH by looking at the correlation with the beam spill ON and OFF. The same two peaks shown in the figure have also been found in two files with different MRS windows appearing at different turn numbers.

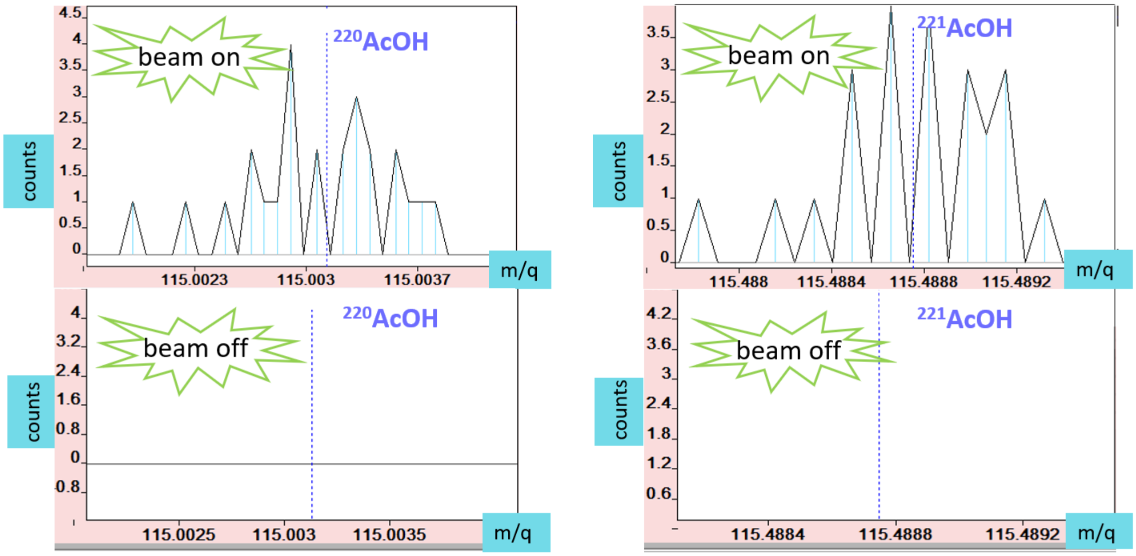

Figure 4.13: IOI identifications for ^{220}AcOH and ^{221}AcOH by looking at the correlation with the beam spill. When the beam is ON the peaks appear in the spectrum, while they do not appear when the beam is OFF. The same two peaks shown in the picture have also been found in two files with different MRS windows appearing at different turn numbers. These two observations confirm the identification of ^{220}AcOH and ^{221}AcOH.

4.3.3 Determination of the Peak-Shape Parameters

After the calibration and the IOI identification the next step is to obtain a peak shape to fit the identified IOI. The mass resolving power of TOF mass spectrometers is generally mass-independent, so peak shapes are consistent for ions of the same charge state. To determine a peak shape valid for the IOI, high-statistics calibrant ion is chosen, measured simultaneously with the IOI and possibly having same charge state and turn number.

In cases when statistical processes dominate the probability distribution, a peak measured with the MRTOF can be simply described by pure Gaussian functions. However, in high-resolution measurements, where the phase-space of the trapped ions has been strongly reduced by experimental methods, the contributions of image aberrations, field imperfections need to be included. Contributions of higher-multipole components and mechanical misalignments are clearly observed in the tails of the distribution and thus require non-Gaussian analysis methods. therefore the calibrant peak is fitted with a hyper-Exponentially Modified Gaussian (hyper-EMG function) [137], i.e., a Gaussian distribution convoluted with multiple exponential functions with different weights at one or both sides. Fig. 4.14 is an example of the peakshape determination resulting from the Hyper-EMG fit function applied to the calibrant peak $^{12}C_2{}^{19}F_5$. The plot shows the count number as a function of the mass-to-charge ratio, on top in linear scale and in the bottom panel in logaritmic scale. In black the data points, in yellow the initialization function and in red the final fit function are included.

For the fit, the data is binned according to Freedman-Diaconis rule [138] and fitted by a least squares (LS) method and validated in a reduced χ^2 test and with a Kolmogorov–Smirnov (KS) test [139]. Once the parameters of the hyper-EMG are determined, the calibrant data is fitted by a weighted maximum likelihood estimation (wMLE) method [140] to unify fitting methods used in the treatment of calibrant ions and IOI data. At this point the peak-shape parameters calculated from the calibrant distribution are scaled to the IOI. The scaling factor takes into account the general increase of the peak width with increasing mass-to-charge ratio and mass resolving power differences

$$S = \frac{\left(\frac{m}{q}\right)_{\mathrm{IOI}}}{\left(\frac{m}{q}\right)_{\mathrm{cal}}} \cdot \frac{\left(\Delta\frac{m}{q}\right)_{\mathrm{cal}}}{\left(\Delta\frac{m}{q}\right)_{\mathrm{IOI}}}, \tag{4.6}$$

where $\left(\frac{m}{q}\right)_{\mathrm{IOI,cal}}$ are the IOI and calibrant mass-to-charge ratios, and $\Delta\left(\frac{m}{q}\right)_{\mathrm{IOI,cal}}$ are their resolving powers.

4.3.4 Precise calibration and Final Mass-to-Charge Value

Up to this step in the data-analysis process, the mass-to-charge scale has been established during the calibrations of the spectra by the three steps: by the t_0 and multiturn calibration plus a Gaussian fit in the TRC correction. Therefore, the wMLE fit must be applied to

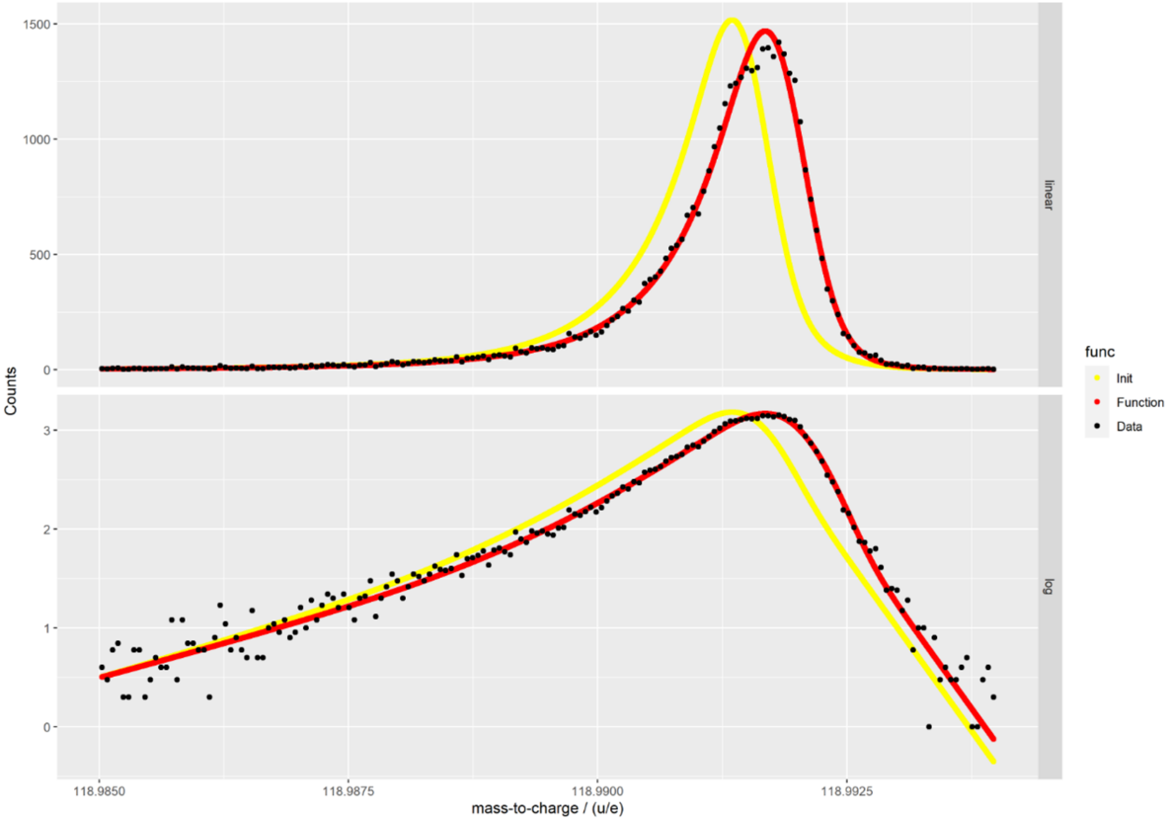

Figure 4.14: An example of the peak shape determination resulting by the Hyper-EMG fit function applied to the calibrant peak $^{12}C_2{}^{19}F_5$. The plot shows the counts number as function of the mass-to-charge ratio, on top in linear scale on the bottom in logaritmic scale. In black are shown the data points, yellow marks the initialization function and in red the final fit function is displayed.

both the IOI and calibrant ion to obtain the final mass-to-charge value and associated uncertainty. This step is called the precise calibration.

The final mass-to-charge value of the IOI is obtained from the wMLE-fitted values of the IOI, $(m/q)_{\mathrm{IOI,wMLE}}$, the calibrant ion, $(m/q)_{\mathrm{cal,wMLE}}$, and the calibrant's literature mass-to-charge value, $(m/q)_{\mathrm{cal,lit}}$, accordingly to:

$$\left(\frac{m}{q}\right)_{\mathrm{IOI}} = \frac{\left(\frac{m}{q}\right)_{\mathrm{IOI,wMLE}}}{\left(\frac{m}{q}\right)_{\mathrm{cal,wMLE}}} \left(\frac{m}{q}\right)_{\mathrm{cal,lit}} . \tag{4.7}$$

4.3.5 Uncertainty of the mass value

The uncertainty of the mass value is calculated by adding in quadrature individual components. A comprehensive list of uncertainty components and their definitions can be found in [133]. The components relevant for this work are statistical uncertainties with contaminations (the statistical uncertainties include multiple incertainty contributions, statistical contribution error and the contamination contribution error give the largest contribution to the statistical uncertainties) of IOI that accounts for about 80% of the total error and calibrant peakshape uncertainties that accounts for about 15% of the total error.

Since there is no analytical solution available for the wMLE fit of a Hyper-EMG, an empirical approach has been applied to determine the statistical uncertainty. Random numbers are drawn (same number of events as measured) according to the distribution function determined for the calibrant and IOI and are fitted with the wMLE function. This is repeated many times (typically 100 times). The standard deviation of the mass to charge value obtained from this procedure is the statistical uncertainty of the calibration peak and the IOI. The contamination uncertainty is due to unknown unresolved peaks (contaminants) such that the peak of the IOI might contain events from contaminant ions. To estimate their influence on (m/q) for the IOI, synthetic data are generated containing two peaks which represent IOI and potential contaminants. The contaminant peak is moved over the IOI peak, and for each position a shift in (m/q)_IOI is calculated with a respective KS test. The corresponding uncertainty is defined as the strongest shift multiplied by the result of the respective KS test. The peak-shape uncertainty is calculated in this way: each parameter of the Hyper-EMG function is altered by its individual uncertainty while keeping the others constant, and the peak is fitted again with the wMLE method. A deviation in the obtained m/q value is calculated for the peak-shape calibrant and the IOI. The deviations calculated for all parameters are added in quadrature to obtain the peakshape uncertainty.

4.3.6 Final atomic mass of the IOI

The IOI reaches the detector as an ion typically in single or doubly charged state, but the final mass we want is the one in atomic neutral form. In this case, the atomic mass of the IOI, denoted as m_{IOI}, along with its uncertainty σ_{IOI}, is calculated as follows:

$$m_{\text{IOI}} = \left(\frac{m}{q}\right)_{\text{IOI}} \cdot q_{\text{IOI}} + m_e \cdot \frac{q_{\text{IOI}}}{e}, \tag{4.8}$$

$$\sigma_{\text{IOI}} = \sigma_{\text{IOI,ionic}} \cdot q_{\text{IOI}}, \tag{4.9}$$

where $\left(\frac{m}{q}\right)_{\text{IOI}}$ and $\sigma_{\text{IOI,ionic}}$ represent the mass-to-charge ratio and its uncertainty as determined in the previous analysis. Here, q_{IOI}/e indicates the charge state of the IOI, and m_e is the mass of an electron. Since for the measurement typically singly- or doubly-charged ions are considered, the electron binding energy, which is on the order of a few eV, can be neglected.

In Fig. 4.15 the m/q ratios of the actinide IOIs $^{223-224}$Th, $^{220-221}$Ac, $^{234-235}$U are displayed in the molecular forms as they are detected. They have been fitted using the procedure illustrated so far. The red line is the fit curve, in black the experimental data are included.

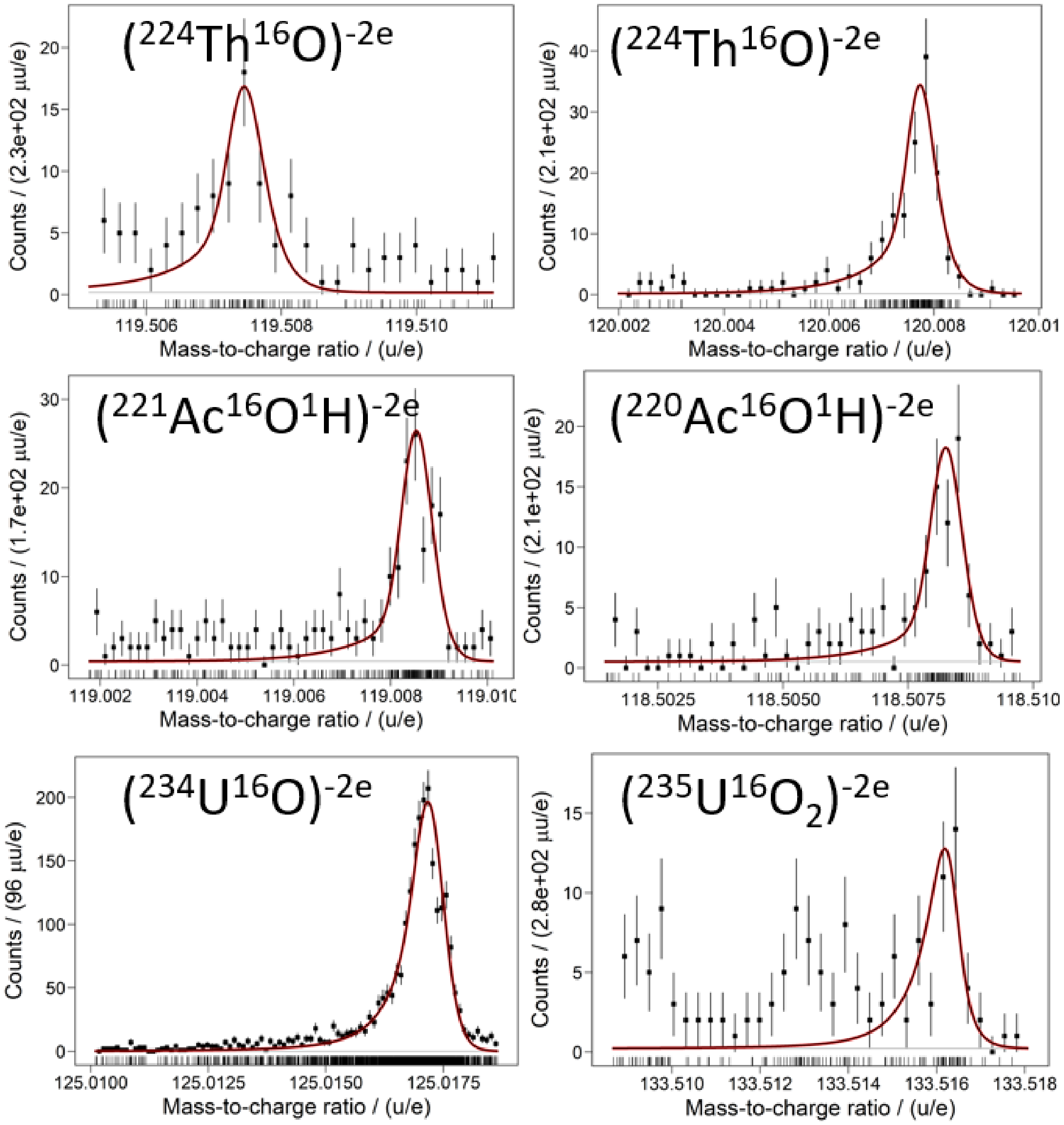

Figure 4.15: MRTOF mass peaks of molecular ions registered for Ac, Th and U isotopes at the FRS-Ion Catcher facility within the S530 experiment. The red line is the fit curve, in black the experimental data are included.

The final results from the fit of the mass distribution peaks in Fig, 4.15 are reported in Table 4.5.

Nuclide	ΔME (keV/c^2)	ME$_{\text{FRS-IC}}$ (keV/c^2)	ME$_{\text{lit}}$ (keV/c^2)[122]
^{220}Ac	-131.8 ± 170.4	13875.8 ± 170	13744 ± 6
^{221}Ac	45.1 ± 141.5	14484.5 ± 128.1	14530 ± 60
^{224}Th	101.5 ± 238.4	19894.5 ± 238.2	19996 ± 10
^{223}Th	9.6 ± 203.9	19375.4 ± 203.8	19385 ± 8
^{234}U	6.4 ± 99.2	38138.6 ± 99.2	38145.0 ± 1.1
^{235}U	-68.0 ± 185.2	40986.8 ± 185.2	40918.8 ± 1.1

Table 4.5: Mass excess of actinide isotopes as derived from MRTOF data acquired in experiment S530. The difference between ΔME between literature values and experimental data is listed.

As shown in Tab. 4.5, the experimental uncertainties of this work range from 2 to 200 times larger than those of the literature values, which are averages of known measurements. Consequently, the results from the S530 experiment do not provide competitive insights and do not significantly add to the existing mass spectrometry data. However, it is worth noting that direct measurements for isotopes like ^{220}Ac and ^{221}Ac had not been conducted prior to this work. Thus, it is important to emphasize that future measurements of these isotopes, with half-lives shorter than 50 ms, can be performed at FRS-IC and improved in similar experiments.

4.4 Time over Threshold data acquisition

The TDC 2 of the acquisition setup was set with threshold values of 0.9 V, 1.5 V and 0.02 V, respectively, for the signal amplitudes at channels 1, 2 and 3, where the first two received the ToF signal, while the third one registered the energy signal. At TDC channel 6 the start time signal was recorded as relative time in each sweep. Channels 1 and 2 were triggered only by the rising signal edge, while channel 3 recorded both rising and falling signal edges. Listmode data were written in hexadecimal format that need to be translated first in to a binary format and then, depending on the assigned number of bins for each measured parameter (sweep number, time, edge type, channel number), converted to a decimal representation. The bin assignment is chosen by the experimenter during the setup of the electronics and is limited by the resolution of the electronics itself. The time converted into decimals is given in channel units, it needs to be multiplied by the granularity of the TDC of 0.8 ns, representing the maximum resolution of the TDC in use.

The reason for these settings is motivated by the idea of implementing a new method specifically designed to identify fission fragment events from all acquired events. The mass measurement technique is a well established method to unveil nuclear isomers with the MR-TOF as explained in Sect. 4.3. Nevertheless, cases are conceivable where, due to the low cross section of the fission decay compared to the competing alpha decay (as for example in the case of ^{235}U, where the alpha decay has a 100% branching ratio, while the spontaneous fission branch only occurs in 7×10^{-9} of all events), only few counts can be acquired for a certain isomeric state during the whole beamtime. This makes it very challenging to validate the measurement of the isomeric state from a statistical point of view. Spontaneous fission decay differs considerably from alpha decay in terms of the decay energy. Using this information, the acquired time-over-threshold data could be used as a convenient method to identify spontaneous fission decay events. ToF signals recorded at channels 1 and 2 at different thresholds are used to remove noise and background from the energy data recorded at channel 3. The rising and falling signal edges recorded at channel 3 allow to measure the width of the acquired energy signal and to discriminate the alpha decay data from spontaneous fission events. Identified fission events can then be matched with the data from the same event as acquired with TDC channels 1 and 2 via the acquisition time stamp. Since the signals fed to channel 1 and 2 of the TDC 2 are copies of the signal sent to TDC 1, one can now better identify the few fission events in the mass spectra. To validate this new method, it was reproduced in an offline test.

4.5 Time over Threshold offline measurements with ^{252}Cf source

This section presents data from an offline measurement with a ^{252}Cf fission (and alpha) source, dedicated to validate the Time - over - Threshold method that uses the TDC data to discriminate fission fragments from alphas. This offline measurement uses a MagneTOF detector and a ^{252}Cf source with an activity of about 2.5 kBq. A ^{252}Cf source is a good choice since it decays through both α decay (97%) and fission (3%). The simplified laboratory setup consists of a ^{252}Cf source placed at a distance of approximately 10 cm facing a MagneTOF detector in high-vacuum of $4 \cdot 10^{-7}$ mbar, measured with an ionization gauge, which was turned off during data measurements. The detector has an acceptance aperture of 15×33 mm^2, and a collimator with 1 cm in diameter is positioned between the detector and the source. Fig. 4.16 shows the experimental setup, with the vacuum pump mounted on top of a vaccuum chamber and the ^{252}Cf source installed on the top of the support piece visible from the open front part of the T flange and placed at a distance of circa 10 cm facing a MagneTOF detector. In between the source and the detector is positioned the collimator.

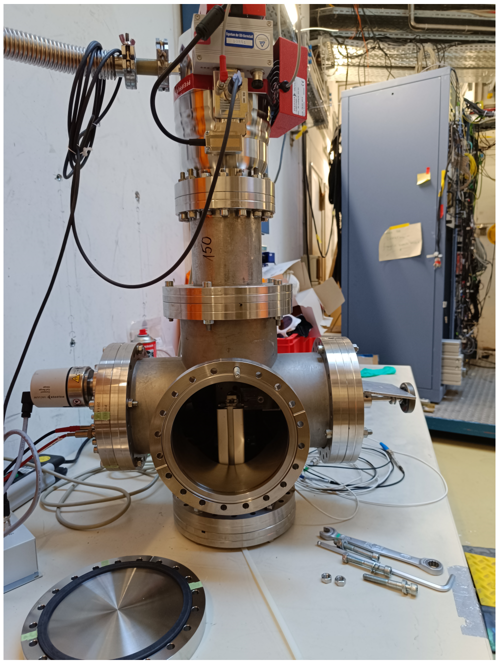

Figure 4.16: Experimental setup for time-over-threshold offline measurement. It consists of a vaccuum chamber where a vacuum pump is mounted on top of it providing high-vacuum conditions of $4 \cdot 10^{-7}$ mbar. Inside a ^{252}Cf source is installed on the top of the support piece visible from the open front part of the chamber and placed at a distance of circa 10 cm facing a MagneTOF detector. In between the source and the detector is positioned a collimator with 1 cm in diameter.

In order to estimate the count rate ratio of α particles to fission fragments, the branching ratio of the decay of ^{252}Cf is taken as reference. ^{252}Cf decays in 96.9% via α - decay and with 3.1% via spontaneous fission. Considering isotropic emission, only about 50% of the alpha particles will be directed towards the detector, while, for each spontaneous fission event two fragments emerge, one of them going in the direction of the detector. This results in an expected count rate at the MagneTOF detector between α - decay and fission of about 15.6 counts per seconds.

4.5.1 Experimental settings

A preliminary analysis had to be performed in order to find the operational point for the applied voltage to the MagneTOF's external grid, as well as the threshold voltage used in order to filter out background from the detection signals.

For this purpose, an MCS6A multiple-event time digitizer with 0.8 ns time resolution (the same was used during the beam time) was used in order to evaluate the measured count rate of decay events as a function of the previously mentioned parameters. A two minutes measuring interval was used for each couple of parameters. The results are plotted in Fig. 4.17, where the count rate is displayed as a function of the applied voltage for multiple settings of the threshold voltage.

Considering the activity of our source and the solid angle with the detector, we expect about 0.36 counts per second. Based on this expectation, an operating point was chosen in the plateau region around 2.2 kV of the applied grid voltage. The value finally selected for the MagneTOF's outer grid potential was 2.15 kV, while -25 mV were chosen as the threshold voltage.

4.5.2 Time-over-Threshold Analysis

For this laboratory measurement instead of using the msca6 TDC, as during the S530 experiment, an HDO4024A-MS oscilloscope was used with an eight times better time resolution. The data were acquired by automatically saving display snapshots for every time a trigger level of -10 mV was reached.

An offline analysis was performed with a script developed for peak finding and characterization. For each identified peak, the ToT was recorded, as well as the amplitude and the integral. By plotting the correlation and histogram plots for these three quantities, the presence of two distinct zones is already evident without any data processing, as illustrated in Fig. 4.18 where the count rate is plotted as function of ToT. A cut at 3 μs applied to the ToT data in Fig. 4.18 clearly separates α particles from fission fragments. From the acquired counts in these two regions of 94222 and 450, respectively, for alphas and FFs, the count rate ratio is 20.9, slightly higher than the expected value of 15.6.

In order to further investigate the previous results, the same analysis was performed by exchanging the ^{252}Cf source against a triple-α source. This source is composed of ^{239}Pu, ^{241}Am and ^{244}Cm, all 100% α emitters. ^{239}Pu has a 3×10^{-10} probability for spontaneous fission decay, while this branch for ^{241}Am and ^{244}Cm, respectively, accounts to 3.6×10^{-10}

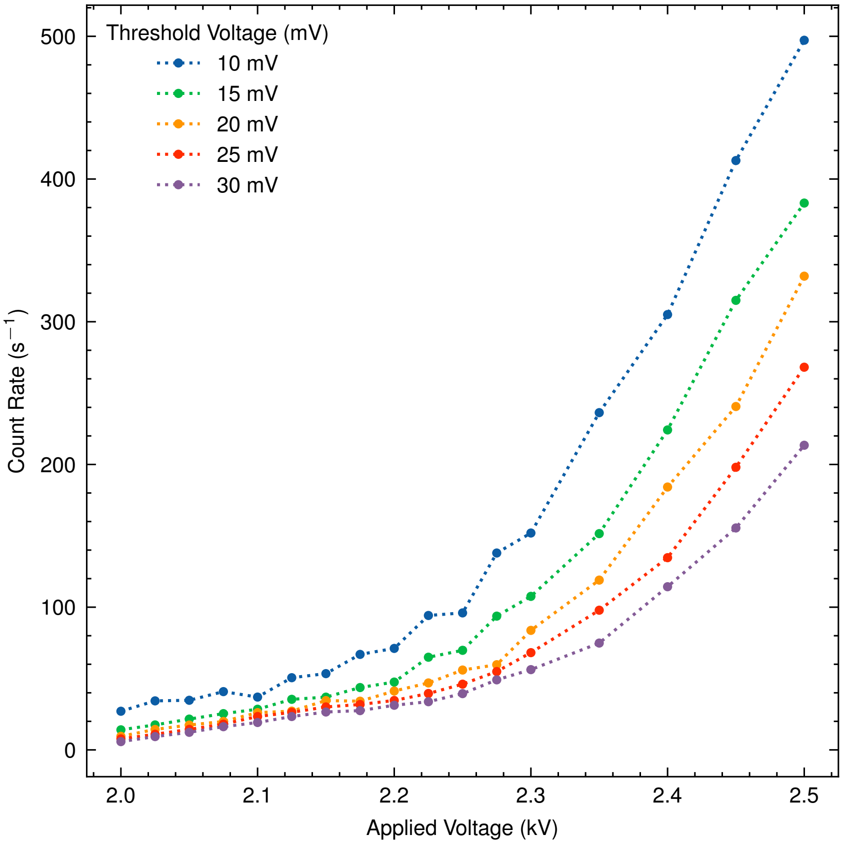

Figure 4.17: Measured count rate as a function of the voltage applied to the outer grid of the MagneTOF detector for different settings of the measurement's absolute threshold voltage.

and 1.4×10^{-4}. Hence spontaneous fission can be neglected and only α decay events are expected from the triple-α source.

The results of the measurements with the triple-α source and the ^{252}Cf source are presented in Fig. 4.19. In the case of ToT events for the triple-α source only values are found below 3 ns, as expected, since only α decay events should be detected.

Furthermore, looking at Fig. 4.19, it is possible to see that the peak associated to α particles is shifted and more widespread for the triple α source. This can be readily explained by the different α particle emission energies for both sources. As reference the α decay energies are listed in Tab. 4.6. The isotopes present in the triple α source span an energy range from 5.1 MeV to 5.8 MeV, while in the case of the ^{252}Cf source the alpha decays have energies in a smaller interval from about 5.8 MeV to 6.1 MeV. This explains the large spread of the alpha distribution in the case of the triple α source compared to ^{252}Cf.

The offline measurement presented here demonstrates that the Time-Over-Threshold (ToT) method, applied to the energy signal, is a reliable approach for identifying fission

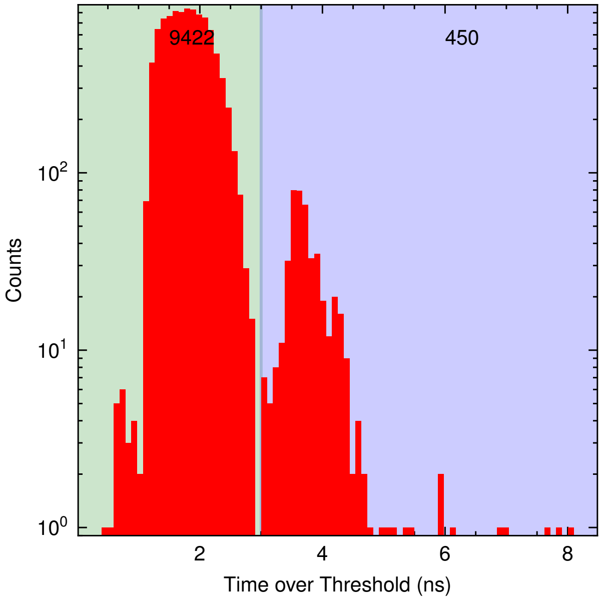

Figure 4.18: Time-over-Threshold histogram for the decay products of a ^{252}Cf source. The green zone contains α decay events, while the blue area confines the fission events.

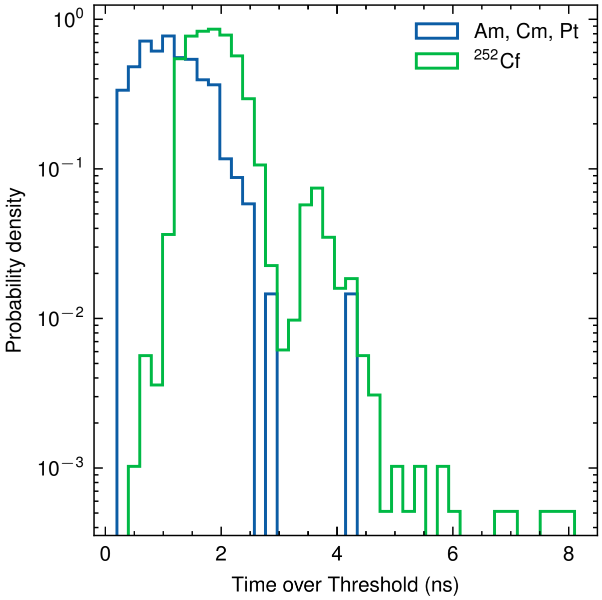

Figure 4.19: Time-over-Threshold histogram for both ^{252}Cf and triple α sources.

fragment events among all acquired events. This method shows promise for future applications as a preliminary tool to distinguish fission fragments and as a complementary technique to support mass measurements. This is particularly valuable in scenarios where the low cross-section of fission decay, relative to competing alpha decay, makes identifying

Table 4.6: α particle emission energies for isotopes of a triple - α - source compared to ^{252}Cf.

Isotope	Energy (MeV)	Intensity (%)
^{239}Pu	5.105	11.5
	5.143	15.1
	5.155	73.4
^{241}Am	5.388	1.4
	5.433	12.8
	5.486	85.2
^{244}Cm	5.763	23.3
	5.805	76.7
^{252}Cf	6.076	14.5
	5.805	76.7

fission fragments in the mass spectra challenging. By enabling a clear distinction of fission events, the ToT method establishes a new tool for advancing studies on fission isomers.

Unfortunately, due to a misalignment in the MRTOF, as detailed in the following chapter, this method could not be employed to distinguish any potential fission isomeric events of ^{235}U from its ground state. The peaks identified in the mass measurements exhibit significant distortion, making it impossible to model them with a single peak shape. This prevents the identification of an isomeric contribution beneath the large peak. [Note after submission: The MRS settings were automatically switched between two configurations, each for such a short time that the electronics inside the MR-TOF never reached a stable state. As a result, the system operated continuously under random/unstable conditions.]

Even if an isomeric peak were present and distinct from the ground state peak, it would remain undetectable due to the significant background noise in the mass spectrum, which masks low-intensity signals or sparse counts. As a result, applying the discussed method to disentangle fission decays from other processes using Time-over-Threshold (ToT) data is futile since no reliable mass measurement of the isomeric state can be performed.

Furthermore, the ToT data themselves are heavily impacted by noise due to the high background levels, making it impractical even to test the method for curiosity. Online measurements, where the incoming count rate is four orders of magnitude higher than in offline measurements, exacerbate this issue, further limiting the method's applicability.

4.6 Data analysis of the half-life for ^{240f}Am and ^{242f}Am

In the commissioning of experiment I290 in Jyväskylä an acquisition system for acquisition of the energy spectra was implemented following the idea developed during the S530 experiment. This time the gain settings have been expanded to allow the detection of fission fragments and a new updated software and hardware DAQ Compass was used. The decay events from the reaction products of fusion-evaporation reactions induced by deuterons from the K130 cyclotron impinging on a ^{242}Pu target, were recorded. These data were acquired with the CAEN digitizer DT5724 in a text format where, for each event, are recorded the channel to which the signal belongs, the time, the energy in channel units and an extra flag (the latter means that for each event is associated a number that tells us if the acquisition of that event had any issue and if so what was the origin of the issue). Since fission decays are expected to have energies above 100 MeV, while alpha decays used for the selection of the beam fragment are expected up to about 8 MeV, fission events could be easily recognized by inspecting the energy spectra of the decay events. The fission events should exhibit a double peak distribution, very well separated from the alpha decay energy. An example of such an energy spectrum is shown in Fig. 4.20.

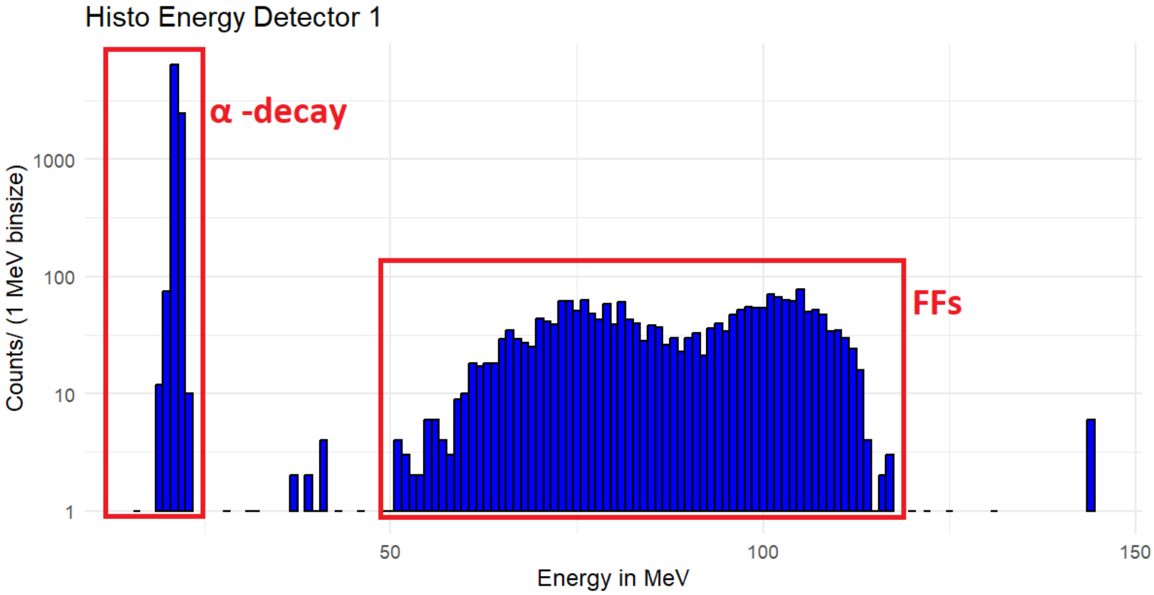

Figure 4.20: Histogram of the energies acquired during the I290 experiment. The histogram shows the energy spectrum of decay events seen by the Si detector 1. Fission events (FFs) are easily identified as those belonging to the slightly asymmetric double-humped distribution at high energies. The energy of the fragments post neutron emission is calibrated using a ^{252}Cf source.

In order to plot and fit the decay time of the fission events we have to gate also on the signal at channel 4 (the kicker signal). The kicker signal is a rectangular logic signal, it is ON when the beam is sent to the Si detectors, and OFF when the beam goes downstream to the MRTOF. The ON/OFF signal relates to an event at channel 4 having as energy 0 or a high number (typically in these data around 5000 channels), the time between ON and OFF events is the time the beam stays oriented towards the Si detector and is the accumulation time of the ions implanted on the Si detector. The time between the OFF and ON events is the time when the beam stays oriented towards the MRTOF, this means no beam reaches the Si detector, so this time interval defines a time window when only decay events are detected from the implantation of ions on the Si detector surface. Therefore one can measure the decay time of accumulated ions within this time window. At this point the second and last gate applied on the events affects only those decaying in the OFF-ON time window. Due to the fact that the Si detectors are far from the production site and that in our case the fission events of interest have decay times in the order of ms, plus the mass separation done via the dipole magnet, it is assumed that the beam is only transporting the isomers for which we want to measure the decay time: ^{242f}Am or ^{240f}Am. The decay time is determined via a linear fit to the decay events plotted in a logarithmic scale. The fit function is $log(N(t)) = b \times t + c$ where N(t) is the number of decay events at time t, t is the time in ms. From the fit the parameters b and c are extracted and from the b value the half-life $\mathrm{T}_{\frac{1}{2}}$ can be derived as $T_{\frac{1}{2}} = \frac{log(2)}{b}$. The linear fit for the ^{242f}Am and ^{240f}Am decay time are shown in Figs. 4.22 and 4.21, respectively.

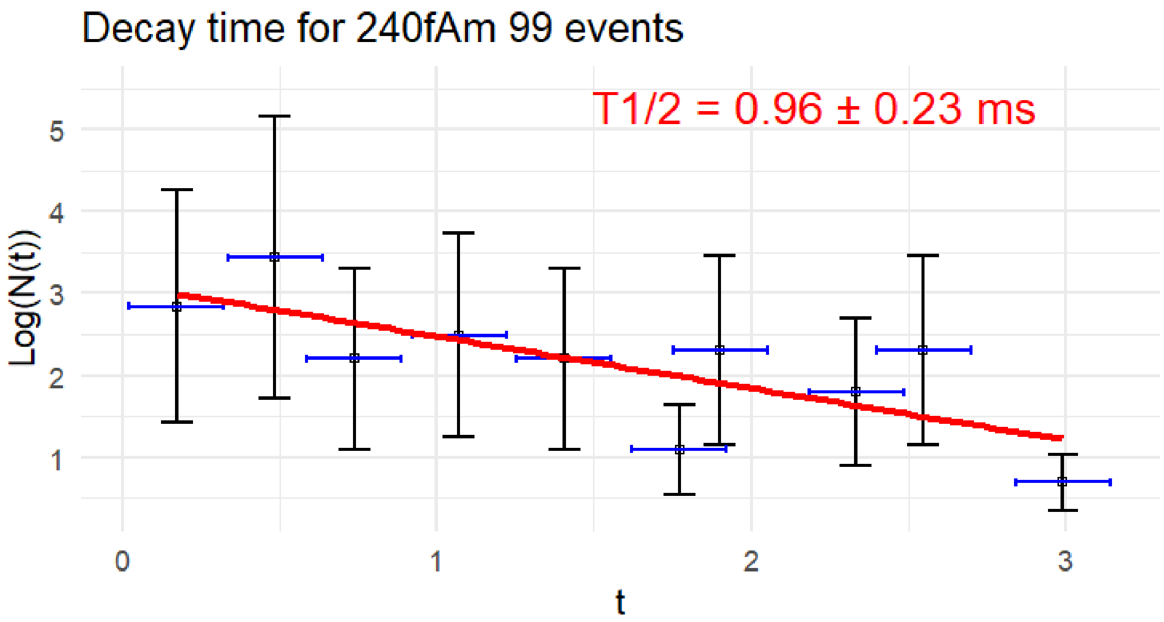

Figure 4.21: The linear fit for the ^{240f}Am decay time. The decay time is extrapolated via a linear fit to the decay events plotted in a logarithmic scale. The fit function is $log(N(t)) = bt + c$ where N(t) is the number of decay events at time t, t is the time in ms. From the fit the parameter b and c are obtained and from the b value the half-life T$_{\frac{1}{2}}$ can be derived as $T_{\frac{1}{2}} = \frac{log(2)}{b}$. The fit is made over 99 events and the half-life resulting from the fit is $T_{\frac{1}{2}} = 0.96 \pm 0.23$ ms.

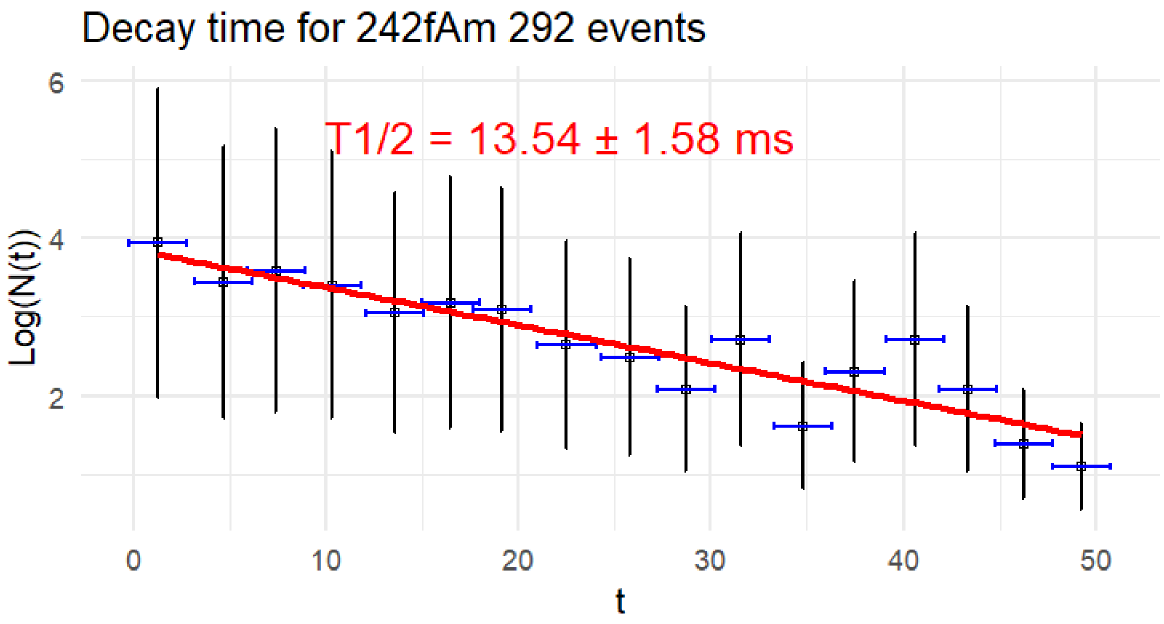

Figure 4.22: The linear fit for the ^{242f}Am decay time. The decay time is determined via a linear fit to the decay events plotted in a logarithmic scale. The fit function is $log(N(t)) = bt + c$ where N(t) is the number of decay events at time t, t is the time in ms. From the fit the parameter b and c are obtained and from the b value the half-life T$_{\frac{1}{2}}$ can be derived as $T_{\frac{1}{2}} = \frac{log(2)}{b}$. The fit is made over 292 events and the half-life resulting from the fit is $T_{\frac{1}{2}} = 13.54 \pm 1.58$ ms.

The results achieved for the fission isomer half-lives for ^{240f}Am and ^{242f}Am are in agreement with the literature values. Literature and experiment values are listed in Table 4.7.

Isomer	$\mathbf{T}_{1/2}^{exp}$	$\mathbf{T}_{1/2}^{lit}$ **[141]**
^{240f}Am	0.96 ± 0.23	0.94 ± 0.04
^{242f}Am	13.5 ± 1.6	14.0 ± 1.0

Table 4.7: Half-lives of ^{240f}Am and ^{242f}Am. In the table the experimental half-life and the literature values are compared [141].

Chapter 5

Discussion of results

5.1 Assessment of rate capability achieved with the FRS-IC

The introduction of the short DC cage for the S530 experiment has allowed for a rate capability of circa 1 order of magnitude higher then before, achieved with beam.

The normalized extraction efficiency as a function of the incident beam rate is shown in Fig. 5.1, compared to previous results with the long DC cage and simulations. It was calculated as the ratio of $^{235}\mathrm{UO}_2^+$ ions measured by the MR-TOF-MS relative to incident ions detected by a plastic scintillator, installed before the CSC, and corrected for the duty cycle of the MRTOF and dead-time effects. To account for stopping and transport losses, efficiencies were normalized to a beam rate of $2.2 \cdot 10^3$ ions/s, where space-charge effects are negligible, assuming full extraction efficiency.

In Fig. 5.1 the red diamonds stand for this work, the (open) squares represent the simulations, the (filled) squares [107] and circles [109] are previous experimental data with the long DC cage installed.

As we can observe from Fig. 5.1, in the case of this work the rate capability is higher than in all other cases and no loss of extraction efficiency at rates of the incident beam up to 2×10^5 ions/s can be observed. Higher beam intensities could not be tested as the radiation limit of the experimental area was reached. The result achieved in terms of higher rate capability reached is due to the following details:

- A higher number of the DC-electrode rings - over - length ratio reduces the near-field distortions and allows efficient transporting of the ions stopped closer to the electrodes

- The diameter of the new DC cage is larger, this enlarges the stopping volume in the radial direction

- Higher DC push fields have been used and this reduces the time for removing the He ion-electron pairs

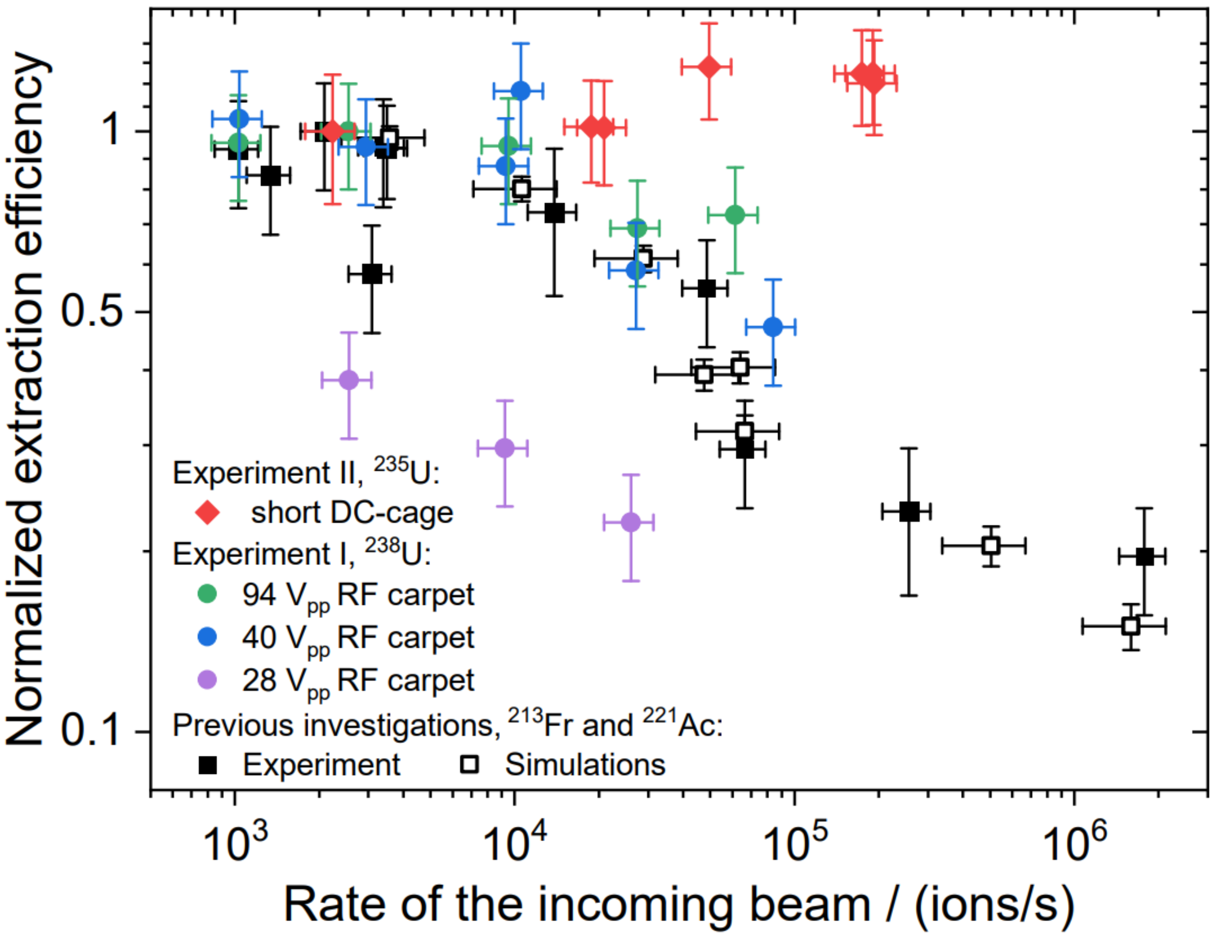

Figure 5.1: The normalized extraction efficiency is displayed as a function of the rate of the incident beam [142]. Red diamonds stand for this work, the (open) squares represents the simulations, the (filled) squares [107] and circles [109] are the previous experimental data with the long DC cage installed.

- The shorter length of the DC cage reduces the impact of space charges on the ion extraction.

Another promising expect related to the installation of the short DC cage is the possibility to reduce the extraction time to 10 ms. The isotopic identification of ^{220}Ac demonstrates an extraction time of at least its half-life (26.2 ms). An additional dataset acquired during the S530 experiment shows encouraging indications of the extraction of shorter-lived species. However, these results are statistically weak and require further validation. A definitive experimental demonstration will rely on future studies with improved statistics and optimized methodologies.

5.2 Mass spectroscopy measurement

In this section the fit results for the Time-of-Flight (ToF) data analysis at TDC 1 will be discussed. In the data analysis methodology, it is assumed that the peak shape does not change across turns in the analyzer. It is well known that variations in peak shape occur for ions with different charges; therefore, any ion of interest must be analyzed using a peak shape corresponding to the same ion charge.

In the present data analysis it is visible how the peakshape of the ion distribution changes within the same "family" of ions, for example, among isotopes of Cd, as shown in Fig. 5.2. In this figure, it is visible how the peak shape distribution changes among the isotopes of Cd. The red line represents the fit obtained by using a chosen common peak shape for all the peak distributions presented in Fig. 5.2, while the black points correspond to the data acquired for Cd isotopes as singly charged ions.

The red fit curve highlights how the distributions of the black data points deviate from the assumed common peakshape in different ways, indicating that the peak shapes are not identical even within singly charged ions. Furthermore, these differences are evident within a range of a few mass-to-charge units and it is not expected that the potential field in the analyzer has a different influence on ions of similar mass - over - charge ratio. On the other side, as it can be seen for ^{110}Cd and ^{111}Cd, which undergo the same turn number $T = 139$ (where T represents the number of turns the ions make in the analyzer before injection onto the detector), their distributions appear similar.

The resulting differences of the inferred ToF peak widths (FWHM) depending on the number of turns in the MRTOF analyzer for certain masses and on the position of a peak in the Time-of-Flight spectrum is evident already in mass calibrant data. Fig. 5.3 displays the width (FWHM) of different calibrant mass peaks as a function of the turn number in the MRTOF analyzer. As visible in Fig. 5.3 strong fluctuations exist between the peak widths even within groups of calibrant mass lines from the same source. There is no agreement of the FWHM values within experimental uncertainties, instead far larger deviations are found.

The most severe challenge encountered during the analysis of mass spectroscopy data is related to the beam alignment in the analyzer.

In the MRTOF analyzer, alignment refers to ensuring that ion trajectories are well-centered and consistent, enabling accurate and precise mass-to-charge ratio (m/q) measurements. Proper alignment minimizes variations in ion paths, ensuring uniform energy and synchronized timing. This is critical for maintaining sharp mass peaks, as misalignment can lead to broadening and reduced resolution.

Alignment is achieved through careful tuning of the electric fields within the analyzer to create uniform ion reflections and, when the beam exits the analyzer, tuning the TFS reflector voltages to ensure the beam hits the center of the detector. Additionally, systems such as energy bunchers standardize the kinetic energy of ions entering the analyzer, further stabilizing their time-of-flight. Calibration using mass peaks of known isotopes helps monitor and refine alignment, with the Full Width at Half Maximum (FWHM) serving as a diagnostic tool. A low and consistent FWHM across multiple ion reflections indicates good

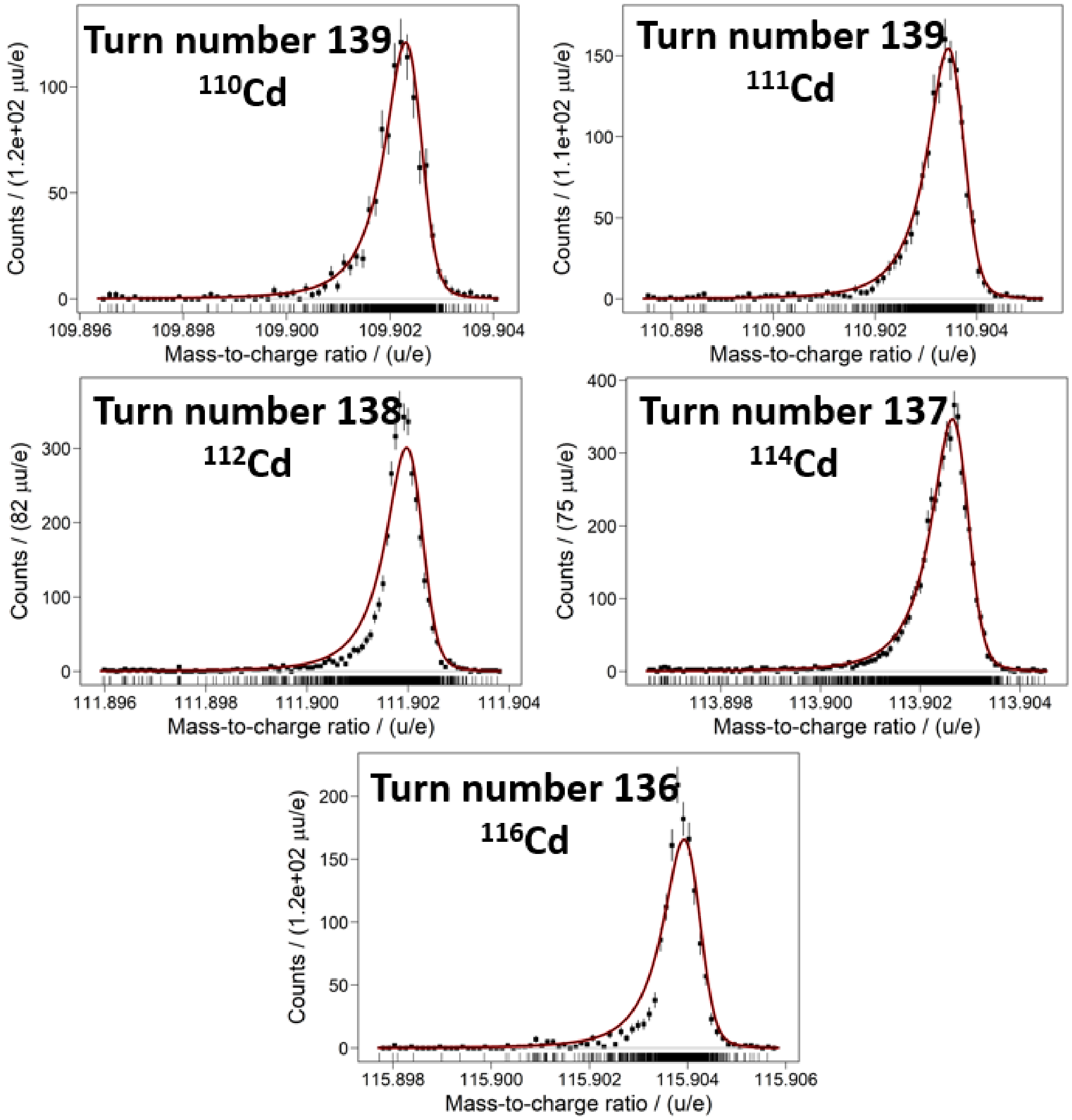

Figure 5.2: Peak shape distribution for Cd isotopes. Black points represent experimental data for Cd isotopes as singly charged ions, while the red curves show the fit obtained using a uniform peak shape across all cases. Deviations between the data and the fit highlight variations in peak shape among isotopes, despite having the same ionic charge. However, ^{110}Cd and ^{111}Cd, both with turn number $T = 139$, exhibit similar distributions.

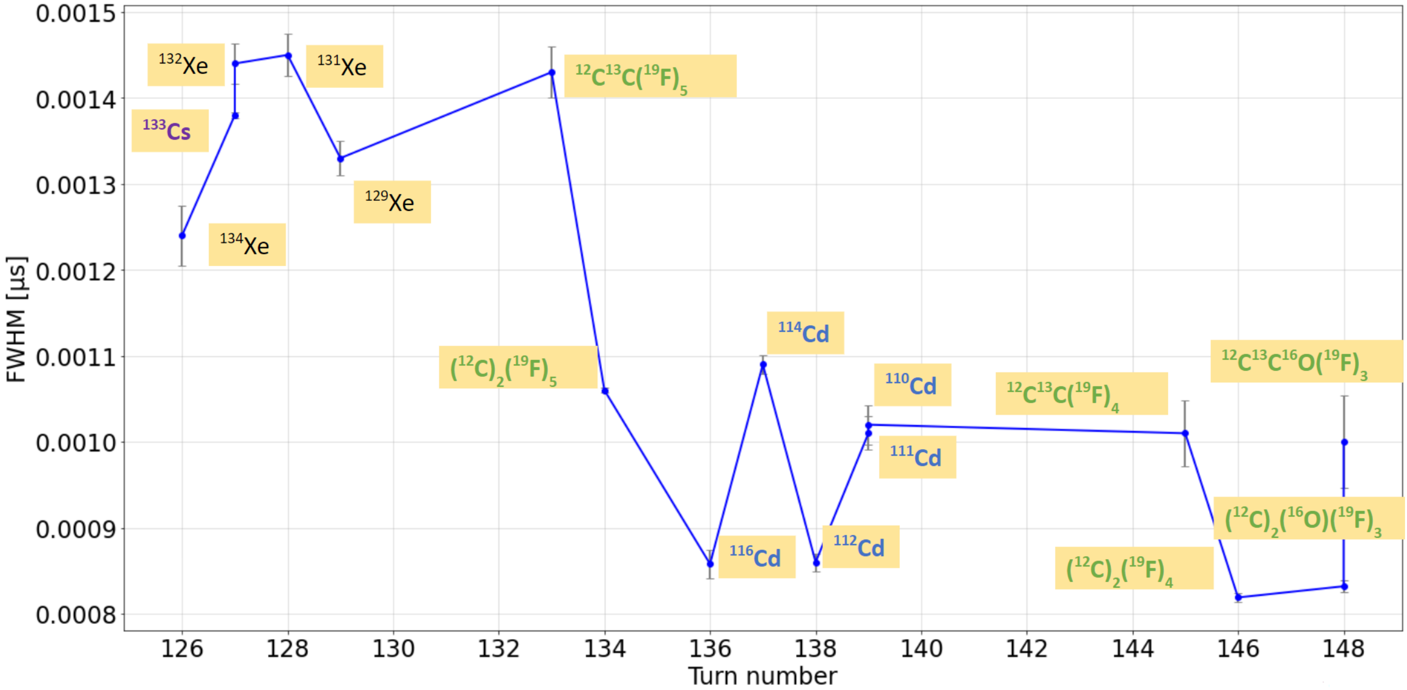

Figure 5.3: FWHM of mass calibrant peaks as a function of the turn number in the MRTOF analyzer. Ions labelled with the same colors belong to the same calibrant source.

alignment, while increasing FWHM suggests cumulative misalignment or inefficiencies in the setup.

In a well-aligned system, the FWHM remains stable even as the number of ion turns increases. This stability is essential for achieving high resolution in mass spectrometry, particularly in MRTOF analyzers, where ions undergo multiple reflections over extended periods. Proper alignment ensures accurate mass measurements and reliable characterization of ion species.

The misalignment found in the mass spectroscopy data proved to be unexpectedly large compared to previous cases, significantly affecting the reachable mass accuracy. Due to the misalignment, an absolute Time-of-Flight (ToF) deviation was observed particularly during ejection through the TFS deflector. The ToF error was also amplified by the high repetition rate used to improve the detection of short-lived nuclei. The unusually high transmission rate caused anomalous variations of the peak shape across turns, a phenomenon never previously observed. [Note after submission: The MRS settings were automatically switched between two configurations, each for such a short time that the electronics inside the MR-TOF never reached a stable state. As a result, the system operated continuously under random/unstable conditions. which resulted in a non-unique and continuously changing peak shape.]

In good alignment condition a couple of calibration points are sufficient, but in this case they are not enough to make an effective error correction. A more detailed calibration across multiple turns could have allowed for better parametrization of the alignment error and enabled the implementation of corrective measures.

The standard data analysis, which assumes uniform peak shape, is therefore ineffective here, resulting in an approximate mass uncertainties of circa 250 keV. While the mass measurements suffice for identification purposes, they do not support detailed nuclear structure analysis (barrier height, curvatures).

Although beam alignment issues limit the precision of mass values, the data confirm the detection of these short-lived species. The 200 Hz repetition rate was instrumental in obtaining sufficient sampling within the brief half-life window.

Furthermore, as demonstrated in [132], it has been proven that mass measurements of short-lived nuclides can be performed at the FRS-IC as indicated by the measurement of ^{215}Po ($t_{1/2} = 1.8$ ms) achieved by isolating the parent and awaiting its decay.

For these reasons we are confident that similar direct mass measurements in the actinide mass region can be achieved in the future.

Future experiments will prioritize a refined beam alignment and a broader set of calibration points provided in a wide mass range from a laser ablation carbon cluster ion (LACCI) source [143]. These improvements will enhance the FRS-IC's ability to measure short-lived isotopes, supporting both identification and, where possible, insights into nuclear structure of heavy and strongly deformed nuclear species at the interface between the region of classical nuclear physics and the upper part of the nuclear chart with the region of superheavy elements.

Chapter 6

Summary and outlook

This thesis explores the properties and formation condition conditions of superdeformed nuclear shapes in the actinide region, with a particular focus on fission isomers and new production and acquisition methodologies. Two exploratory experiments are presented in this work. The first was conducted at the Fragment Separator (FRS) and the FRS Ion Catcher (FRS-IC) at GSI, and at IGISOL at the JYFL Laboratory of the University of Jyväskylä.

The heavy actinides region is particularly compelling for investigating superdeformed states due to the interplay between strong shell effects and deformation-driving forces at low angular momentum.

In the context of experiment S530, it was demonstrated that fragmentation is a suitable method for producing isotopes in the actinide region and that these isotopes can be efficiently selected and delivered to the FRS-IC. Key aspects of the experimental methodology included precise beam alignment, optimization of degrader settings for efficient ion separation and transport, and advanced mass spectroscopy for isotope identification. Furthermore, the installation of a short DC cage into the FRS - Ion Catcher was shown to be instrumental for fast ion extraction from the stopping cell and for the subsequent detection and identification of particularly short-lived isotopes reducing extraction times. The high repetition rate 200 Hz of the MRTOF also played an essential role in ensuring the detection of these short-lived nuclei.

Moreover, the upgraded DC electrode system also boosted the rate capability and thus the beam current acceptance of the stopping cell by at least an order of magnitude; while previously a drop of the extraction efficiency occurred at about 10^4 incoming beam ions per second, after implementation of the short DC cage the efficiency stayed at its maximum until 2×10^5 ions/seconds, only limited by the maximum beam current allowed to enter the experimental area from radioprotection limits.

The experimental setup and data acquisition system enabled fast identification of the delivered isotopes, mass measurements, and Q_α value determination, confirming the reliability of the FRS-IC setup for nuclear structure studies.

This work also introduced the Time-Over-Threshold (ToT) method, applied to the energy signal, which proved effective in distinguishing fission fragment events from alpha decays.

This technique addresses challenges posed by the low cross-section of fission events relative to the competing alpha decay channel and establishes a novel tool for identifying fission isomers.

The second experiment, I290, performed as part of this work, demonstrated that the applied detection techniques allowed for measuring half-lives time for the decay of fission isomers in Am isotopes in good agreement with literature values. This confirms the validity of this alternative methodology for the production and measurement of fission isomers. Future analysis of additional data branches beyond the scope of this thesis and acquired during this collaborative experiment is expected to provide further insights, including information on fission isomers such as their excitation energy in the second potential well E_{II} and the barrier penetration probability.

This thesis establishes a strong foundation for future experimental investigations in the actinides region, emphasizing the importance of using multiple detection methodologies and state-of-the-art instrumentation to advance our understanding of superdeformed nuclear states. In this context, a new experiment is scheduled for June next year, using the fragmentation reaction to produce and implant ^{236}U nuclei.

During the S530 experiment, the combination of significant background suppression challenges, a 500 ns dead time, and the limited number of surviving events prevented a conclusive determination of the half-life of ^{236}U. Current scientific literature presents two conflicting values for this half-life (60 ns and 120 ns), based on previous experiments.

In the upcoming experiment, an improved system will be utilized, featuring a reduced-thickness implanter (0.5 mm or 1 mm) designed to decrease the dead time to 100 ns. This optimization will reduce the energy deposited by implanted ions, minimizing electronic signals that could cause saturation. Additionally, the setup will include two new veto detectors: VETO 1, located upstream, with a 0.5 mm thick plastic scintillator, and VETO 2, located downstream, with a 5 mm thick scintillator. The latter, being thicker than the one used in S530, will enable more effective suppression of background signals originating from the degrader.

literatur

Bibliography

[1] A. Jain, B. Maheshwari, and A. Goel. *Nuclear Isomers - A Primer*. Springer, July 2021. ISBN: 978-3-030-78675-5. DOI: `10.1007/978-3-030-78675-5#toc`.

[2] I. Tanihata, H. Toki, and T. Kajino, eds. *Handbook of Nuclear Physics*. Springer, 2023. ISBN: 978-981-19-6344-5, 978-981-19-6345-2, 978-981-15-8818-1. DOI: `10.1007/978-981-15-8818-1`.

[3] B. Maheshwari P. M. Walker A. K. Jain. "Nuclear Isomers". In: *The European Physics Journal Special Topics, 2024, vol. 233, Issue 5*. Springer, 2024.

[4] E. Rutherford. "The scattering of alpha and beta particles by matter and the structure of the atom". In: *Philosophical Magazine* 21 (1911), pp. 669–688.

[5] F. Soddy. "Intra-atomic Charge". In: *Nature* 92 (1913), pp. 399–400. DOI: `10.1038/092399a0`.

[6] G. Greison. *Sei donne che hanno cambiato il mondo: Le grandi scienziate della fisica del XX secolo*. Bollati Boringhieri Saggi. Bollati Boringhieri, 2017. ISBN: 9788833975597. URL: `https://books.google.de/books?id=QF8yDwAAQBAJ`.

[7] J. Chadwick. "The Existence of a Neutron". In: *Proceedings of the Royal Society of London. Series A, Containing Papers of a Mathematical and Physical Character* 136 (1932), pp. 692–708. DOI: `10.1098/rspa.1932.0112`.

[8] C. F. von Weizsäcker. "Zur Theorie der Kernmassen". In: *Naturwissenschaften* 24 (1936), p. 813. DOI: `10.1007/BF01493837`.

[9] M. G. Mayer. "On Closed Shells in Nuclei. II". In: *Physical Review* 75 (1949), pp. 1969–1970. DOI: `10.1103/PhysRev.75.1969`.

[10] O. Haxel, J. H. D. Jensen, and H. E. Suess. "On the "Magic Numbers" in Nuclear Structure". In: *Physical Review* 75 (1949), pp. 1766–1766. DOI: `10.1103/PhysRev.75.1766`.

[11] A. Bohr and B. R. Mottelson. *Nuclear Structure*. Vol. I. New York: Benjamin, 1969, p. 223.

[12] P. Walker and G. Dracoulis. "Energy traps in atomic nuclei". In: 399.6731 (May 1999), pp. 35–40. DOI: `10.1038/19911`.

[13] A. K. Jain et al. “Atlas of Nuclear Isomers”. In: *Nuclear Data Sheets* 128 (2015), pp. 1–130. ISSN: 0090-3752. DOI: `https://doi.org/10.1016/j.nds.2015.08.001`. URL: `https://www.sciencedirect.com/science/article/pii/S0090375215000344`.

[14] F.G. Kondev et al. “The NUBASE2020 evaluation of nuclear physics properties *”. In: *Chinese Physics C* 45.3 (2021), p. 030001. DOI: `10.1088/1674-1137/abddae`. URL: `https://dx.doi.org/10.1088/1674-1137/abddae`.

[15] I. Tanihata, H. Toki, and T. Kajino, eds. *Handbook of Nuclear Physics*. Springer, 2023. Chap. 12. ISBN: 978-981-19-6344-5, 978-981-19-6345-2, 978-981-15-8818-1. DOI: `10.1007/978-981-15-8818-1`.

[16] R. B. Firestone. “The table of isotopes-8th edition and beyond”. In: *Transactions of the American Nuclear Society* 75 (Dec. 1996). URL: `https://www.osti.gov/biblio/426372`.

[17] F. G. Kondev, G. D. Dracoulis, and T. Kibédi. “Configurations and hindered decays of K isomers in deformed nuclei with A¿100”. In: *Atomic Data and Nuclear Data Tables* 103-104 (2015), pp. 50–105. ISSN: 0092-640X. DOI: `https://doi.org/10.1016/j.adt.2015.01.001`. URL: `https://www.sciencedirect.com/science/article/pii/S0092640X15000029`.

[18] J. Cerny et al. “Confirmed proton radioactivity of 53Com”. In: *Physics Letters B* 33.4 (1970), pp. 284–286. ISSN: 0370-2693. DOI: `https://doi.org/10.1016/0370-2693(70)90270-4`. URL: `https://www.sciencedirect.com/science/article/pii/0370269370902704`.

[19] M. Pfützner et al. “Radioactive decays at limits of nuclear stability”. In: *Rev. Mod. Phys.* 84 (2 2012), pp. 567–619. DOI: `10.1103/RevModPhys.84.567`. URL: `https://link.aps.org/doi/10.1103/RevModPhys.84.567`.

[20] D. Symochko, E. Browne, and J. K. Tuli. “Nuclear Data Sheets for A = 119”. In: *Nuclear Data Sheets* 110 (Nov. 2009), pp. 2945–3105. DOI: `10.1016/j.nds.2009.10.003`.

[21] S. Hofmann et al. “The new isotope ^{270}110 and its decay products ^{266}Hs and ^{262}Sg”. In: *European Physical Journal A* 10.1 (Feb. 2001), pp. 5–10. DOI: `10.1007/s100500170137`.

[22] F. R. Xu et al. “Enhanced Stability of Superheavy Nuclei Due to High-Spin Isomerism”. In: *Physical Review Letters* 92.25 (June 2004). ISSN: 1079-7114. DOI: `10.1103/physrevlett.92.252501`. URL: `http://dx.doi.org/10.1103/PhysRevLett.92.252501`.

[23] J. Kallunkathariyil et al. “Stability of the heaviest elements: K isomer in ^{250}No”. In: *Phys. Rev. C* 101 (1 2020), p. 011301. DOI: `10.1103/PhysRevC.101.011301`. URL: `https://link.aps.org/doi/10.1103/PhysRevC.101.011301`.

[24] P. Walker and Z. Podolyák. *Celebrating a century of nuclear isomers*. Accessed: 2024-10-23. 2019. URL: `https://physicsworld.com/a/celebrating-a-century-of-nuclear-isomers/`.

[25] C. Chiara et al. "Isomer depletion as experimental evidence of nuclear excitation by electron capture". In: *Nature* 554 (2018), pp. 216–218. DOI: `10.1038/nature25483`.

[26] Burke J. T. "One tick closer to a nuclear clock". In: *Nature* 573 (2019), pp. 202–203. DOI: `10.1038/d41586-019-02664-8`.

[27] B. Seiferle et al. "Energy of the ^{229}Th nuclear clock transition". In: *Nature* 573 (2019), pp. 243–246. DOI: `10.1038/s41586-019-1533-4`.

[28] L. von der Wense et al. "A Laser Excitation Scheme for ^{229m}Th". In: *Phys. Rev. Lett.* 119 (13 2017), p. 132503. DOI: `10.1103/PhysRevLett.119.132503`. URL: `https://link.aps.org/doi/10.1103/PhysRevLett.119.132503`.

[29] N. Minkov and A. Pálffy. "Reduced Transition Probabilities for the Gamma Decay of the 7.8 eV Isomer in ^{229}Th". In: *Physical Review Letters* 118 (2017), p. 212501. DOI: `10.1103/PhysRevLett.118.212501`.

[30] J. T. Burke. "One tick closer to a nuclear clock". In: 573.7773 (Sept. 2019), pp. 202–203. DOI: `10.1038/d41586-019-02664-8`.

[31] C. J. Campbell et al. "Single-Ion Nuclear Clock for Metrology at the 19th Decimal Place". In: *Phys. Rev. Lett.* 108 (12 2012), p. 120802. DOI: `10.1103/PhysRevLett.108.120802`. URL: `https://link.aps.org/doi/10.1103/PhysRevLett.108.120802`.

[32] V. V. Flambaum. "Enhanced Effect of Temporal Variation of the Fine Structure Constant and the Strong Interaction in ^{229}Th". In: *Phys. Rev. Lett.* 97 (9 2006), p. 092502. DOI: `10.1103/PhysRevLett.97.092502`. URL: `https://link.aps.org/doi/10.1103/PhysRevLett.97.092502`.

[33] E. Peik et al. "Nuclear clocks for testing fundamental physics". In: *Quantum Science and Technology* 6.3 (2021), p. 034002. DOI: `10.1088/2058-9565/abe9c2`. URL: `https://dx.doi.org/10.1088/2058-9565/abe9c2`.

[34] I. Tanihata, H. Toki, and T. Kajino, eds. *Handbook of Nuclear Physics*. Springer, 2023. Chap. 1. ISBN: 978-981-19-6344-5, 978-981-19-6345-2, 978-981-15-8818-1. DOI: `10.1007/978-981-15-8818-1`.

[35] C. Jesch et al. "The MR-TOF-MS isobar separator for the TITAN facility at TRIUMF". In: *Hyperfine Interactions* (May 2015). DOI: `10.1007/s10751-015-1184-2`.

[36] T. Dickel et al. "Recent upgrades of the multiple-reflection time-of-flight mass spectrometer at TITAN, TRIUMF". In: *Hyperfine Interactions* 240 (June 2019). DOI: `10.1007/s10751-019-1610-y`.

[37] R. Wolf et al. "ISOLTRAP's multi-reflection time-of-flight mass separator/spectrometer". In: *International Journal of Mass Spectrometry* 349 (Sept. 2013), pp. 123–133. DOI: `10.1016/j.ijms.2013.03.020`.

[38] S. Raeder et al. "An ion guide laser ion source for isobar-suppressed rare isotope beams". In: *The Review of scientific instruments* 85 (Mar. 2014), p. 033309. DOI: `10.1063/1.4868496`.

[39] G. Münzenberg et al. "The velocity filter ship, a separator of unslowed heavy ion fusion products". In: *Nucl. Instrum. Meth.* 161 (1979), pp. 65–82. DOI: `10.1016/0029-554X(79)90362-8`.

[40] M. Schädel. "Superheavy element chemistry at GSI - Status and perspectives". In: *The European Physical Journal D* 45 (Oct. 2007), pp. 67–74. DOI: `10.1140/epjd/e2007-00036-6`.

[41] H. Geissel et al. "The GSI projectile fragment separator (FRS): a versatile magnetic system for relativistic heavy ions". In: *Nuclear Instruments and Methods in Physics Research B* 70.1-4 (Aug. 1992), pp. 286–297. DOI: `10.1016/0168-583X(92)95944-M`.

[42] H. Geissel, G. Münzenberg, and K. Riisager. "Secondary exotic nuclear beams". In: *Ann. Rev. Nucl. Part. Sci.* 45 (1995), pp. 163–203. DOI: `10.1146/annurev.ns.45.120195.001115`.

[43] H. Geissel et al. "New results with stored exotic nuclei at relativistic energies". In: *Nucl. Phys. A* 746 (2004). Ed. by G. Savard, C. N. Davids, and C. J. Lister, pp. 150–155. DOI: `10.1016/j.nuclphysa.2004.09.030`.

[44] I. D. Moore et al. "Towards commissioning the new IGISOL-4 facility". In: *Nuclear Instruments and Methods in Physics Research Section B: Beam Interactions with Materials and Atoms* 317 (2013). XVIth International Conference on ElectroMagnetic Isotope Separators and Techniques Related to their Applications, December 2–7, 2012 at Matsue, Japan, pp. 208–213. ISSN: 0168-583X. DOI: `https://doi.org/10.1016/j.nimb.2013.06.036`. URL: `https://www.sciencedirect.com/science/article/pii/S0168583X13007143`.

[45] I. Moore et al. "Development of a laser ion source at IGISOL". In: *Journal of Physics G: Nuclear and Particle Physics* 31 (Sept. 2005), S1499. DOI: `10.1088/0954-3899/31/10/020`.

[46] P. Van Duppen et al. "A laser ion source for on-line mass separation". In: *Hyperfine Interactions* 74 (Jan. 1992), pp. 193–204. DOI: `10.1007/BF02398629`.

[47] "UNILAC: A linear accelerator for atomic ions of any mass". In: (Dec. 1966).

[48] K. Blasche and B. Franczak. "The heavy ion synchrotron SIS". In: *In Proc. EPAC* (1992), p. 9.

[49] W. R. Plaß et al. “The FRS Ion Catcher – A facility for high-precision experiments with stopped projectile and fission fragments”. In: *Nuclear Instruments and Methods in Physics Research Section B: Beam Interactions with Materials and Atoms* 317 (2013). XVIth International Conference on ElectroMagnetic Isotope Separators and Techniques Related to their Applications, December 2–7, 2012 at Matsue, Japan, pp. 457–462. ISSN: 0168-583X. DOI: `https://doi.org/10.1016/j.nimb.2013.07.063`. URL: `https://www.sciencedirect.com/science/article/pii/S0168583X13008823`.

[50] W. R. Plaß et al. “The science case of the FRS Ion Catcher for FAIR Phase-0”. In: *Hyperfine Interact.* 240.1 (2019), p. 111. DOI: `10.1007/s10751-019-1597-4`.

[51] *Website Title*. 2024. URL: `https://www.gsi.de/en/researchaccelerators/fair`.

[52] T. Dickel et al. “Mean range bunching of exotic nuclei produced by in-flight fragmentation and fission — Stopped-beam experiments with increased efficiency”. In: *Nucl. Instrum. Meth. B* 541 (2023), pp. 275–278. DOI: `10.1016/j.nimb.2023.05.018`. arXiv: `2306.09350 [physics.ins-det]`.

[53] B. Voss et al. “The scintillation-detector equipment of the GSI projectile—fragment separator”. In: *Nuclear instruments & methods in physics research / A* 364.1 (1995), pp. 150 –158. ISSN: 0168-9002. DOI: `10.1016/0168-9002(95)00294-4`. URL: `https://repository.gsi.de/record/51632`.

[54] R. Janik et al. “Time Projection Chambers with C-pads for heavy ion tracking”. In: *Nuclear Instruments Methods in Physics Research Section A-accelerators Spectrometers Detectors and Associated Equipment - NUCL INSTRUM METH PHYS RES A* 640 (June 2011), pp. 54–57. DOI: `10.1016/j.nima.2011.02.052`.

[55] M. Pfützner et al. “Energy deposition by relativistic heavy ions in thin argon absorbers”. In: *Nuclear Instruments and Methods in Physics Research Section B: Beam Interactions with Materials and Atoms* 86.3 (1994), pp. 213–218. ISSN: 0168-583X. DOI: `https://doi.org/10.1016/0168-583X(94)95280-9`. URL: `https://www.sciencedirect.com/science/article/pii/0168583X94952809`.

[56] A. Stolz et al. “A detector system for the identification of relativistic heavy ions at high rates”. In: *GSI scientific report 1998* (1999).

[57] R. Julin and P. Dendooven. “The JYFL Accelerator Laboratory in Jyväskylä”. In: *Nuclear Physics News* 10 (Jan. 2000), pp. 4–10. DOI: `10.1080/10506890009411534`.

[58] Carroll J. Carpenter M. et al. Chiara C. “Isomer depletion as experimental evidence of nuclear excitation by electron capture.” In: *Nature* 554 (218), 216–218. URL: `https://doi.org/10.1038/nature25483`.

[59] Yuanbin Wu, Christoph H. Keitel, and Adriana Pálffy. “^{93m}Mo Isomer Depletion via Beam-Based Nuclear Excitation by Electron Capture”. In: *Phys. Rev. Lett.* 122 (21 2019), p. 212501. DOI: `10.1103/PhysRevLett.122.212501`. URL: `https://link.aps.org/doi/10.1103/PhysRevLett.122.212501`.

[60] J. Rzadkiewicz et al. “Beam-based scenario for ^{242m}Am isomer depletion via nuclear excitation by electron capture”. In: *Phys. Rev. C* 99 (4 2019), p. 044309. DOI: `10.1103/PhysRevC.99.044309`. URL: `https://link.aps.org/doi/10.1103/PhysRevC.99.044309`.

[61] S. M. Polikanov et al. “Spontaneous fission with anomalously short period”. In: *Zh. Eksp. Teor. Fiz.* 42 (1962), p. 1016.

[62] S. Bjørnholm and J. E. Lynn. “The double-humped fission barrier”. In: *Rev. Mod. Phys.* 52 (4 1980), pp. 725–931. DOI: `10.1103/RevModPhys.52.725`. URL: `https://link.aps.org/doi/10.1103/RevModPhys.52.725`.

[63] A. Fubini et al. “Short-Range Intermediate Structure Observed in the ^{237}Np Neutron Subthreshold Fission Cross Section”. In: *Phys. Rev. Lett.* 20 (24 1968), pp. 1373–1375. DOI: `10.1103/PhysRevLett.20.1373`. URL: `https://link.aps.org/doi/10.1103/PhysRevLett.20.1373`.

[64] V. M. Strutinsky. “Shell effects in nuclear masses and deformation energies”. In: *Nuclear Physics A* 95.2 (1967), pp. 420–442. ISSN: 0375-9474. DOI: `https://doi.org/10.1016/0375-9474(67)90510-6`. URL: `https://www.sciencedirect.com/science/article/pii/0375947467905106`.

[65] G. N. Flerov and V. A. Druin. “Radioactive Properties of Nuclei of Heaviest Elements (Review); Radioaktive svoistvayader naibolee tyazhelykh elementov”. In: (Jan. 1966). URL: `https://www.osti.gov/biblio/4553683`.

[66] K. S. Krane and D. Halliday. *Introductory nuclear physics*. New York: Wiley, 1987. ISBN: 978-0-471-80553-3.

[67] D. L. Hill and J. A. Wheeler. “Nuclear Constitution and the Interpretation of Fission Phenomena”. In: *Phys. Rev.* 89 (5 1953), pp. 1102–1145. DOI: `10.1103/PhysRev.89.1102`. URL: `https://link.aps.org/doi/10.1103/PhysRev.89.1102`.

[68] *Physics and Chemistry of Fission - 1965 (Salzburg, 22-26 March 1965)*. Proceedings Series. Vienna: INTERNATIONAL ATOMIC ENERGY AGENCY, 1965. ISBN: 92-0-030665-9. URL: `https://www.iaea.org/publications/2050/physics-and-chemistry-of-fission-1965-salzburg-22-26-march-1965`.

[69] B. D. Wilkins, E. P. Steinberg, and R. R. Chasman. “Scission-point model of nuclear fission based on deformed-shell effects”. In: *Phys. Rev. C* 14 (5 1976), pp. 1832–1863. DOI: `10.1103/PhysRevC.14.1832`. URL: `https://link.aps.org/doi/10.1103/PhysRevC.14.1832`.

[70] E. Migneco and J. P. Theobald. “Resonance grouping structure in neutron induced subthreshold fission of 240Pu”. In: *Nuclear Physics A* 112.3 (1968), pp. 603–608. ISSN: 0375-9474. DOI: `https://doi.org/10.1016/0375-9474(68)90081-X`. URL: `https://www.sciencedirect.com/science/article/pii/037594746890081X`.

[71] S. Plattard, J. Blons, and D. Paya. "Fission Cross Section of Neptunium-237 from 3 eV to 2 MeV". In: *Nuclear Science and Engineering* 61.4 (1976), pp. 477–495. DOI: `10.13182/NSE76-A14485`.

[72] G. F. Auchampaugh et al. "Nature of the coupling in subthreshold fission of ^{238}Np". In: *Phys. Rev. C* 29 (1 1984), pp. 174–181. DOI: `10.1103/PhysRevC.29.174`. URL: `https://link.aps.org/doi/10.1103/PhysRevC.29.174`.

[73] G. F. Auchampaugh and C. D. Bowman. "Parameters of the Subthreshold Fission Structure in ^{242}Pu". In: *Phys. Rev. C* 7 (5 1973), pp. 2085–2091. DOI: `10.1103/PhysRevC.7.2085`. URL: `https://link.aps.org/doi/10.1103/PhysRevC.7.2085`.

[74] H. Weigmann, J. A. Wartena, and C. Bürkholz. "Neutron-induced fission cross section of 242 Pu". In: *Nucl. Phys. A* 438 (1985), pp. 333–353. DOI: `10.1016/0375-9474(85)90379-3`.

[75] F. C. Di filippo et al. "Measurement of the /sup 238/U subthreshold fission cross section for incident neutron energies between 0. 6 and 100 keV". In: *Nucl. Sci. Eng.; (United States)* 63 (June 1977). URL: `https://www.osti.gov/biblio/7097173`.

[76] S. G. Nilsson. "Binding states of individual nucleons in strongly deformed nuclei". In: *Kong. Dan. Vid. Sel. Mat. Fys. Med.* 29N16 (1955), pp. 1–69.

[77] H. Weigmann. "The Nuclear Fission Process". In: *The Nuclear Fission Process*. Ed. by C. Wagemans. Boca Raton/Ann Arbor/Boston/London: CRC Press, 1991, pp. 7–33.

[78] C. Gustafson et al. "Nuclear deformabilities in the rare-earth and actinide regions with excursions off the stability line and into the super-heavy region." In: *Ark. Fys., 36: 613-27(1967).* (Jan. 1967). URL: `https://www.osti.gov/biblio/4523550`.

[79] P. G. Thirolf and D. Habs. "Spectroscopy in the second and third minimum of actinide nuclei". In: *Progress in Particle and Nuclear Physics* 49.2 (2002), pp. 325–402. ISSN: 0146-6410. DOI: `https://doi.org/10.1016/S0146-6410(02)00158-8`. URL: `https://www.sciencedirect.com/science/article/pii/S0146641002001588`.

[80] H. Weigmann. "The Nuclear Fission Process". In: *The Nuclear Fission Process*. Ed. by C. Wagemans. Boca Raton/Ann Arbor/Boston/London: CRC Press, 1991, pp. 63–102.

[81] P. Möller and J. R. Nix. "Calculation of Fission Barriers". In: *Physics and Chemistry of Fission 1973, vol. 1.* Vienna: IAEA, 1974, p. 103.

[82] I. Tanihata, H. Toki, and T. Kajino, eds. *Handbook of Nuclear Physics*. Springer, 2023. Chap. 20. ISBN: 978-981-19-6344-5, 978-981-19-6345-2, 978-981-15-8818-1. DOI: `10.1007/978-981-15-8818-1`.

[83] A. K. Jain et al. "Atlas of nuclear isomers". In: *Nucl. Data Sheets* 128 (2015), p. 1.

[84] S. Oberstedt et al. "Limits on the half life of the shape isomer in ^{239}U". In: *Nucl. Phys. A* 573 (1994a), p. 467.

[85] S. Oberstedt et al. “Intermediate structure and the shape isomer in ^{233}Th”. In: *Nucl. Phys. A* 578 (1994b), p. 31.

[86] A. Oberstedt and S. Oberstedt. “Exploring the fission barrier of ^{235}U”. In: *Phys. Rev. C* 104 (2021), p. 024611.

[87] J. Blons, C. Mazur, and D. Paya. “Evidence for rotational bands near the $^{232}\mathrm{Th}(n, f)$ fission threshold”. In: *Phys. Rev. Lett.* 35 (1975), p. 1750.

[88] J. Blons et al. “Rotational bands in asymmetrically deformed ^{231}Th”. In: *Phys. Rev. Lett.* 41 (1978), p. 1282.

[89] J. Blons et al. “High resolution fission probabilities for $^{229,230,232}\mathrm{Th}(d, pf)$ and $^{233,236}\mathrm{U}(d, pf)$ reactions”. In: *Nucl. Phys. A* 477 (1988), p. 231.

[90] R. Bengtsson et al. “Properties of nuclei at the third-minimum deformation”. In: *Nucl. Phys. A* 473 (1987), p. 77.

[91] S. Cwiok et al. “Hyperdeformations and clustering in the actinide nuclei”. In: *Phys. Lett. B* 322 (1994), p. 304.

[92] P. G. Thirolf. “Spectroscopy in the Second and Third Minimum of Actinide Nuclei”. Habilitationsschrift. PhD thesis. Munich: Ludwig-Maximilians-Universität München, 2003.

[93] P. G. Reinhard. In: *Z. Phys. A* 329 (1988), p. 257.

[94] P. G. Reinhard et al. In: *Z. Phys. A* 323 (1986), p. 13.

[95] M. M. Sharma, M. A. Nagarajan, and P. Ring. In: *Phys. Lett. B* 312 (1993), p. 377.

[96] J. F. Berger, M. Girod, and D. Gogny. In: *N. Phys. A* 502 (1989), p. 85c.

[97] H. X. Zhang, T. R. Yeh, and H. Lancman. In: *Phys. Lett. C* 34 (1986), p. 1397.

[98] K. Rutz et al. In: *N. Phys. A* 590 (1995), p. 680.

[99] U. Brosa et al. “Nuclear scission”. In: *Nucl. Phys. A* 502 (1989), p. 423.

[100] U. Brosa, S. Grossmann, and A. Müller. “Nuclear scission”. In: *Physics Reports* 197.4 (1990), pp. 167–262. ISSN: 0370-1573. DOI: `https://doi.org/10.1016/0370-1573(90)90114-H`. URL: `https://www.sciencedirect.com/science/article/pii/037015739090114H`.

[101] A. Turkevich and J. B. Niday. “Radiochemical Studies on the Fission of Th^{232} with Pile Neutrons”. In: *Phys. Rev.* 84 (1 1951), pp. 52–60. DOI: `10.1103/PhysRev.84.52`. URL: `https://link.aps.org/doi/10.1103/PhysRev.84.52`.

[102] A. Karpov, A. Kelić-Heil, and K. H. Schmidt. “On the topographical properties of fission barriers”. In: *Journal of Physics G Nuclear Physics* 35 (Mar. 2008), p. 035104. DOI: `10.1088/0954-3899/35/3/035104`.

[103] T. Ichikawa et al. “Contrasting fission potential energy structure of actinides and mercury isotopes”. In: *Phys. Rev. C* 86 (2012), p. 024610.

[104] T. Dickel et al. "A high-performance multiple-reflection time-of-flight mass spectrometer and isobar separator for the research with exotic nuclei". In: *Nuclear Instruments and Methods in Physics Research Section A: Accelerators, Spectrometers, Detectors and Associated Equipment* 777 (2015), pp. 172–188. ISSN: 0168-9002. DOI: `https://doi.org/10.1016/j.nima.2014.12.094`. URL: `https://www.sciencedirect.com/science/article/pii/S0168900214015629`.

[105] M. Ranjan et al. "Europhys. Lett." In: *Europhys. Lett.* 96 (2011), p. 52001.

[106] S. Purushothaman et al. "EPL". In: *EPL* 104 (2013), p. 42001.

[107] M. P. Reiter et al. "Rate capability of a cryogenic stopping cell for uranium projectile fragments produced at 1000MeV/u". In: *Nuclear Instruments and Methods in Physics Research Section B: Beam Interactions with Materials and Atoms* 376 (2016). Proceedings of the XVIIth International Conference on Electromagnetic Isotope Separators and Related Topics (EMIS2015), Grand Rapids, MI, U.S.A., 11-15 May 2015, pp. 240–245. ISSN: 0168-583X. DOI: `https://doi.org/10.1016/j.nimb.2015.12.016`. URL: `https://www.sciencedirect.com/science/article/pii/S0168583X15012604`.

[108] A. Rotaru et al. "INCREASE: An in-cell reaction system for multi-nucleon transfer and spontaneous fission at the FRS ion catcher". In: *Nuclear Instruments and Methods in Physics Research Section B: Beam Interactions with Materials and Atoms* 512 (2022), pp. 83–90. ISSN: 0168-583X. DOI: `https://doi.org/10.1016/j.nimb.2021.11.018`. URL: `https://www.sciencedirect.com/science/article/pii/S0168583X21003943`.

[109] I. Miskun. "A Novel Method for the Measurement of Half-Lives and Decay Branching Ratios of Exotic Nuclei with the FRS Ion Catcher". PhD thesis. Justus-Liebig-Universität Gießen, 2019.

[110] F. Greiner. "Construction and Commissioning of an RF Quadrupole Switchyard (in German)". Bachelor thesis. Justus Liebig University Gießen, 2013.

[111] E. Haettner et al. "A versatile triple radiofrequency quadrupole system for cooling, mass separation and bunching of exotic nuclei". In: *Nucl. Instrum. Methods A* 880 (2018), pp. 138–151.

[112] W. R. Plaß et al. "An RF quadrupole-time-of-flight system for isobar-separation and multiplexed low energy rare-isotope beam experiments". In: *Eur. Phys. J. Special Topics* 150 (2007), pp. 367–368.

[113] F. Greiner et al. "Removal of molecular contamination in low-energy RIBs by the isolation-dissociation-isolation method". In: *Nuclear instruments & methods in physics research / B* 463 (2020), pp. 324 –326. ISSN: 0168-583X. DOI: `10.1016/j.nimb.2019.04.072`. URL: `https://repository.gsi.de/record/236643`.

[114] Exosens. *Magnum^{TM} Electron Multiplier*. `https://www.exosens.com/products/magnumtm-electron-multiplier`.

[115] ORTEC. *Ultra Silicon Charged Particle Radiation Detectors for Alpha Spectroscopy.* `https://www.ortec-online.com/products/radiation-detectors/silicon-charged-particle-radiation-detectors/si-charged-particle-radiation-detectors-for-alpha-spectroscopy/ultra`.

[116] I. Mardor et al. "Mass measurements of As, Se, and Br nuclei, and their implication on the proton-neutron interaction strength toward the $N = Z$ line". In: *Phys. Rev. C* 103.3 (2021), p. 034319. DOI: `10.1103/PhysRevC.103.034319`. arXiv: `2011.13288 [nucl-ex]`.

[117] *MagneTOF: A New Class of Robust Sub-nanosecond TOF Detectors with Exceptional Dynamic Range.* Product data sheet. ETP Electron Multipliers. 2023. URL: `https://www.etp-ms.com`.

[118] T. Niwase et al. "Development of an "-TOF" detector for correlated measurement of atomic masses and decay properties". In: *Nuclear Instruments and Methods in Physics Research Section A: Accelerators, Spectrometers, Detectors and Associated Equipment* 953 (2020), p. 163198. ISSN: 0168-9002. DOI: `https://doi.org/10.1016/j.nima.2019.163198`. URL: `https://www.sciencedirect.com/science/article/pii/S0168900219314901`.

[119] W. Plaß, T. Dickel, and C. Scheidenberger. "Multiple-reflection time-of-flight mass spectrometry". In: *International journal of mass spectrometry* 349-350 (2013), pp. 134–144. ISSN: 1387-3806. DOI: `10.1016/j.ijms.2013.06.005`. URL: `https://repository.gsi.de/record/65705`.

[120] C. Will. "Achieving One Million Mass Resolving Power with a Multiple-Reflection Time-of-Flight Mass Spectrometer". Master thesis. Justus Liebig University Gießen, 2019.

[121] ETP Ion Detection. *Ion Detection for Time-of-Flight Mass Spectrometry.* Accessed: 2023-11-06. 2023. URL: `https://www.etp-ms.com/technology/the-etp-difference/ion-detection/TOFMS`.

[122] *Evaluated Nuclear Structure Data File.* URL: `https://www.nndc.bnl.gov/ensdf/`.

[123] J. Bergmann. "High-resolution tandem mass spectrometry of complex mixtures with a multiple-reflection time-of-flight mass spectrometer". PhD thesis. Justus-Liebig-Universität Gießen, 2023.

[124] CAEN S.p.A. *DT5780 - Dual Digital Multi-Channel Analyzer Desktop Module.* 2024. URL: `https://www.caen.it/products/dt5780/`.

[125] R. Haas et al. "Development and characterization of a Drop-on-Demand inkjet printing system for nuclear target fabrication". In: *Nuclear Instruments and Methods in Physics Research Section A: Accelerators, Spectrometers, Detectors and Associated Equipment* 874 (2017), pp. 43–49. ISSN: 0168-9002. DOI: `https://doi.org/10.1016/j.nima.2017.08.027`. URL: `https://www.sciencedirect.com/science/article/pii/S0168900217308987`.

[126] J. Ärje et al. "Submillisecond On-Line Mass Separation of Nonvolatile Radioactive Elements: An Application of Charge Exchange and Thermalization Processes of Primary Recoil Ions in Helium". In: *Phys. Rev. Lett.* 54 (2 1985), pp. 99–101. DOI: `10.1103/PhysRevLett.54.99`. URL: `https://link.aps.org/doi/10.1103/PhysRevLett.54.99`.

[127] M. Wang et al. "The AME 2020 atomic mass evaluation (II). Tables, graphs and references*". In: *Chinese Physics C* 45.3 (2021), p. 030003. DOI: `10.1088/1674-1137/abddaf`. URL: `https://dx.doi.org/10.1088/1674-1137/abddaf`.

[128] C. J. Chiara et al. "Reply to: Possible overestimation of isomer depletion due to contamination". In: *Nature (London)* 594.7861 (June 2021). DOI: `10.1038/s41586-021-03334-4`.

[129] ORTEC. *B-Series Silicon Charged Particle Radiation Detectors for Research Applications.* Accessed: 2024-11-11. 2024. URL: `https://www.ortec-online.com/products/radiation-detectors/silicon-charged-particle-radiation-detectors/si-charged-particle-radiation-detectors-for-research-applications/b-series`.

[130] S. Purushothaman et al. "Hyper-EMG: A new probability distribution function composed of Exponentially Modified Gaussian distributions to analyze asymmetric peak shapes in high-resolution time-of-flight mass spectrometry". In: *International Journal of Mass Spectrometry* 421 (2017), pp. 245–254. ISSN: 1387-3806. DOI: `https://doi.org/10.1016/j.ijms.2017.07.014`. URL: `https://www.sciencedirect.com/science/article/pii/S1387380616302913`.

[131] E. Rey-Herme et al. "Level structure of ^{221}Ac and ^{217}Fr from decay spectroscopy, and reflection asymmetry in ^{221}Ac". In: *Phys. Rev. C* 108 (1 2023), p. 014304. DOI: `10.1103/PhysRevC.108.014304`. URL: `https://link.aps.org/doi/10.1103/PhysRevC.108.014304`.

[132] N. Tortorelli et al. "Alpha spectroscopy of purified beams of exotic nuclei at the FRS Ion Catcher". In: *Nuclear Physics A* 1053 (2025), p. 122967. ISSN: 0375-9474. DOI: `https://doi.org/10.1016/j.nuclphysa.2024.122967`. URL: `https://www.sciencedirect.com/science/article/pii/S0375947424001490`.

[133] S. Ayet San Andrés et al. "High-resolution, accurate multiple-reflection time-of-flight mass spectrometry for short-lived, exotic nuclei of a few events in their ground and low-lying isomeric states". In: *Phys. Rev. C* 99 (2019), p. 064313.

[134] J. Ebert. "Mass Measurements of 238U-Projectile Fragments for the First Time with a Multiple-Reflection Time-Of-Flight Mass Spectrometer". PhD thesis. Justus Liebig University Gießen, 2016.

[135] S. Ayet San Andrés. "Developments for Multiple-Reflection Time-of-Flight Mass Spectrometers and Their Application to High-Resolution Accurate Mass Measurements of Short-Lived Exotic Nuclei". PhD thesis. Justus Liebig University Gießen, 2018.

[136] D. Amanbayev. “Mass measurements at the N=Z and N=126 limits at the FRS Ion Catcher and development of the Cryogenic Stopping Cell for the Super-FRS”. NOCHKG 29.05.2024 DNB Nachweis noch offen; Dissertation, Justus-Liebig-Universität Gießen, 2023. PhD thesis. Justus-Liebig-Universität Gießen, 2023. DOI: `10.22029/JLUPUB-18567`. URL: `https://repository.gsi.de/record/347775`.

[137] S. Purushothaman et al. “Hyper-EMG: A new probability distribution function composed of Exponentially Modified Gaussian distributions to analyze asymmetric peak shapes in high-resolution time-of-flight mass spectrometry”. In: *International Journal of Mass Spectrometry* 421 (2017), pp. 245–254. ISSN: 1387-3806. DOI: `https://doi.org/10.1016/j.ijms.2017.07.014`. URL: `https://www.sciencedirect.com/science/article/pii/S1387380616302913`.

[138] D. Freedman and P. Diaconis. “On the histogram as a density estimator: L^2 theory”. In: *Zeitschrift für Wahrscheinlichkeitstheorie und Verwandte Gebiete* 57.4 (1981), pp. 453–476.

[139] F. J. Massey Jr. “The Kolmogorov-Smirnov test for goodness of fit”. In: *Journal of the American Statistical Association* 46.253 (1951), pp. 68–78.

[140] F. Hu and J. V. Zidek. “The Weighted Likelihood”. In: *Canadian Journal of Statistics* 30.3 (2002), pp. 347–371.

[141] Swati Garg et al. “Atlas of nuclear isomers—Second edition”. In: *Atomic Data and Nuclear Data Tables* 150 (Jan. 2023), p. 101546. ISSN: 0092-640X. DOI: `10.1016/j.adt.2022.101546`. URL: `http://dx.doi.org/10.1016/j.adt.2022.101546`.

[142] J. W. Zhao et al. “Increasing the rate capability for the cryogenic stopping cell of the FRS Ion Catcher”. In: *Nuclear Instruments and Methods in Physics Research Section B: Beam Interactions with Materials and Atoms* 547 (2024), p. 165175. ISSN: 0168-583X. DOI: `https://doi.org/10.1016/j.nimb.2023.165175`. URL: `https://www.sciencedirect.com/science/article/pii/S0168583X23004160`.

[143] J. Yu et al. “A laser ablation carbon cluster ion source for the FRS Ion Catcher”. In: *Nuclear instruments & methods in physics research / Section A* 1064 (2024). German Federal Ministry for Education and Research (BMBF) under contract no. 05P16RGFN1, 05P19RGFN1, and 05P21RGFN1. Helmholtz Association. Office of China Postdoc Council (OCPC).TThis is an open access article under the CC BY license (http://creativecommons.org/licenses/by/4.0/)., p. 169371. ISSN: 0167-5087. DOI: `10.1016/j.nima.2024.169371`. URL: `https://repository.gsi.de/record/350490`.

Acknowledgment

I would like to express my deepest gratitude to my supervisor, Prof. Peter Thirolf, for his invaluable guidance, encouragement, and support throughout my PhD journey. His thought-provoking ”simple” questions opened up a world of possibilities and new ideas, while his kindness and captivating stories made this experience enriching both academically and personally.

My heartfelt thanks extend to Dr. Timo Dickel, for his unwavering confidence in my work, his encouragement to pursue my ideas in the lab, and his remarkable ability to recognize the value in everyone as a resource for the group and the wider scientific community. His dedication to teamwork has been a constant source of inspiration, demonstrating how collaboration drives impactful results.

I am also deeply grateful to Prof. Andreas Oberstaedt for kindly agreeing to serve as the second referee for this thesis. I greatly appreciated the stimulating discussions and shared moments during beam times, which have been both insightful and memorable.

I sincerely thank the members of my research group, particularly Daler, Gabi, Jianwei, and all my colleagues at the FRS-IC, for their collaboration, guidance, and continuous support during challenging moments. Your insights and encouragement have been invaluable.

A special acknowledgment goes to my colleagues and friends at the Medical Physics Chair of LMU. Beyond introducing me to the fascinating applications of nuclear physics, they demonstrated how to build a community founded on sharing resources and knowledge. In particular, I am deeply thankful to Beatrice, for being a dear and honest friend, a “grandma” who nourished me with exceptional food, and a sister with whom I could engage in daily arguments over silly matters, which somehow always brightened my days.

Special appreciation goes to the GSI Helmholtz Centre and LMU Munich, including the technical and administrative staff, for providing the experimental facilities and resources that made this research possible, and for helping to navigate the challenges of bureaucracy.

To Salvatore Esposito, thank you for reminding me of my capabilities and encouraging me to pursue my scientific and personal ambitions.

I am also profoundly grateful to the wonderful friends I made during this journey. A heartfelt thanks to Angelo and Giordano for being my family during the difficult COVID times.

I cannot forget my lifelong friends, who have always been by my side and, with humor and patience, periodically asked, ”Have you finished your thesis yet? We need to be ready for the party!”

To Stefano, thank you for supporting me on my path to happiness and showing me the beauty of thunderstorms.

To my sister, for taking care of the people I love most (including herself), and to my parents, who gifted me the freedom to follow my dreams and taught me the importance of staying true to myself.

To my grandparents, by blood and by choice, whether present on Earth or in Heaven, thank you for making me feel deeply loved and special.

Lastly, I extend my gratitude to my large family for their unconditional love and encouragement. Your unwavering belief in my abilities has been a constant source of motivation.

To all those whose names may not appear here but who have played a part in this journey, your support and kindness have not gone unnoticed. Thank you for everything.

Dedica

Questa tesi la dedico ai miei genitori che mi hanno sempre detto che la cosa più importante nella vita è lo studio. In esso c'è la chiave della libertà. Papà:"se studi sei libera di trovare il lavoro che ti piace ed alle tue condizioni". Mamma:" solo lo studio ti permetterà di essere una donna indipendente economicamente e da ogni restrizione che la società vorrà importi". Grazie, se sono arrivata al massimo grado di istruzione oggi possibile lo devo a voi. Non so ancora qual è il lavoro dei miei sogni né tantomeno quali sono le condizioni sotto le quali vorrei lavorare. E non so nemmeno che donna voglio essere. Ma lungo tutto questo tragitto in cui lo studio si è intrecciato con i primi 32 anni della mia vita, ho visto così tante strade, ho avuto l'opportunità di scegliere quale intraprendere e quale no. Ho conosciuto così tante donne e molte mi hanno inspirata ad essere come sono oggi. Probabilmente non saprò mai qual è la mia strada e/o chi voglio essere ma ad oggi rifarei ogni passo che ho fatto per arrivare fin qui. Io non inseguo un'idea di chi o come vorrò essere, la mia ambizione risiede semplicemente nel cercare di migliorarmi nel tempo. E questa libertà, di poter cambiare chi essere, cosa fare e le persone di cui circondarmi, e la leggerezza, di tuffarmi in ogni idea e persona che incontro esiste in me perchè sono incosciente. E la mia incoscienza prende il sopravvento perchè il mio cuore sa che posso volare leggera perchè, per qualunque cosa mi capiti nella vita, io ho un paracadute. Il mio paracadute siete voi.